FILE COPY

AFOSR-TR- 89-1247

(2)

AD-A212 925

R89-957464-F

Investigation of Fuel Additive Effects on Sooting Flames

by

P. A. Bonczyk
United Technologies Research Center
East Hartford, Connecticut 06108

July 28, 1989

Final Technical Report
under
Contract F49620-86-C-0054

DTIC
ELECTE
SEP 27 1989
S B D

Prepared for
Air Force Office of Scientific Research
Bolling Air Force Base, DC 20332

DISTRIBUTION STATEMENT A
Approved for public release
Distribution Unlimited

"Original contains color plates: All DTIC reproductions will be in black and white"

Unclassified
SECURITY CLASSIFICATION OF THIS PAGE

REPORT DOCUMENTATION PAGE

Form Approved OMB No. 0704-0188

1a. REPORT SECURITY CLASSIFICATION Unclassified

1b. RESTRICTIVE MARKINGS

2a. SECURITY CLASSIFICATION AUTHORITY

2b. DECLASSIFICATION/DOWNGRADING SCHEDULE

3. DISTRIBUTION/AVAILABILITY OF REPORT Approved for public release; distribution is unlimited.

4. PERFORMING ORGANIZATION REPORT NUMBER(S)

5. MONITORING ORGANIZATION REPORT NUMBER(S) AFOSR-TR- 89-1247

6a. NAME OF PERFORMING ORGANIZATION United Technologies Research Center

6b. OFFICE SYMBOL *(If applicable)*

7a. NAME OF MONITORING ORGANIZATION AFOSR/NA

6c. ADDRESS *(City, State, and ZIP Code)*
East Hartford, CT 06108

7b. ADDRESS *(City, State, and ZIP Code)*
Building 410, Bolling AFB DC
20332-6448

8a. NAME OF FUNDING/SPONSORING ORGANIZATION AFOSR/NA

8b. OFFICE SYMBOL *(If applicable)* NA

9. PROCUREMENT INSTRUMENT IDENTIFICATION NUMBER F49620-86-C-0054

8c. ADDRESS *(City, State, and ZIP Code)*
Building 410, Bolling AFB DC
20332-6448

10. SOURCE OF FUNDING NUMBERS

PROGRAM ELEMENT NO.	PROJECT NO.	TASK NO.	WORK UNIT ACCESSION NO.
61102F	2308	A2	

11. TITLE *(Include Security Classification)*
(U) Investigation of Fuel Additive Effects on Sooting Flames

12. PERSONAL AUTHOR(S) Bonczyk, Paul A.

13a. TYPE OF REPORT Final

13b. TIME COVERED FROM 86/6/1 TO 89/5/31

14. DATE OF REPORT *(Year, Month, Day)* 89/7/28

15. PAGE COUNT

16. SUPPLEMENTARY NOTATION

17. COSATI CODES

FIELD	GROUP	SUB-GROUP

18. SUBJECT TERMS *(Continue on reverse if necessary and identify by block number)*
Additive, Alkali, Alkaline-Earth, Ferrocene, Flame, Soot

19. ABSTRACT *(Continue on reverse if necessary and identify by block number)*

Research has been carried out to clarify the mechanisms responsible for the suppression of soot in flames by selected fuel additives. Measurements were limited to well-defined prevaporized liquid- and gaseous-fueled hydrocarbon/air flames. Emphasis was given to ferrocene in a diffusion flame fueled by prevaporized iso-octane, as well as to alkali and alkaline-earth additives in premixed ethylene/air flames. Nonperturbing laser optical diagnostic techniques were used to measure flame temperature, as well as to relate changes in soot particulate size, number density, and volume fraction to additive type and concentration. In addition, quartz probe sampling and gas chromatography were used to determine the additive's effect on soot precursor hydrocarbon and other species. For the diffusion flame, the time of the first appearance of soot is shortened when ferrocene is present. Following its appearance, the particulate's size and number density are perturbed by ferrocene in a somewhat complex manner in that increases and decreases are observed (contined on reverse side)

20. DISTRIBUTION/AVAILABILITY OF ABSTRACT
☒ UNCLASSIFIED/UNLIMITED ☒ SAME AS RPT. ☑ DTIC USERS

21. ABSTRACT SECURITY CLASSIFICATION Unclassified

22a. NAME OF RESPONSIBLE INDIVIDUAL Julian M Tishkoff

22b. TELEPHONE *(Include Area Code)* (202) 767-[redacted] 4935

22c. OFFICE SYMBOL AFOSR/NA

DD Form 1473, JUN 86 *Previous editions are obsolete.*

SECURITY CLASSIFICATION OF THIS PAGE
Unclassified

89 9 27 048

at early and late residence times, respectively. For the most part, ferrocene does not affect temperature or soot precursor chemistry, with the possible exception of marginal evidence that it accelerates acetylene oxidation. Ferrocene is very effective at late stages, appearing to enhance soot burnout. Attempts were not successful to find iron occluded by soot as a possible mechanism of enhanced soot oxidation. For the premixed flame, the efficiency of a given metal additive is dependent almost exclusively on temperature and the metal atom's ionization potential; the higher the temperature and the lower the ionization potential, the greater is the soot removal. As such, only the alkali metals were effective. For them, the perturbation of soot takes the form of decreased size and volume fraction and increased number density, the extent of the perturbation increasing with residence time. As above, the soot precursor chemistry is only marginally affected by the additive. The alkali metals remove soot by creating more smaller particulates, which then burn out more rapidly at a late stage; intervention at the precursor stage, may not be stated with certainty at this time.

R89–957464–F

Investigation of Fuel Additive Effects on Sooting Flames

TABLE OF CONTENTS

n For
A&I ☑
ed ☐
tion ☐
tion/
ility Codes
Dist
Avail and/or
Special
A-1

QUALITY INSPECTED 4

TABLE OF CONTENTS (continued)

APPENDICES

LIST OF ILLUSTRATIONS

LIST OF ILLUSTRATIONS (concentrations)

LIST OF ILLUSTRATIONS (concentrations)

ACKNOWLEDGEMENTS

I wish to thank Richard Bodurtha, Russell Cutting, David Kocum and David Santos for the technical assistance which they provided me at various times. I also wish to thank Robert Hall, Meredith Colket, and Bruce Laube for their essential contributions to temperature, soot precursor species and ESCA measurements, respectively. Also, I am very grateful to Laurence Boedeker for his design of the prevaporized-liquid fuel burner.

ABSTRACT

Under Contract F49620-86-C-0054 sponsored by the Air Force Office of Scientific Research, the United Technologies Research Center (UTRC) has conducted research to clarify the mechanisms responsible for the suppression of soot in flames by selected fuel additives. Measurements were limited to well-defined prevaporized liquid- and gaseous-fueled hydrocarbon/air flames. Emphasis was given to ferrocene in a diffusion flame fueled by prevaporized iso-octane, as well as to alkali and alkaline-earth additives in premixed ethylene/air flames. Nonperturbing laser optical diagnostic techniques were used to measure flame temperature, as well as to relate changes in soot particulate size, number density, and volume fraction to additive type and concentration. In addition, quartz probe sampling and gas chromatography were used to determine the additive's effect on soot precursor hydrocarbon and other species. For the diffusion flame, the time of the first appearance of soot is shortened when ferrocene is present. Following its appearance, the particulate's size and number density are perturbed by ferrocene in a somewhat complex manner in that increases and decreases are observed at early and late residence times, respectively. For the most part, ferrocene does not affect temperature or soot precursor chemistry, with the possible exception of marginal evidence that it accelerates acetylene oxidation. Ferrocene is very effective at late stages, appearing to enhance soot burnout. Attempts were not successful to find iron occluded by soot as a possible mechanism of enhanced soot oxidation. For the premixed flame, the efficiency of a given metal additive is dependent almost exclusively on temperature and the metal atom's ionization potential; the higher the temperature and the lower the ionization potential, the greater is the soot removal. As such, only the alkali metals were effective. For them, the perturbation of soot takes the form of decreased size and volume fraction and increased number density, the extent of the perturbation increasing with residence time. As above, the soot precursor

chemistry is only marginally affected by the additive. The alkali metals remove soot by creating more smaller particulates, which then burn out more rapidly at a late stage; intervention at the precursor stage, may not be stated with certainty at this time.

SECTION 1.0

INTRODUCTION

Particulate soot is a combustion product whose occurrence is highly undesirable in almost all instances. From the military's perspective, for example, soot creates a visible aircraft exhaust plume, thereby rendering the aircraft and its mission vulnerable to an adversary. Secondly, soot may shorten engine life by excessively increasing heat transfer to critical engine components. The use of fuel additives to control soot formation is a proven, effective approach to the problem. It is a simpler alternative than undertaking radical engine redesign for the purpose of reducing soot. The difficulty with additives is that their mechanism(s) of action are very poorly understood at present, which impedes much more effective and widespread use of them in fuels. The objective of this contract research, expressed in its simplest and most direct terms, was to seek to understand the latter mechanisms, and therefrom find ways to enhance and optimize fuel additive use for soot suppression.

In the recent past, experiments have been carried out to determine the soot suppressing properties of fuel additives in both small well-defined-laboratory flames as well as in more practical combustion media. With perhaps one or two exceptions, the past experiments have been very qualitative in nature, amounting to a cataloguing of the relative effectiveness of a large number of different additives. Moreover, the measurement techniques were either intrusive by nature or restricted to postflame analysis of soot with and without fuel additives present. Although this genre of additive research is useful in a practical sense, and is a reasonable point of departure for understanding additive behavior, it alone is insufficient for clarifying additive behavior in detail. In order for this to ensue, more comprehensive and specific measurements are required.

In order to address the needs mentioned above, the approach which was taken was to seek to comprehend the behavior of fuel additives in flames by relying upon non-intrusive and spatially precise laser/optical techniques, as well as probe sampling. More specifically, the techniques employed included: scattering/extinction of visible laser light to determine soot particulate size, number density and volume fraction with and without an additive present; quartz probe sampling of soot precursor species concentrations; a novel emission/absorption tomographic technique to determine flame temperature.

Unlike many past experiments, emphasis in this contract research centered on only a few different additives. Specifically, attention was given to alkali and alkaline-earth metals and to ferrocene. These metals were selected for study since, qualitatively, they were known from past gaseous- and liquid-fueled flame measurements to be effective soot suppressants in both research and practical media. Second, and equally important, details of their behavior were poorly understood.

SECTION 2.0

FERROCENE-SEEDED DIFFUSION FLAME

This section summarizes measurements of soot particulate and precursor species in a prevaporized iso-octane/air diffusion flame with and without ferrocene present as a fuel additive. The principal experimental techniques which are described include Mie scattering for soot particulate size, number density and volume fraction determination, and gas chromatographic analysis of quartz probe collected samples for the determination of soot precursor species concentrations. In addition, a description of an infrared tomographic technique for temperature measurement is given, as well as a description of an ESCA (electron scattering for chemical analysis) analysis of solid soot effluent chemical composition. Data are presented which give the effect of ferrocene seeding on the several parameters mentioned above as determined by the techniques which have been indicated. The section concludes with a discussion of results in relation to understanding the process by which ferrocene suppresses soot emission from a diffusion flame.

2.1 Background

Ferrocene, or dicyclopentadienyl iron [$(C_5H_5)_2Fe$], is a transition metal arene complex which possesses synthetic accessibility, chemical versatility and, in addition, remarkable structural stability (Ref. 2.1). Perhaps for this reason ferrocene is the best known and the most often investigated organometallic compound. The crystal structure of ferrocene is a sandwich configuration in which the two C_5 rings are planar, parallel to each other, and symmetrically located with respect to the C_5H_5-Fe-C_5H_5 axis. More specifically, the antiprismatic sandwich structure has been demonstrated by X-ray crystallographic analysis, with the C-C bonds in a given ring and all C-Fe bonds being equidistant. For the work reported here, the properties of ferrocene of particular interest are its solubility in conventional liquid fuels, as well as its thermal stability and vapor pressure. Ferrocene is soluble in a wide variety of organic solvents, albeit to a varying degree depending upon the particular solvent selected (Ref. 2.2). Its solubility is greatest in aromatic liquids. Since conventional jet fuels all have some aromatic character, ferrocene is soluble in them as well, which enhances the feasibility of ferrocene use to suppress soot in practical, large scale combustion devices. For the work reported here, there was no difficulty in obtaining the 0.3% (wght.) concentration of ferrocene in iso-octane sufficient to observe measurable suppression of soot emissions. Ferrocene is a small, strongly bound ligand. Very low pressure pyrolysis data have shown that ferrocene decomposition occurs only at temperatures of 1120°K and above (Ref. 2.3). Since in this work the ferrocene/iso-octane mixture is heated to only 125°C, or just above the 98-99°C b.p. of the fuel, the ligand's stability is not a problem. The vapor pressure of ferrocene is high even at very modest temperatures (Ref. 2.4). This is a property crucial to the success of the experiment reported here since without it there would be no hope of observing an additive induced perturbation of the emitted soot. Indeed, during this work an unsuccessful attempt was made to observe the effect of a cerium hexanoate additive on soot. This failure was due most likely to the very low vapor pressure of the latter cerium compound at or near the b.p. temperature of the fuel. At 125°C, the vapor pressure of ferrocene is 15 Torr (Ref. 2.4) or more than high enough to influence soot emissions.

Iron compounds, and ferrocene in particular, have been used rather extensively in the combustion area for quite some time. Some of the important uses of ferrocene as a fuel additive are given in Fig. 2.1. The last entry lists the thermochemical properties of ferrocene which make it particularly attractive as a fuel additive. This issue has been dealt with in more detail in the paragraph above. The first entry in Fig. 2.1 summarizes the diverse media in which ferrocene has been observed to be a smoke (or soot) inhibitor. The list encompasses gaseous and liquid fuels, combustion at atmospheric and higher pressure, and both laboratory and practical media. In one or two instances the experiments have been

SIGNIFICANCE OF FERROCENE AS A FUEL ADDITIVE

(ferrocene = dicyclopentadienyl iron)

- Smoke inhibitor
    - Jet and domestic burners
    - Flow reactor acetylene pyrolysis
    - Diesel combustion of petroleum hydrocarbons
    - Aircraft and utility gas turbine engines
    - Poly (vinyl chloride) combustion
    - Laboratory diffusion flames
- Gasoline antiknock agent
- Solid propellant burning rate enhancer
- Soot ignition temperature reducer
- Ferrocene is readily synthesized, air stable, non-toxic and soluble in practical fuels

RA2745TX.018

Fig. 2.1

done in sufficient detail to permit some very tentative conclusions concerning operative mechanisms. For example, the effect of ferrocene on acetylene pyrolysis has been presumed to be twofold (Ref. 2.5). The initial effect is decomposition of ferrocene to yield cyclopentadienyl radicals which enhance acetylene reaction, decomposition and soot formation. Secondly, however, as iron deposits form on the walls of a flow reactor, quenching of soot formation occurs. In the area of diesel research, the effectiveness of ferrocene as a soot suppressant has been compared for different hydrocarbon fuels each containing the same 0.1 weight percent ferrocene concentration (Ref. 2.6). Listed by fuel, the relative effectiveness of ferrocene in decreasing order of importance was: aromatics > naphthenes > alkanes. Along similar lines, a recent U. S. patent disclosure describes the use of 10-15 ppm ferrocene in a fuel to "condition" diesel engines (Ref. 2.7). Conditioning consists of keeping the cylinder walls free of carbon deposits, and formation of iron oxide on the walls is presumed to account for the catalytic removal of carbon. In addition to the fairly systematic studies in flow reactors and diesel engines mentioned above, other useful measurements have been made in gas turbine engines (Ref. 2.8) and laboratory diffusion flames, where the latter laboratory measurements have been carried out principally at UTRC under both corporate and AFOSR support (Ref. 2.9).

The previous ferrocene measurements done at UTRC served to establish the soot reducing properties of the latter organometallic when added to two dissimilar laboratory diffusion flames. In one case, ferrocene measurements were done with a wick flame. The burner, in this case, was exceedingly simple in design. A small bottle, having a roughly 50 ml capacity, was filled with liquid fuel, a wick was passed through a narrow opening in the bottle cap, and the evaporating fuel was then ignited. For this wick flame, the sooting which occurred for a 5/1 iso-octane/toluene fuel mixture without additives present was compared with the case in which ferrocene was added to the fuel in varying, small concentration. For 0.25% ferrocene by weight, a heavy soot plume was suppressed as determined by visual observation. The wick flame measurements were valuable in that the significance of ferrocene as a soot suppressant was made very evident. The difficulty with a burner of this type is, however, that fundamental combustion parameters such as fuel and additive type, fuel flow rate and additive concentration, and flame temperature are not easily varied. It is for this reason that emphasis was shifted to a prevaporized fuel burner having more flexibility. With it, it was possible not only to replicate the wick flame data, but also to better control the fuel flow rate and thereby cause the unseeded flame to operate either above or below its smoke-point. In addition, some preliminary low-spatial-resolution Mie scattering measurements were made with this burner which demonstrated that soot suppression was the result of particulate size and number density reduction by ferrocene at a late combustion stage.

The preliminary work mentioned above has been described previously (Ref. 2.9). In this work, the ferrocene measurements have been refined and their scope extended. First, more detailed, spatially accurate measurements have been made of the effect of ferrocene on soot size, number density and volume fraction. Second, soot precursor species concentrations have been determined, with and without ferrocene present, via gas chromatographic analysis of samples collected with a quartz probe. Third, the possible perturbation of flame temperature by the additive has been examined using a novel infrared tomographic temperature measurement technique. Finally, an attempt was made to collect and analyze the solid effluent in the post flame zone so as to determine the final chemical state of the iron and its physical (or spatial) relationship, if any, to the particulate carbon. These efforts are described in full detail in the discussions below.

2.2 Burner and Fuel/Additive Feed

The burner used in the experiments reported here is shown in Fig. 2.2. Liquid fuel at room temperature enters the burner assembly via a 30 cm long x 12 mm i.d. stainless steel

PREVAPORIZED-FUEL DIFFUSION FLAME BURNER

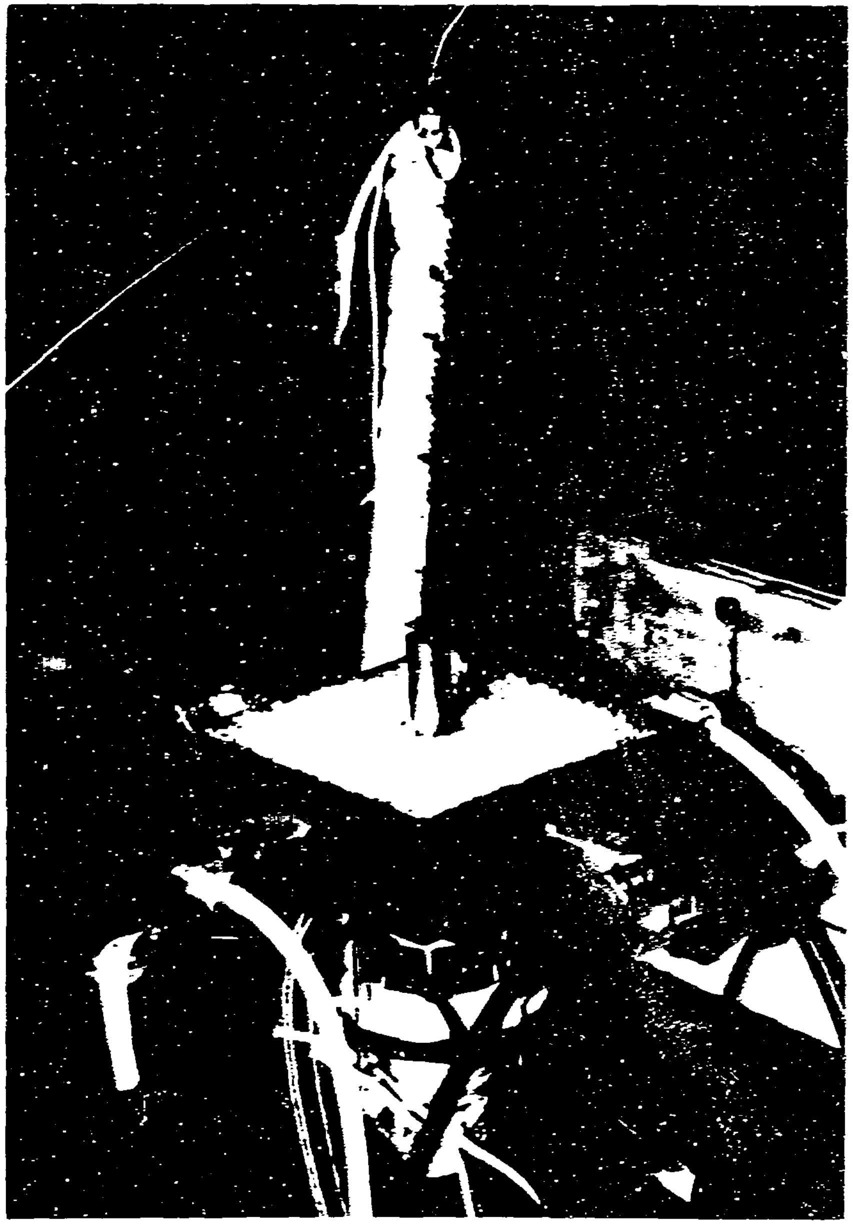

89—7—41—6

2.2

vaporizer tube packed almost completely with 3 mm diam. stainless steel spheres. Heat is applied to this tube by a tape tightly wound around it so as to create a temperature of about 125°C. This temperature is maintained constant by an OMEGA Engineering Model 49 controller. The latter temperature is sufficient to fully vaporize the fuel which has a b.p. of about 98-99°C. The liquid fuel is fed into the vaporizer at a very slow 0.1 to 0.2 cc/min rate, and the resulting fuel vapor is purged gently through the burner with a 50-60 cc/min flow of nitrogen. The fuel vapor enters the combustion zone through a 15 cm long x 11 mm i.d. nickel tube attached to the end of the vaporizer. Then, the fuel is mixed with air provided by an air plenum concentric to the nickel tube. Prior to mixing with the fuel, the air is passed through a bed of 3 mm diam. glass beads and then a 12 mm thick piece of honeycomb, both of which are located within a 10 x 10 cm square enclosure extending about 40 cm above the fuel tube lip. The enclosure (or shroud) has quartz windows on all four sides to accommodate Mie scattering and other in-situ optical measurements. Additional external heating beyond that described is required in order to ensure that fuel vapor does not condense out on the walls of the nickel tube. To this end, the tube is isolated from the air plenum by air gaps using a thin shell support structure. A thin cartridge heats the top portion of the nickel burner tube directly through an intermediate slip-fit slotted plug. The cartridge heater and its leads are isolated from the hot fuel vapor, and the leads are brought out through a feed-through at the bottom of the nickel tube. In addition to the cartridge internal to the nickel tube, the lower part of the tube is heated by attaching a band heater to an intermediate thick nickel ring firmly clamped to the fuel tube. The foregoing, somewhat complex burner construction results in a smooth, roughly 1 minute transit of fuel vapor to the combustion zone where a reasonably stable flicker-free axisymmetric diffusion flame results.

A schematic diagram of the complete burner and fuel/additive feed system is given in Fig. 2.3. The rotary fluid switch is used to select among reservoirs containing pure fuel or

PREVAPORIZED FUEL BURNER

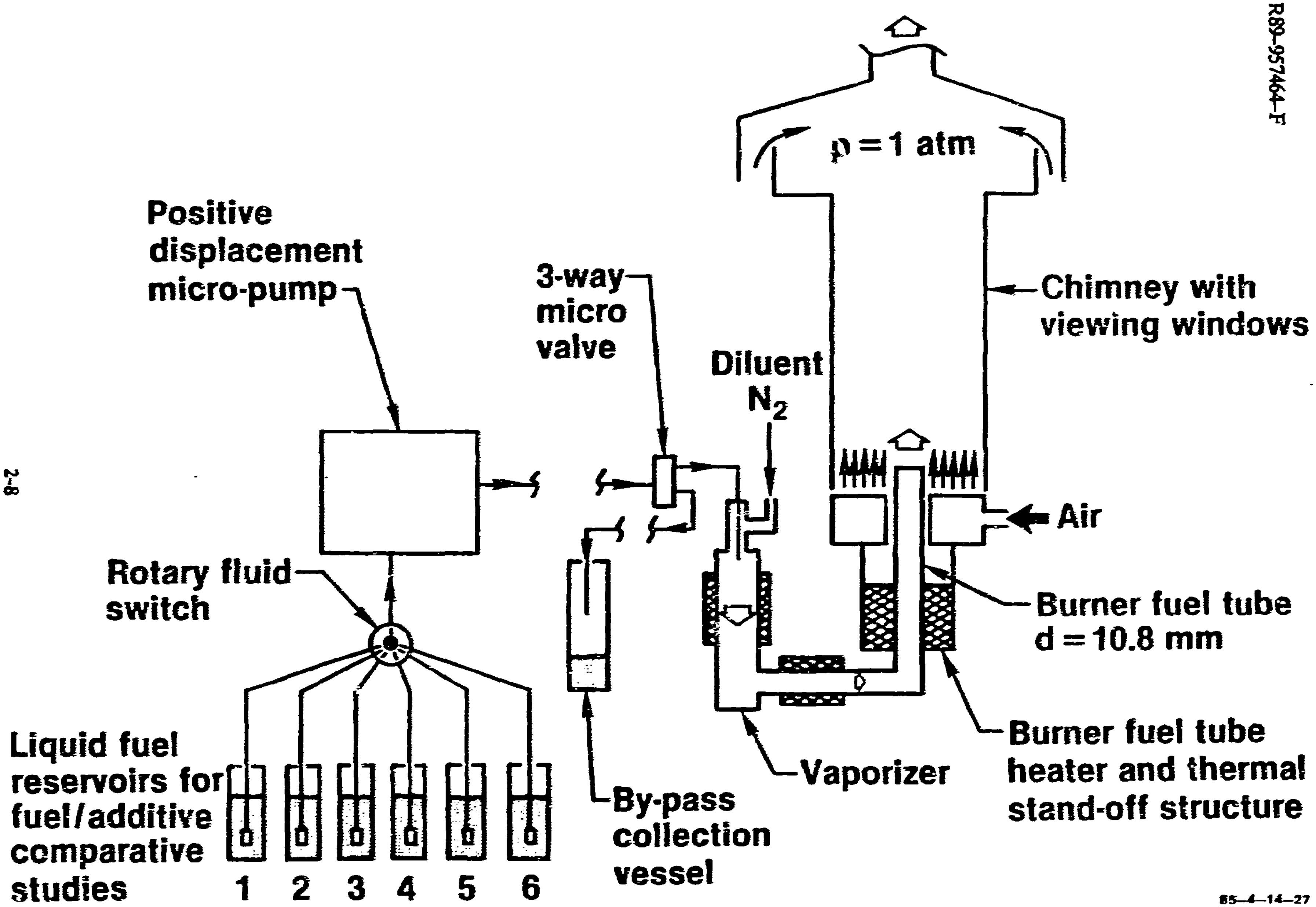

85-4-14-27

Fig. 2.3

those containing iso-octane in which ferrocene is dissolved at various concentrations. The function of the 3-way micro-valve and by-pass system is to provide a means of rapidly changing from one reservoir to another. Normally the Gilson Model 302 positive displacement micro-pump is operated at a very low flow-rate when a flame is present; however, it is operated at a high flow-rate when the 3-way micro-valve is used. The depiction of the vaporizer, fuel tube, external heating, air plenum and chimney in Fig. 2.3 are only schematic. For more and accurate details, refer to the preceding paragraph.

By flowing iso-octane (2, 2, 4 - trimethylpentane) at roughly 0.2 cc/min through the burner, the yellow flame shown in the left half of Fig. 2.4 was produced. This flame (no additive) is above its smoke point and a pronounced plume of soot emanates from its tip. Unfortunately, this is not convincingly evident in Fig. 2.4 due to limitations inherent in simultaneously photographing a black effluent and the flame's bright emission, but in the laboratory the plume is clearly visible. The right side of Fig. 2.4 shows the same flame when 0.3% (by wght.) ferrocene is present in the starting fuel. In this case, the soot plume is not present, having been suppressed by the ferrocene. Equivalently, one may state that the additive has raised the threshold value of fuel flow required for soot emission from the flame tip. Detailed Mie scattering measurements on these and similar flames are described below in detail.

2.3 Light Scattering and Particulate Sizing

Soot is measured with and without additives present using the 10 nsec, 10 pps Nd:Yag laser in Fig. 2.5, as well as the two detection arms oriented at 20 and 160° with respect to the incident light direction. The Pellin-Broca prism, PBP, serves two purposes. It rotates the 5320 Å 2x Nd:Yag laser output by 90°, and refracts the 10,600 Å 1x Nd:Yag residual output into the light trap, T. The half-wave plate, $\lambda/2$, rotates the polarization axis of the laser to a direction normal to the scattering (or Fig. 2.5) plane. The arms at 20 and 160° record the

SOOT REDUCTION WITH FUEL ADDITIVE

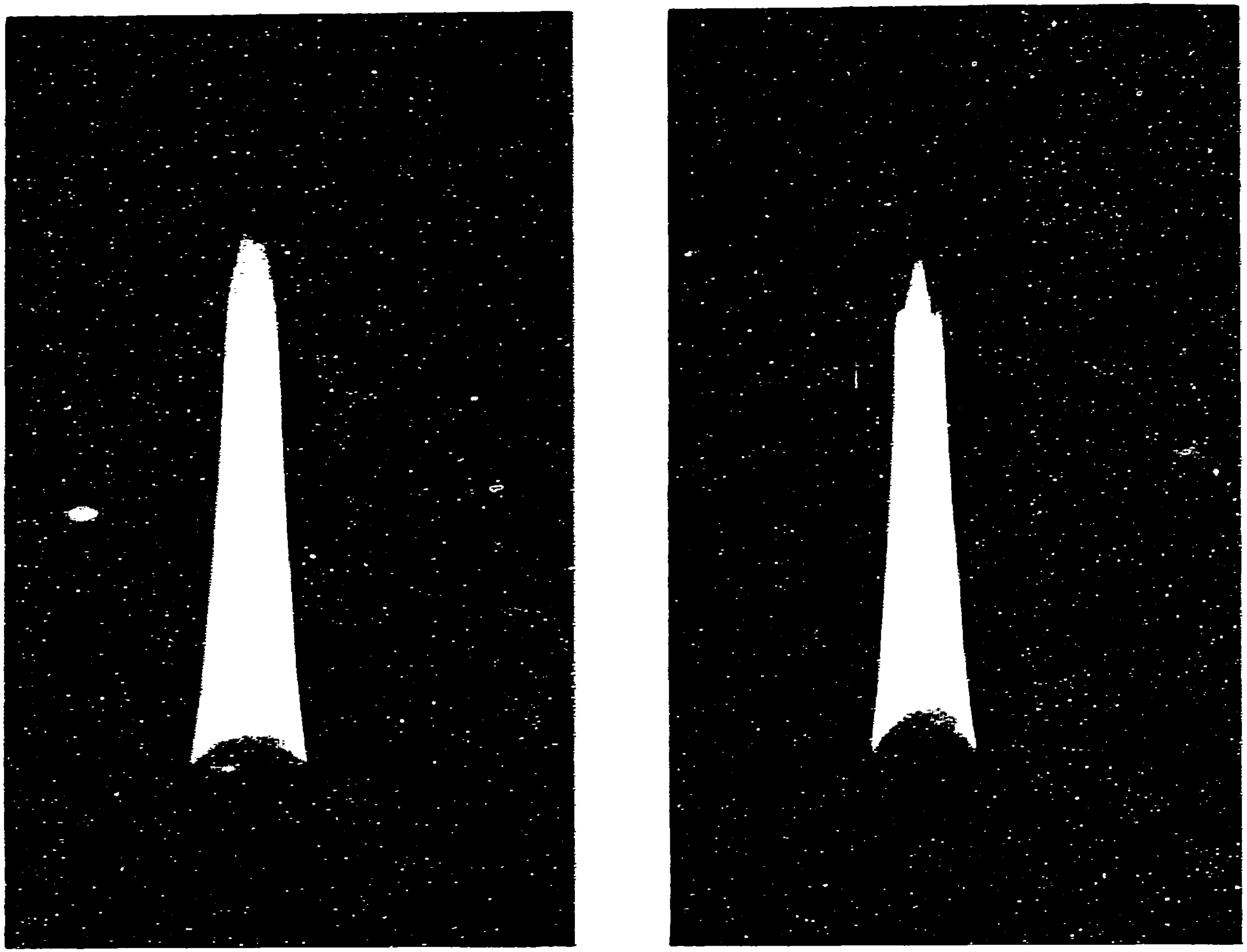

No additive

0.3% ferrocene

SOOT MEASUREMENT SCHEMATIC

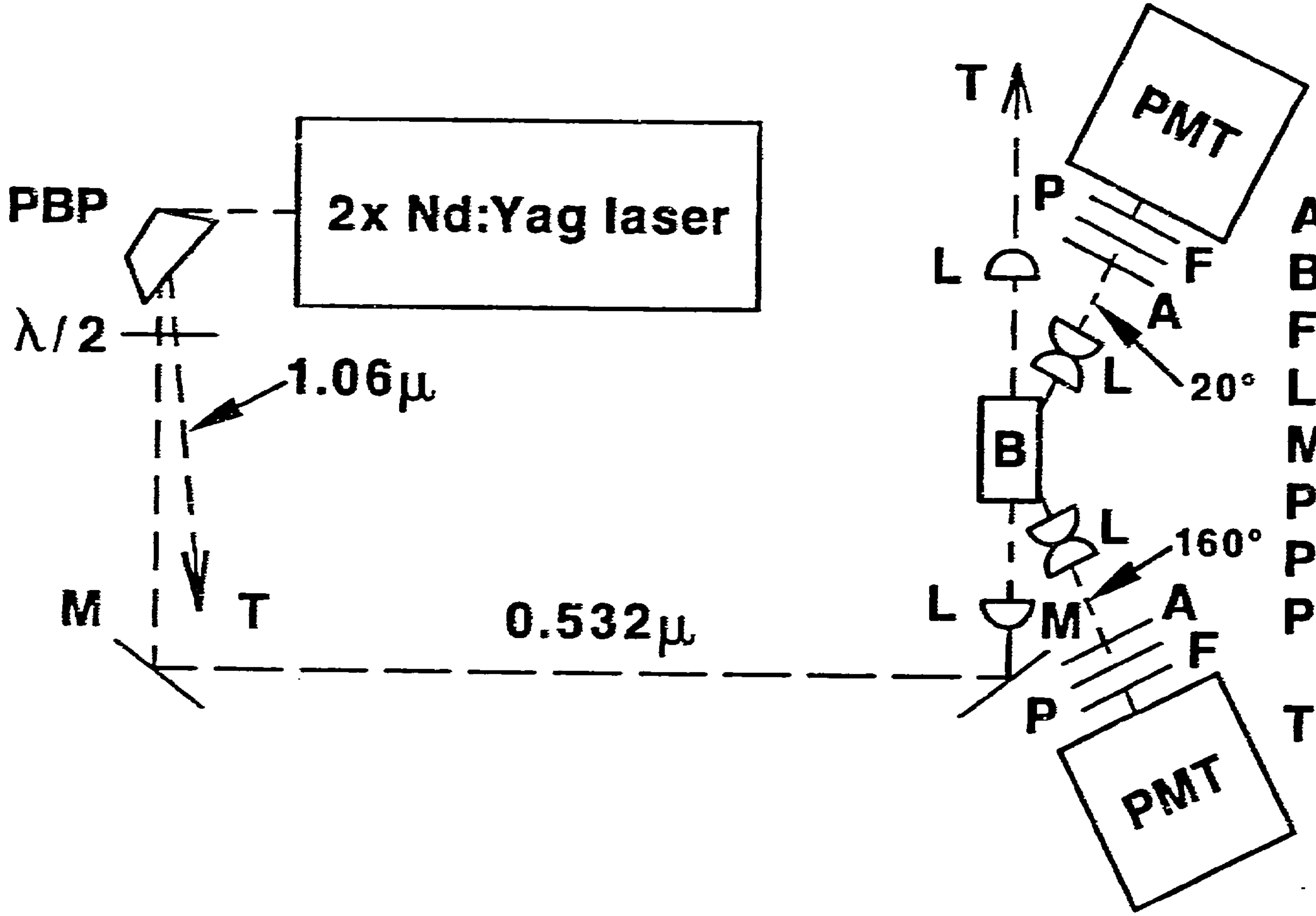

A, aperture
B, burner
F, optical filter
L, lens
M, mirror
P, polarizer
PBP, prism
PMT, photo-multiplier
T, light trap

RA2745TX.012

Fig. 2.5

light Mie scattered by the soot particulates. Each detection arm has an aperture, A, and lenses, L, to define both the optical sample length and the light collection solid angle, a polarization analyzer, P, aligned with the laser polarization axis, a narrow-band filter, F, centered at 5320 Å, and a photomultiplier, PMT. Electronic processing of all PMT signals is done with EG&G/Princeton Applied Research boxcar averagers not shown in Fig. 2.5. The optics in Fig. 2.5 are such that the soot sample volume is approximately a 0.75 mm long x 0.025 mm diam. cylinder.

Soot size, number density and volume fraction are inferred from the light intensities at the PMT's. The soot diameter, D, is evaluated from the 20/160° intensity ratio (Ref. 2.10). Having D, the number density, N, is obtained from the absolute intensity at either angle. Then, the volume fraction, f_v, is calculated from, $f_v = (\pi D^3/6)N$. In the Mie analysis, particulate nonsphericity is neglected, a monodisperse size distribution is assumed, and the refractive index is taken to be, $\hat{n} = 1.94 - 0.66\,\hat{i}$ (Ref. 2.11). In earlier work (Ref. 2.10), it was shown that an unambiguous size distribution determination is not possible for small, high number density nonspherical particulates whose refractive index is not accurately known. This accounts for the monodisperse assumption above, which in fact has no significant bearing in relation to understanding additive behavior.

Soot parameters were measured for ferrocene seeded and unseeded iso-octane/air flames operating both below and above their characteristic smoke points. Data which show the effect of ferrocene on soot for below smoke-point operation are given in Figs. 2.6, 2.7 and 2.8. It is evident from Fig. 2.6 that ferrocene may act so as to either increase or decrease soot volume fraction depending upon its location. Not far above the burner lip near z = 10 mm, there appears to be a soot increase with ferrocene present, whereas near the flame tip the opposite is the case. If notice is taken that the vertical scale in Fig. 2.6 is logarithmic, then it follows that the perturbation by ferrocene is quite substantial. Since as

ADDITIVE EFFECTIVENESS ON SOOT VOLUME FRACTION

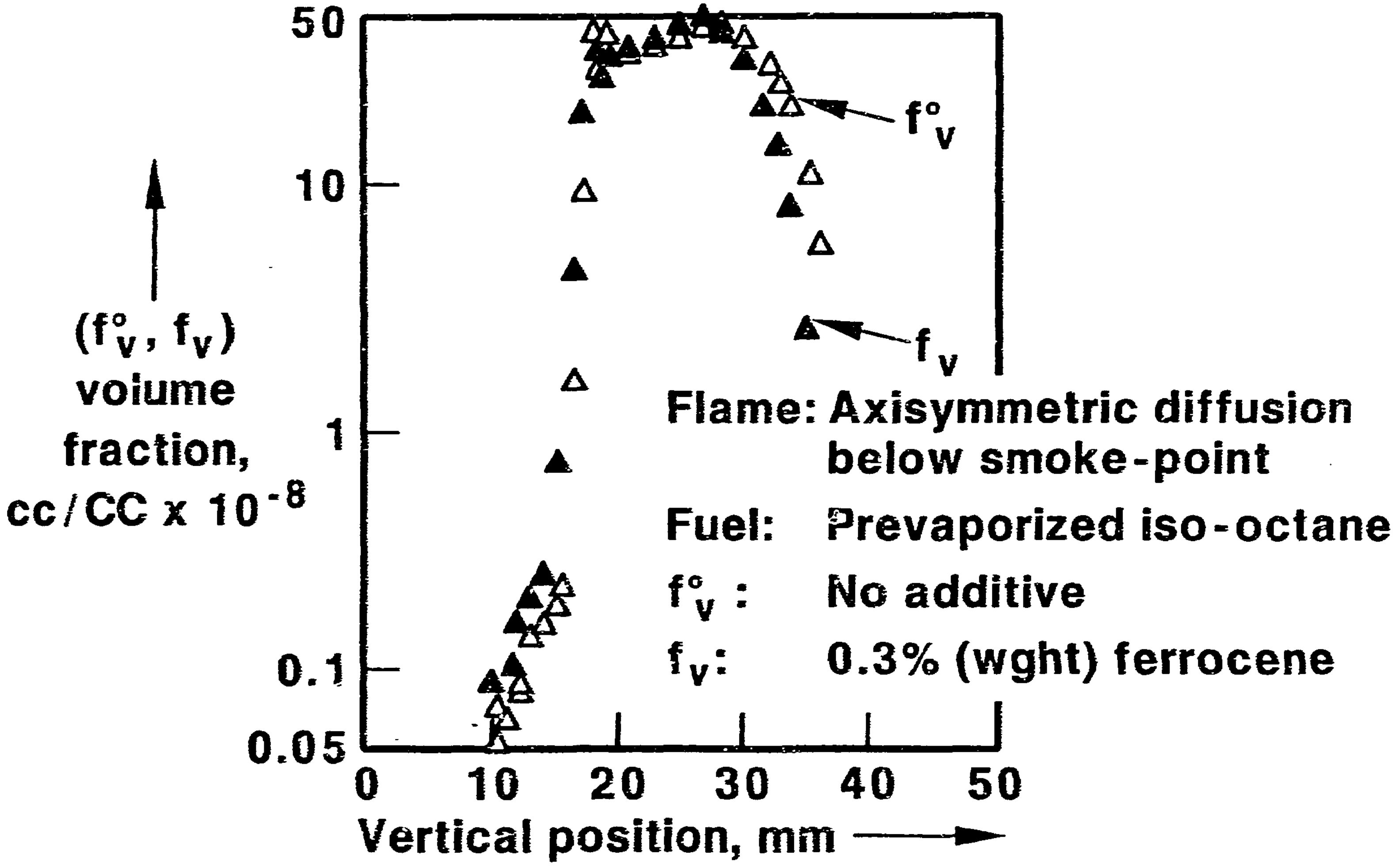

Flame: Axisymmetric diffusion below smoke-point

Fuel: Prevaporized iso-octane

f°_{v} : No additive

f_{v}: 0.3% (wght) ferrocene

RC2745TX.005

Fig. 2.6

Fig. 2.7

ADDITIVE EFFECTIVENESS ON SOOT DIAMETER

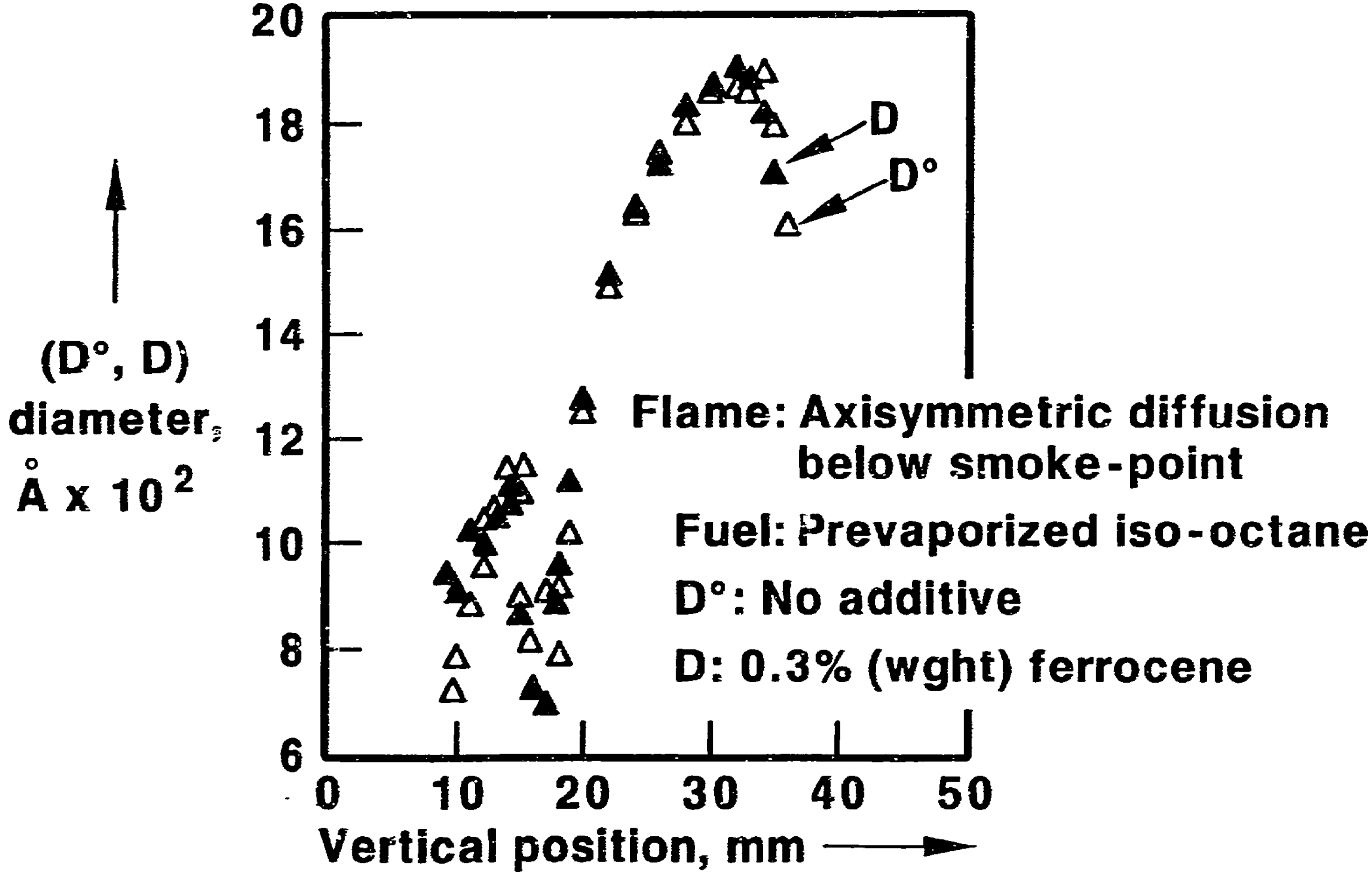

Flame: Axisymmetric diffusion below smoke-point

Fuel: Prevaporized iso-octane

D°: No additive

D: 0.3% (wght) ferrocene

RC2745TX.006

ADDITIVE EFFECTIVENESS ON SOOT NUMBER DENSITY

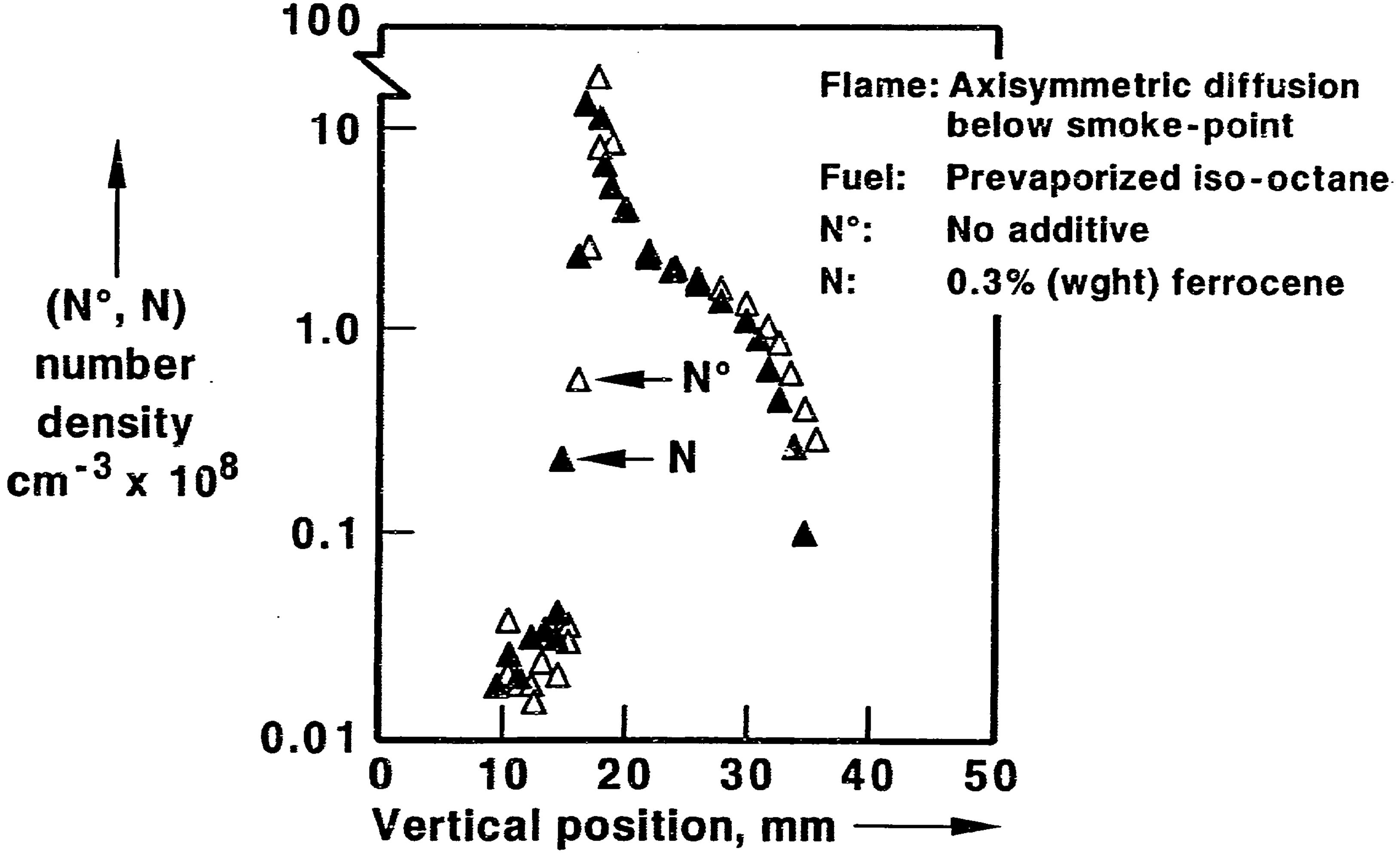

RC2745TX.007

Fig. 2.8

outlined above the volume fraction is not a directly measured parameter but rather is computed from diameter and number density, the ferrocene perturbation should be reflected in the latter parameters as well. Indeed, this is confirmed in Figs. 2.7 and 2.8, but unfortunately with significantly less clarity. At late stages near $z \geq 30$ mm, the data are relatively precise due to heavy soot loading there and the resulting intense light scattering signals. On the other hand, near $z = 10$ mm where the loading is a factor of 500 smaller, the data are more susceptible to residual instabilities (flicker). In addition, the "double hump (peak)" feature evident in both Fig. 2.7 and 2.8 is an additional uncertainty. Whether this feature is real or instrumental is not entirely clear, save to point out that it was not observed for very similar above the smoke-point data to be discussed below. Due to these uncertainties, the "D" and "N" data near $z = 10$ mm cannot be interpreted as evidence for ferrocene induced soot enhancement. Near $z = 30$ mm, however, the interpretation is clearer; namely, soot suppression is due primarily to N reduction and secondarily to a decrease in diameter, D. It would appear, then, that the role of ferrocene at a late combustion stage is to enhance the oxidation of soot (i.e., soot burnout) already present in the unseeded flame.

The measurements discussed in the preceding paragraph were taken at points along the z- or vertical axis of the flame. As mentioned, these were not firmly supportive of soot enhancement. In order to confirm ferrocene enhancement at small "z", measurements were made at lateral positions coincident with peak soot volume fraction for $z = 5$, 7, 9 and 11 mm. The latter peak positions were selected in the expectation that probing could be done close to the burner lip while retaining reasonably intense scattered light signal intensities. Moreover, by staying away from the geometric center of the fuel tube, spurious signals due to unvaporized fuel droplets could be avoided. The results of these measurements are given in Table 2.1 where again the clearest evidence for ferrocene enhancement of soot is in the volume fraction data. Although they contain some

TABLE 2.1

Soot size (D^o,D), number density (N^o,N), and volume fraction (f_v^o, f_v) at a lateral position coincident with the volume fraction peak for each of the z-positions given below. Data are for unseeded (D^o, N^o, f_v^o) and seeded (D, N, f_v) otherwise identical flames operating below their smoke-points.

z (mm)	D^o,D (Å)	N^o,N (cm^{-3}) x 10^8	f_v^o, f_v (cm^{-3}/CM^{-3}) x 10^{-7}
5	668, 751	0.76, 1.50	0.12, 0.33
7	967, 1036	4.46, 4.94	2.11, 2.88
9	1061, 1168	9.98, 8.71	6.25, 7.26
11	1586, 1519	2.82, 5.52	5.89, 10.13

irregularities, the data for D and N are in general supportive (as they must be!) of the volume fraction results. The one or two inconsistencies are due to unsteady scattered light signals caused by slight spatial wandering of the very thin, < 1 mm wide, reaction zone which is very nearly coincident with the location of the volume fraction peak. In order to rule out the possibility that the enhancement in Table 2.1 was due to soot promotion by the dicyclopentadiene product of ferrocene decomposition, measurements were repeated for a dicyclopentadiene seeded flame, where the mole fraction of the latter present in the fuel ($=1.86 \times 10^{-3}$) was the same as that for the ferrocene case. For $z = 5$ mm and a lateral position corresponding to peak volume fraction, no measurable effect of the dicyclopentadiene on sooting was observed.

Data were obtained as well for the flame operating above its smoke-point. This mode of operation was achieved quite simply by adjusting the positive displacement micro-pump so as to increase the rate of liquid fuel flow into the vaporizer tube. This produced the flame in Fig. 2.4 referred to above. The data which give the effect of ferrocene on the above the smoke-point flame are shown in Figs. 2.9, 2.10 and 2.11. In this case, the peak volume fraction near $z = 60$ mm in Fig. 2.9 is roughly a factor of four larger than the corresponding peak in Fig. 2.6. This excess of soot enhanced the scattered light signals and, hence, made it possible to observe the influence of ferrocene at and near the flame tip very clearly. It is evident from Figs. 2.9, 2.10 and 2.11 that the volume fraction decreases due to a ferrocene induced decrease in both size and number density. For this flame, no serious attempts were made to document ferrocene effects in the region $z = 5$ to $z = 15$ mm. This decision was made for two reasons. First, there is no reason to expect that the data would differ from those taken for the flame below its smoke-point, where the latter data were, in addition, very difficult to obtain. Second, it seemed more interesting to make measurements even lower in the flame, preferably in a zone where particulates are first formed. These efforts yielded some extremely interesting results which are described immediately below.

ADDITIVE EFFECTIVENESS ON SOOT VOLUME FRACTION

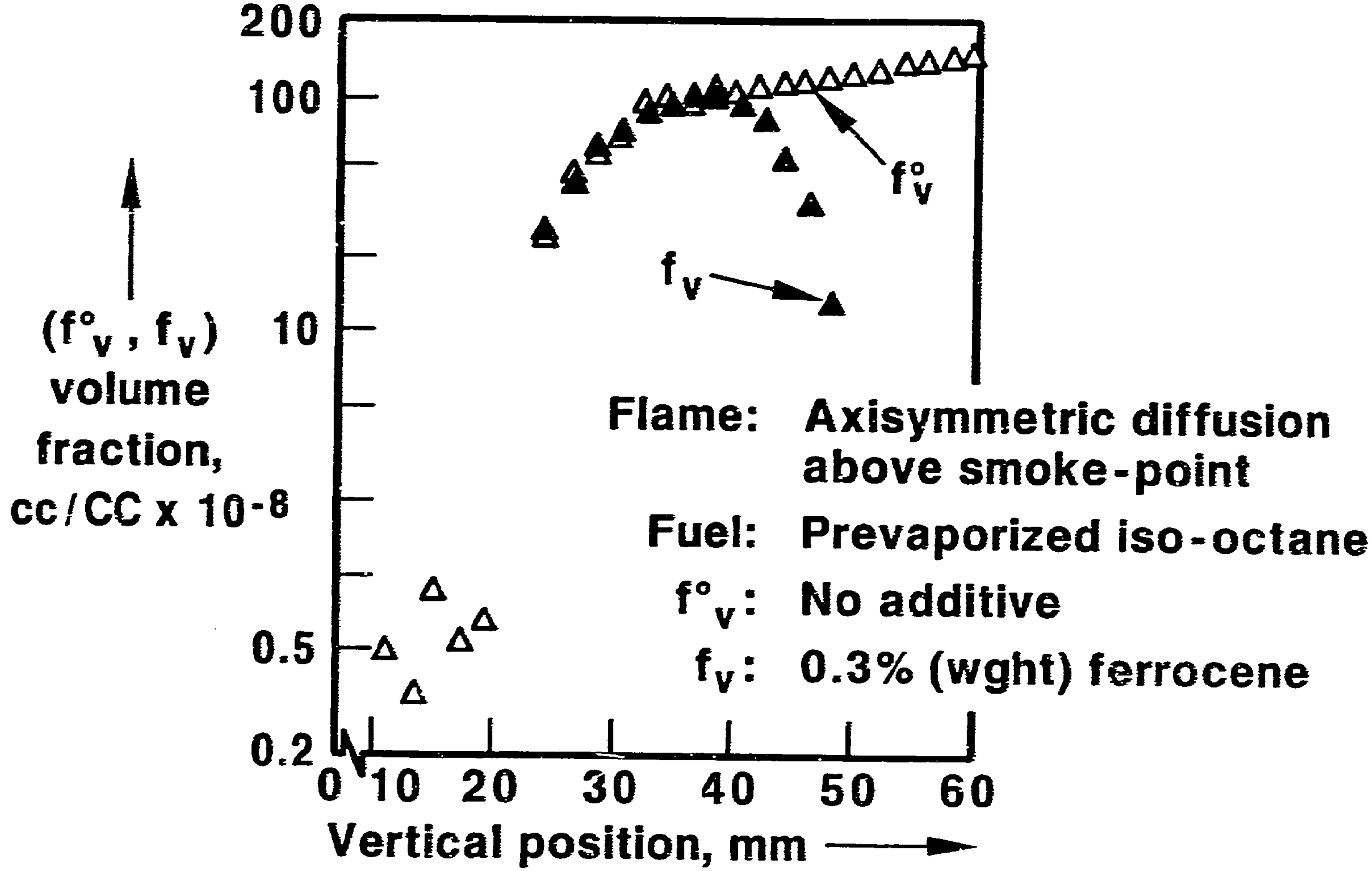

Flame: Axisymmetric diffusion above smoke-point

Fuel: Prevaporized iso-octane

f°_v: No additive

f_v: 0.3% (wght) ferrocene

RC2745TX.012

Fig. 2.9

ADDITIVE EFFECTIVENESS ON SOOT DIAMETER

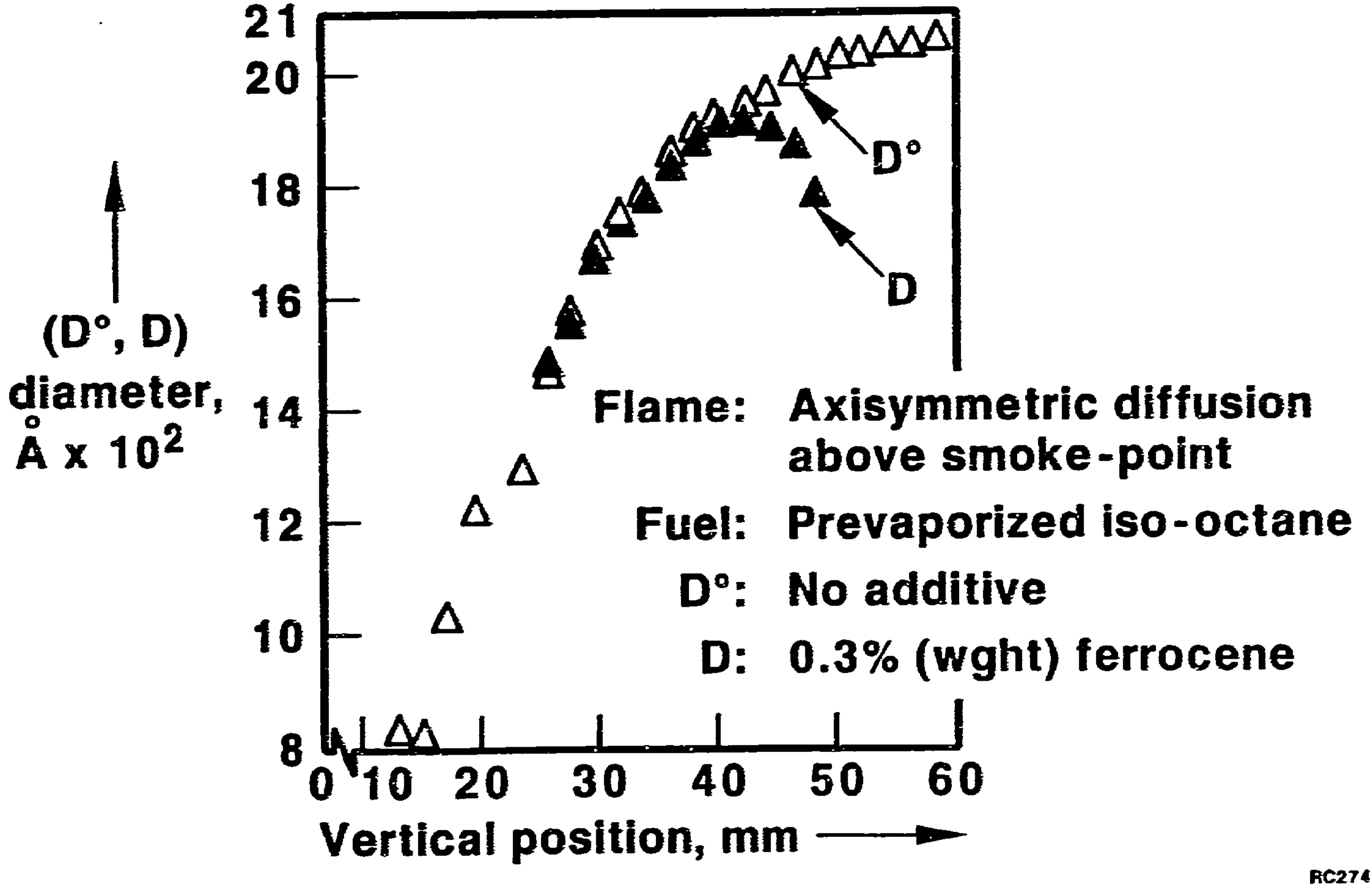

RC2745TX.013

Fig. 2.10

Fig. 2.11

ADDITIVE EFFECTIVENESS ON SOOT NUMBER DENSITY

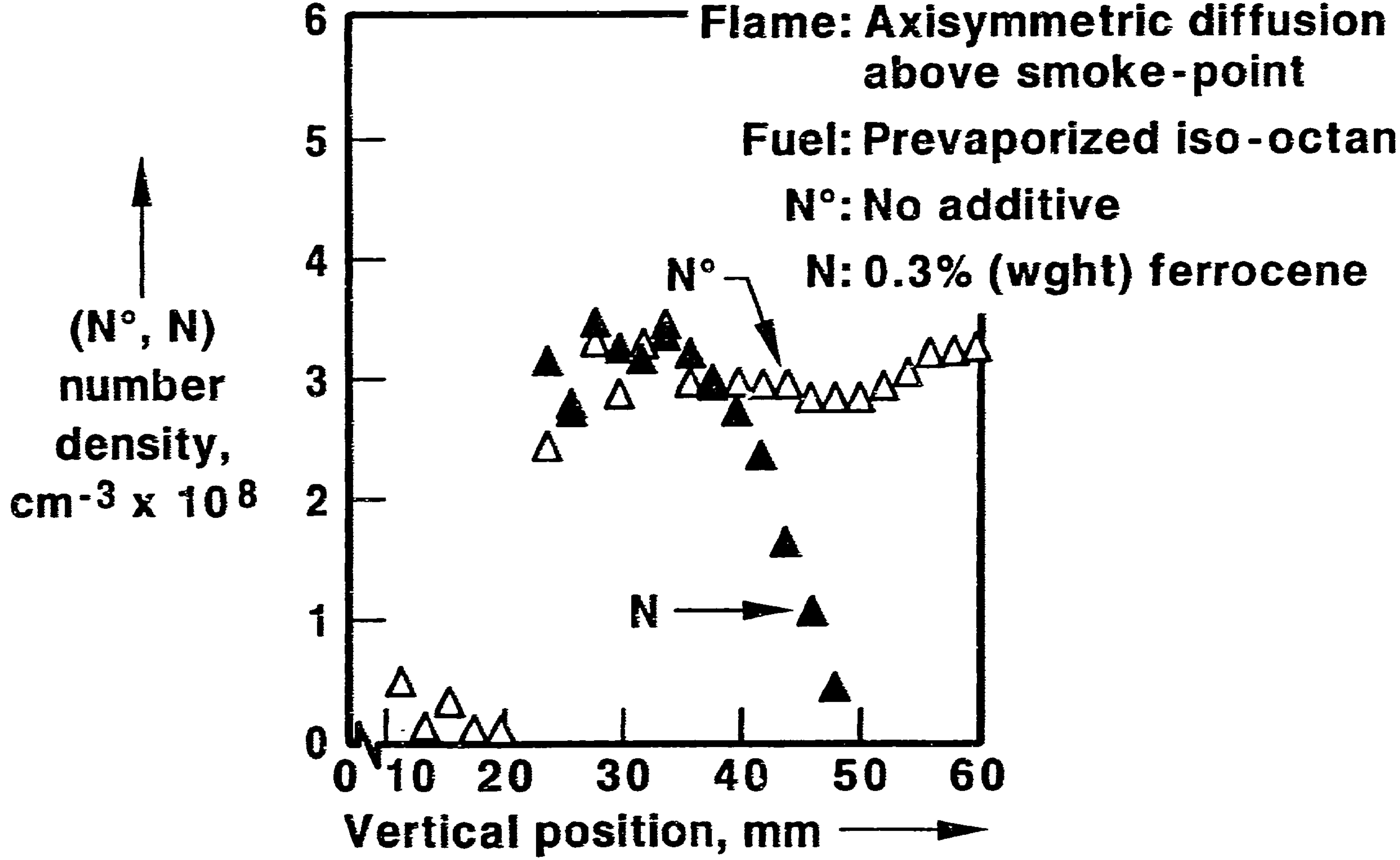

RC2745TX.011

An example of ferrocene effects at an early combustion stage is shown in Fig. 2.12. These data give measured scattered intensities at a 20-degree scattering angle, and for a fixed height of $z = 4$ mm and variable x-position. In Fig. 2.12a there are two signals. The first at $x = 0$ is due to unvaporized fuel and is not of immediate interest; the second between $x = 4$ and 5 mm is the first detectable soot signal. In other words, for the unseeded flame soot first appears between $x = 4$ and 5 mm at a height of $z = 4$ mm. When the flame is seeded with ferrocene and the x-traversal is repeated, the data are decidedly different as indicated in Fig. 2.12b. The cause for enhancement at $x = 0$ is unclear, but this signal is probably not relevant to additive behavior vis-a-vis soot. The signal near $x = 3$ mm is new. As will be shown, it is present at reduced intensity even before soot inception, i.e., at $z < 4$ mm. It is spatially separated from the soot, and will be shown to be due to solid Fe_xO_y formation. As in Fig. 2.12a, the signal between $x = 4$ and 5 mm in Fig. 2.12b is due to soot. With the ferrocene present, however, its magnitude exceeds that of its counterpart in the unseeded flame. This is fully consonant with $10 < z < 15$ mm in Fig. 2.6 and the discussion above in which the point was made that ferrocene has the capacity to enhance soot formation at early combustion stages. Equivalently, if one were to scan the flame horizontally and at the same time probe for scattered light at successively increasing fuel residence times, then a seeded flame would yield a signal at an earlier time than would the same flame with no ferrocene present.

In order to gather more evidence for solid Fe_xO_y formation, the following data were taken. Scans were made for seeded flames at $z = 2$ mm, i.e. before soot onset, with and without a trace of added O_2 present. The results of these measurements are given in Fig. 2.13. In Fig. 2.13a, the signal is measured at a 20-degree scattering angle and for a $z = 2$ mm vertical position. In Fig. 2.13b, conditions are the same except for the addition of a 13 cc/min flow of O_2 to the fuel/N_2 stream. The increase of signal intensity is evident. Based on both the large magnitude of the 20-degree signal (as compared, for example, to

LATERAL DEPENDENCE OF SCATTERED LIGHT INTENSITY

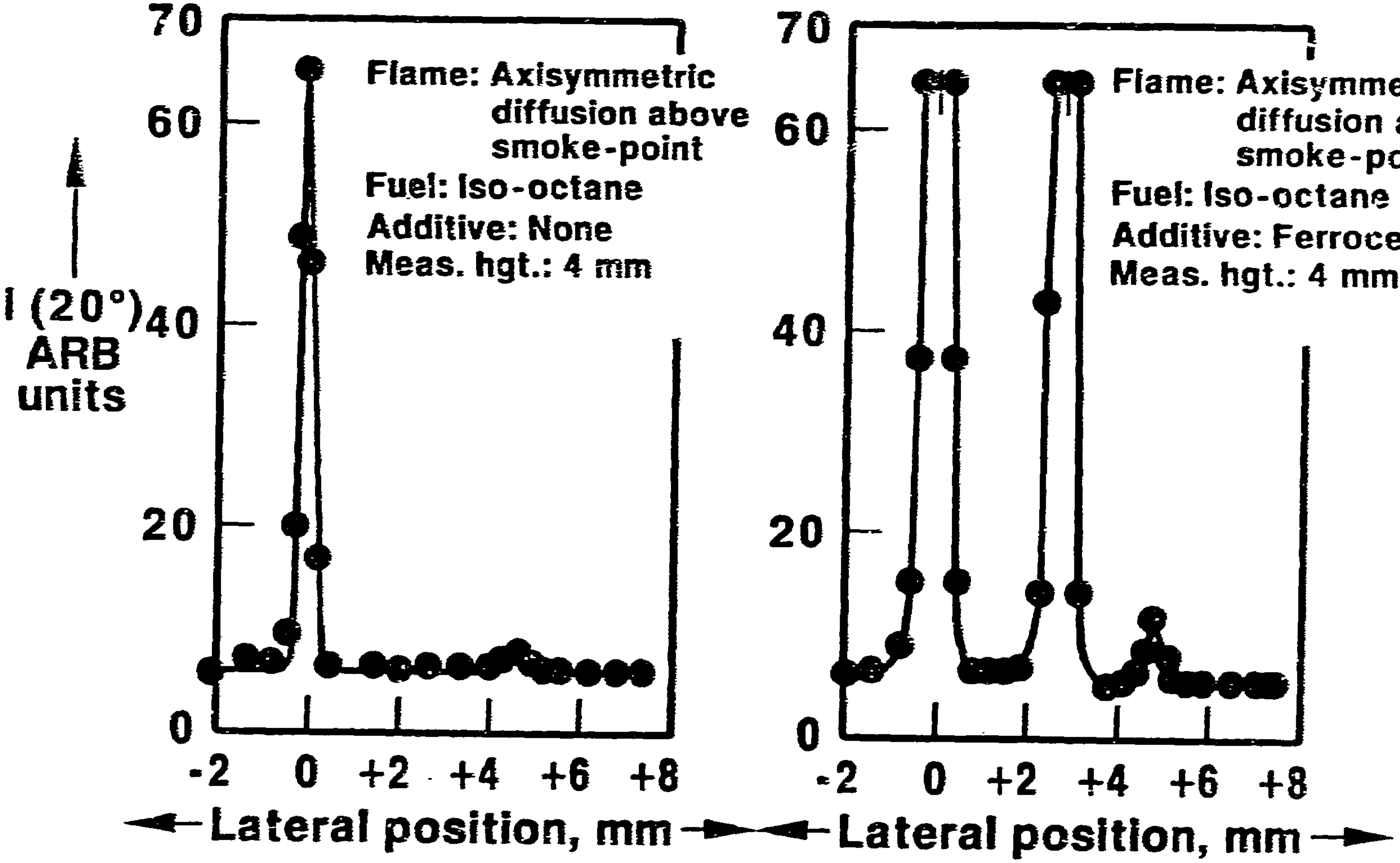

(a)

(b)

RA2745TX.010

Fig. 2.12

LATERAL DEPENDENCE OF SCATTERED LIGHT INTENSITY

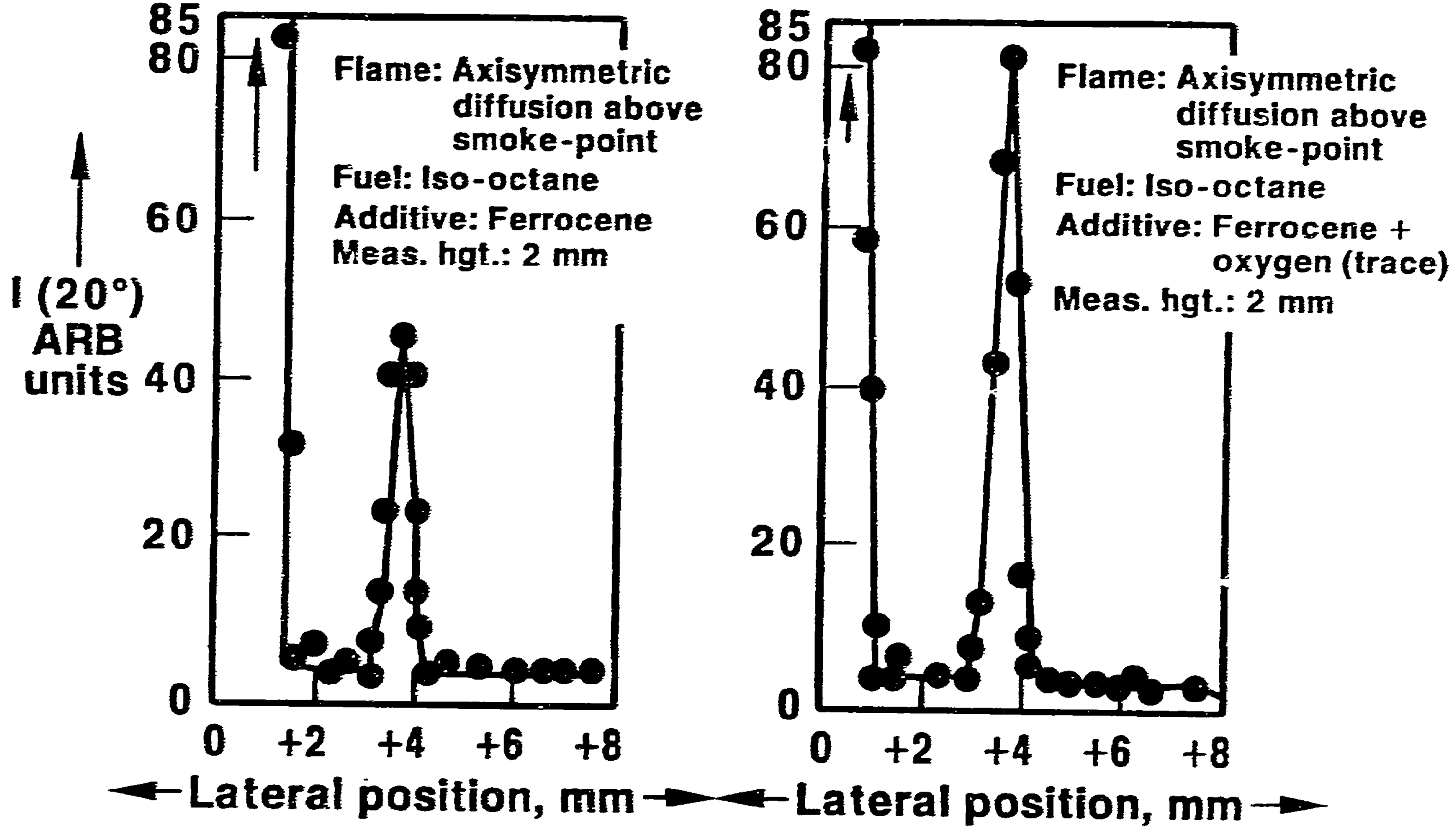

(a)

(b)

RA2745TX.011

Fig. 2.13

that due to molecular Rayleigh scattering) and the insensitivity (unreported data) of the 20/160° scattering ratio to O_2 addition, it appears indeed that the data in Fig. 2.13 indicate an increase in the number density of solid particles with said addition. Although the data in Fig. 2.13 are highly suggestive of solid Fe_xO_y formation, further confirmation of this interpretation is desirable. Accordingly, measurements were made in which soot from the ferrocene seeded flame was collected on cooled metal discs placed in the post combustion effluent stream, and then the soot was examined via ESCA for evidence of Fe or Fe_xO_y occlusion within the soot particulates. These data are discussed in a separate section below.

2.4 Quartz Probe Species Sampling

In order to determine the effect, if any, which ferrocene has on the gas-phase products of iso-octane/air combustion, the latter species concentrations were measured using a small quartz probe for species extraction, a steel cylinder for sample collection, and a gas chromatograph for concentration analysis.

The probe which was used is shown in Fig. 2.14. It is uncooled, has a 0.17 mm diam. aperture, and is similar to one used earlier by Kaiser et al. (Ref. 2.12). The design of the probe is such as to minimize flame perturbations and to effect a rapid reduction in static pressure and thereby quench species-altering chemical reactions occurring within the probe or transfer line. Using a mechanical vacuum pump and an appropriate control (throttle) valve, the pressure at the probe tip was typically 1-3 Torr under conditions of sampling, i.e., with the probe positioned within the luminous zone of the flame. Pressures higher than the range given above showed evidence of perturbations of the true flame species spectrum, i.e., additional species not present at 1-3 Torr were evident.

In Figs. 2.15 and 2.16 evidence is given of the extent to which the quartz probe perturbed the very small iso-octane/air diffusion flame. Clearly perturbations are present, and become progressively more evident as the probe is inserted nearer the burner lip. These

Fig. 2.14

RA2745TX.025

QUARTZ SAMPLING PROBE

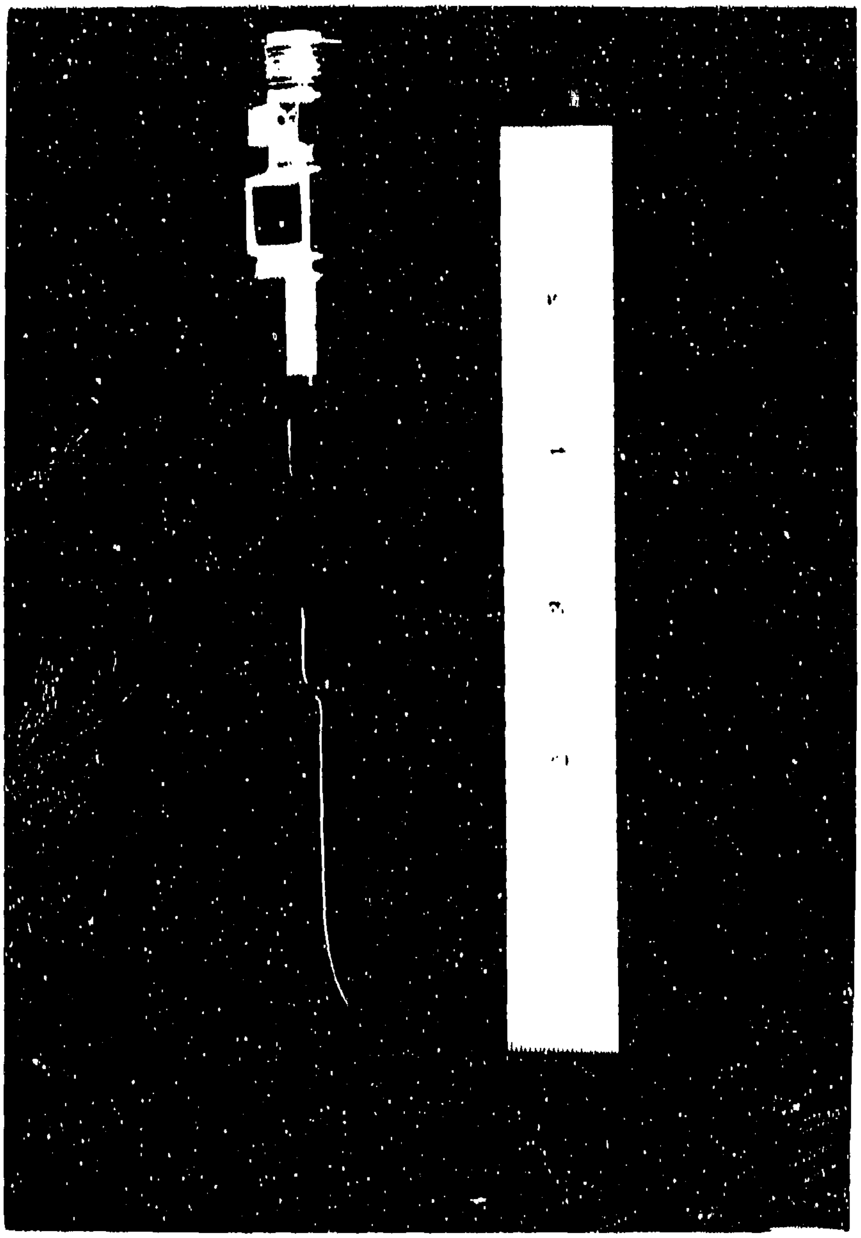

Fig. 2.15

FLAME WITH AND WITHOUT SAMPLING
AT Z = 15 MM

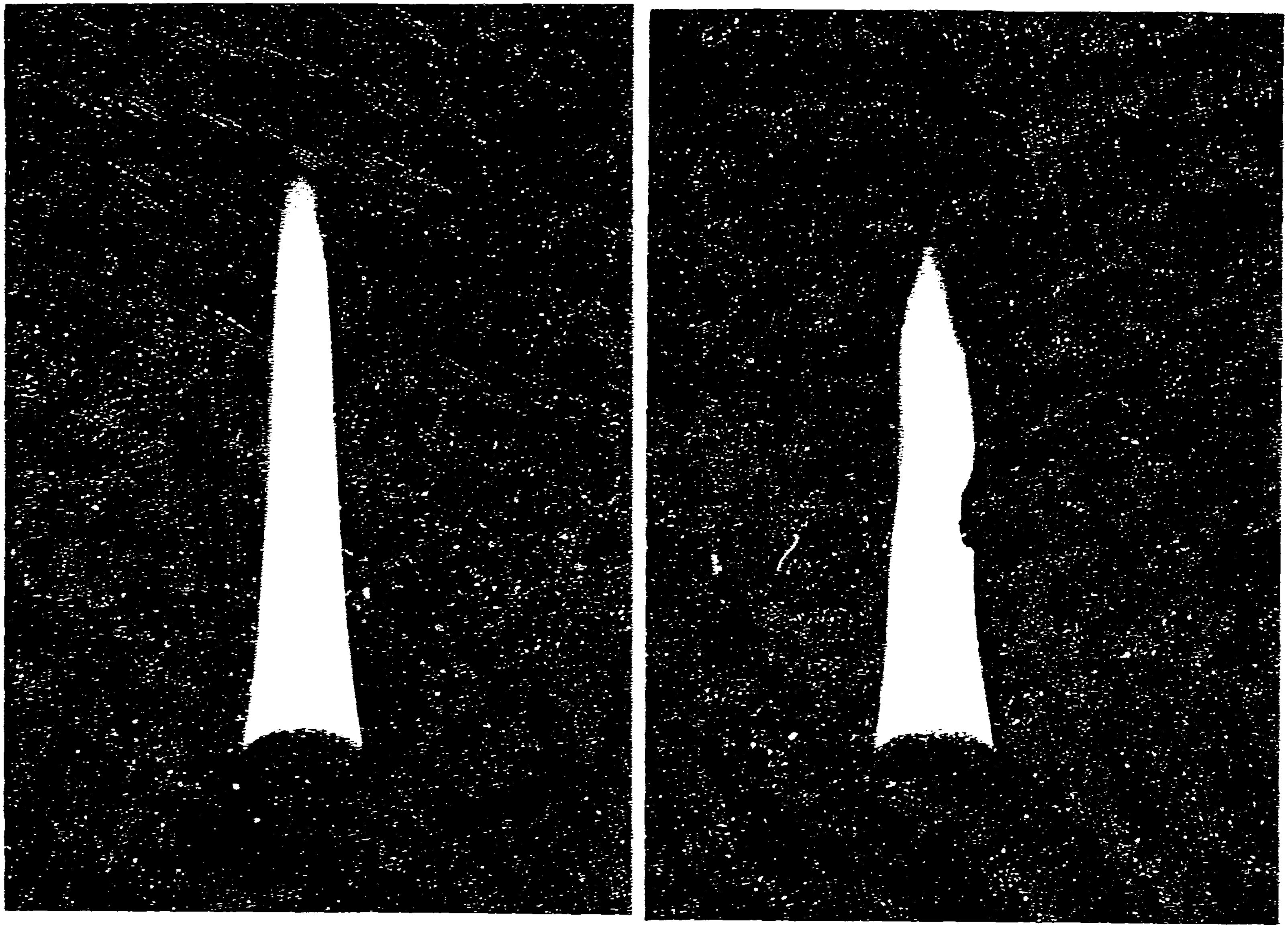

FLAME SAMPLING AT DIFFERENT HEIGHTS

z = 12 mm

z = 9 mm

z = 6 mm

RA2745TX.023

visible distortions are most likely due to cooling of the flame by the probe, and are not, for example, due to excess suction of the emerging combustion gases. This was tested by moving the probe in and out of the flame, and observing the flame distortion with the mechanical vacuum pump in Fig. 2.17 alternately valved "in" and "out". The appearance of the flame with the probe at its center was the same in both cases; hence, the assumption of flame cooling by the probe is probably correct. In other circumstances, the distortions would be considered serious and limiting; however, since in this work interest is limited to parameter measurement (comparison) with and without ferrocene, the distortions do not invalidate the results. More specifically, although the probe may, and probably does, affect absolute species concentrations, relative concentrations with and without ferrocene are unaffected.

The gas handling system used to collect samples extracted by the probe is shown in Fig. 2.17. With it, species were collected in a steel sample bottle at room temperature, or collected at liquid nitrogen temperature in a u-tube attached to the control valve. The control valve was used to set the probe tip sampling pressure which was measured with the capacitance manometer. The steel bottle was used successfully to collect gas-phase species up to about C_{10}. The role of the u-tube was to trap condensible, higher molecular weight species such as the pcah; however, this was not successful since the probe became plugged before a condensate of sufficient quantity could be collected. Plugging was not a problem for gas-phase species collection since probe insertion times, relative to those for condensate collection, were very short. In summary, the data reported here are for non-condensible species only. The latter, after being allowed to fill the sample bottle for 1 min or so, were taken then to a separate gas chromatographic facility for analysis.

Two different flames were sampled in this work. One was fueled by prevaporized (125°C) iso-octane mixed with air, while the other differed from the first in that it had a

Fig. 2.17

RA2745TX.001

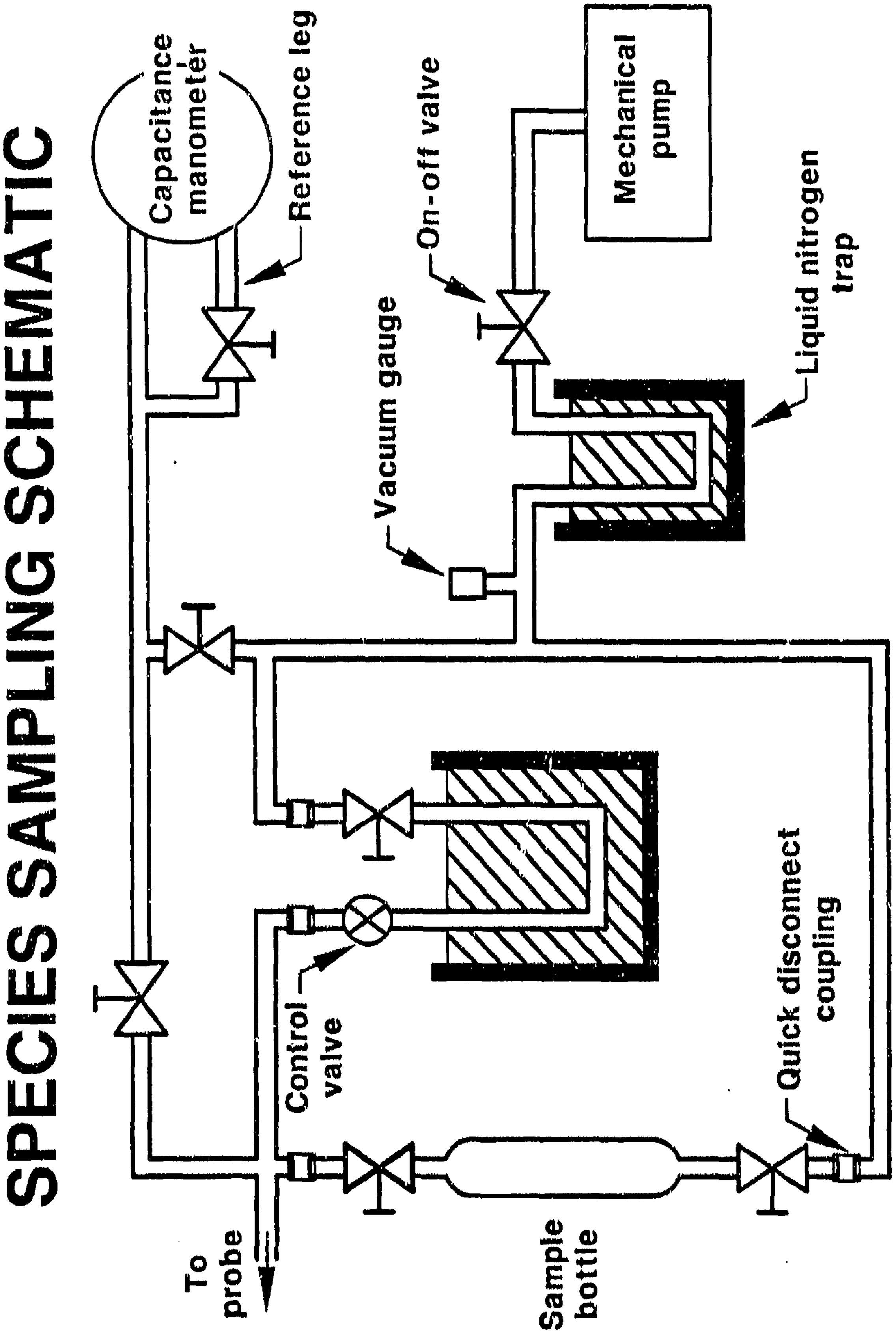

0.3% (by weight) ferrocene additive present in the starting liquid fuel. The burner tube, air plenum honeycomb face and quartz probe are shown in Fig. 2.18. Pure iso-octane or one of several different iso-octane/ferrocene mixtures is selected with the rotary switch in Fig. 2.17. The positive displacement pump delivers about 200 microliters/min of liquid to the vaporizer. There the liquid impacts a column of heated (125°C), small steel spheres (not shown in Fig. 2.17), vaporizes, and is purged through the burner tube with a small ~ 60 cc/min N_2 flow. The vertical portion of the burner tube is more complex in construction than indicated in Fig. 2.17. A thin cartridge heats the top portion of the burner tube directly through an intermediate slip-fit slotted plug. The cartridge heater and its leads are isolated from the hot fuel vapor and the leads are brought out through a feed-through at the bottom of the burner tube. The chimney has a hole in one of its sides through which the quartz probe is inserted. The probe itself is attached to coupled, programmable translation stages which permits precise x- and z-positioning of the probe tip relative to the burner lip with ± 0.0125 mm precision.

The flame studied in this work operates above its smoke-point without ferrocene present. As such, the soot loading is heavy, which leads to rather rapid plugging of the probe's aperture; under the best conditions, sampling could be done for a period not exceeding 1-2 min. Since soot loading varies with height, the preceding difficulty translates into a finite vertical range over which measurements were possible. That is, species sampling could be done for $z \leq 15$ mm, or for vertical positions up to but not including those of peak pcah and soot concentration. An attempt was made to collect pcah (at liquid nitrogen temperature) at $z = 15$ mm with and without ferrocene, but the permissible sampling period was too short for adequate sample collection.

Despite the limitations outlined above, a reasonably large number of species was detected in the range $0 < z < 15$ mm. Figure 2.19 lists all of the species observed at

PROBE AND FUEL TUBE

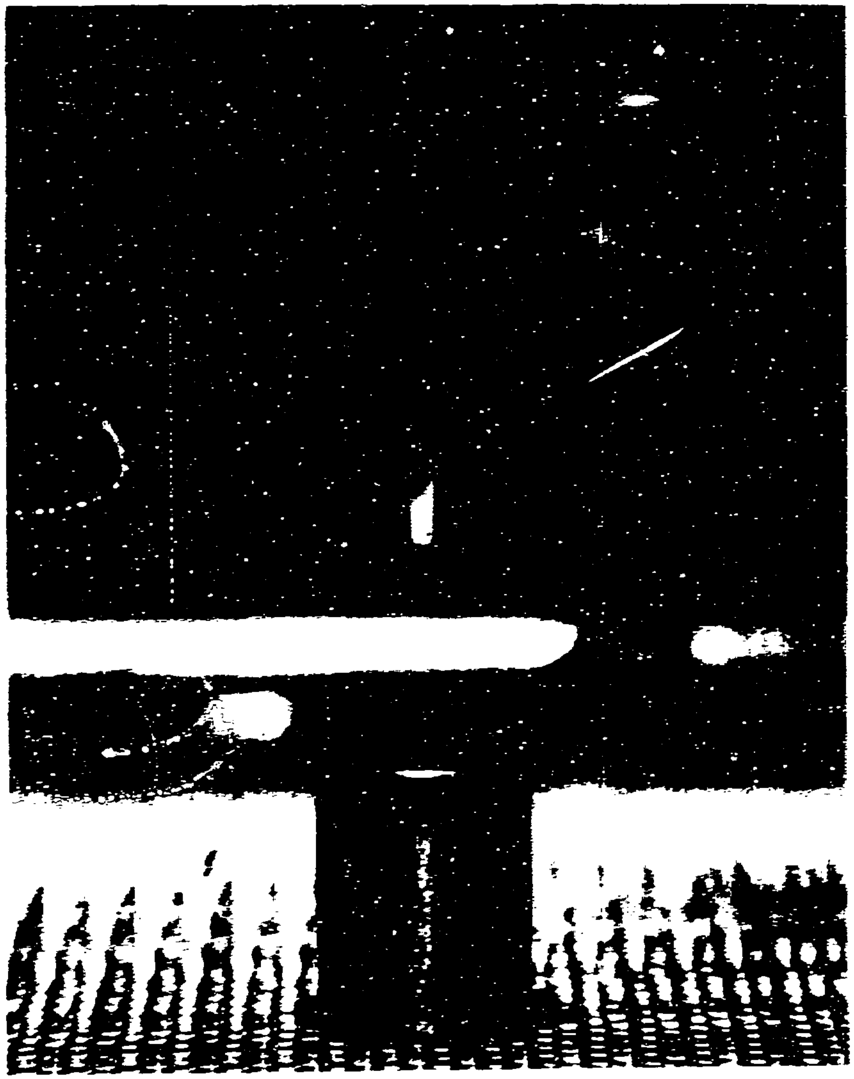

RA2745TX.024

Fig. 2.18

Fig. 2.19

GAS CHROMATOGRAPHIC SPECIES ANALYSIS RESULTS

Species mole fractions at 15 mm height with and without ferrocene. Measurement uncertainties are given in parentheses.

Species	Mole % without ferrocene	Mole % with ferrocene
CH_4	3.12 (18)	3.35 (23)
C_2H_2	2.19 (22)	1.75 (40)
C_2H_4	1.44 (8)	1.43 (8)
C_2H_6	0.14 (2)	0.11 (5)
C_3H_4	0.58 (8)	0.46 (12)
C_3H_6	0.33 (8)	0.35 (12)
C_4H_6	0.09 (3)	0.08 (2)
isobutene	0.14 (5)	0.15 (9)
C_6H_6	0.54 (2)	0.52 (7)
C_7H_8	0.10 (3)	0.13 (5)
phenylacetylene	0.08 (2)	0.06 (4)
styrene	0.11 (3)	0.10 (4)
C_9H_8	0.10 (5)	0.05 (3)
$C_{10}H_8$	0.31 (28)	0.37 (41)
H_2	3.98 (60)	7.60 (219)
CO	4.90 (21)	6.32 (33)
CO_2	7.41 (30)	7.83 (72)

RA2745TX.013

$z = 15$ mm. The numbers in parentheses are the statistical mole % errors multiplied by 100; so that, e.g., 3.12 (18) is 3.12 ± 0.18, etc. The total mole fraction in Fig. 2.18 is 25.56%; the remaining species are presumed to be N_2 and O_2, where the latter (i.e., O_2) was not readily amenable to mole percent measurement with the gas chromatograph. In order to account more carefully for all species, at least for one sample position, the O_2 content of a sample at $z = 9$ mm was analyzed with a calibrated mass spectrometer and found to be present at 2.7 ± 0.5% concentration. When this is added to an estimated 70% N_2 concentration from gas chromatographic analysis, and then added to the concentrations of the remaining species, a 104% concentration results. This is close enough to the correct value of 100% since relative (and not absolute) concentrations with and without ferrocene are of principal interest here.

With the exception of naphthalene ($C_{10}H_8$), as indicated by the large error, all the measured mole fractions were very repeatable. The difficulty with naphthalene may have been its tendency to condense in undesired locations either during collection or during analysis. For this reason, although it is an important pcah, no claim to having successfully measured its concentration is made. Generally, Fig. 2.19 indicates that ferrocene is not very perturbing of the species mole fractions. The possible exceptions are C_2H_2, H_2 and CO. Figures 2.20 through 2.26 give the representative behavior of the more important species concentrations as a function of vertical position. In contrast with the absence of any perturbation of C_6H_6 in Fig. 2.20, ferrocene appears to decrease C_2H_2 systematically in Fig. 2.20 and to increase H_2 dramatically in Fig. 2.23. Although the measurement errors associated with C_2H_2 and H_2 measurement are not small, we believe that the indicated trends are probably correct. If so, a possible conclusion to be drawn from these data is that ferrocene enhances C_2H_2 oxidation. Although an increase in CO was observed only at $z = 15$ mm in Fig. 2.24, the increase is consistent with the foregoing hypothesis. Also in Fig. 2.24 the pyrolysis of the fuel behaves very similarly with and without ferrocene, which

CH_4,C_2H_2 AND C_6H_6 CONCENTRATIONS

With (●,▲,■) and without (○,△,□) ferrocene

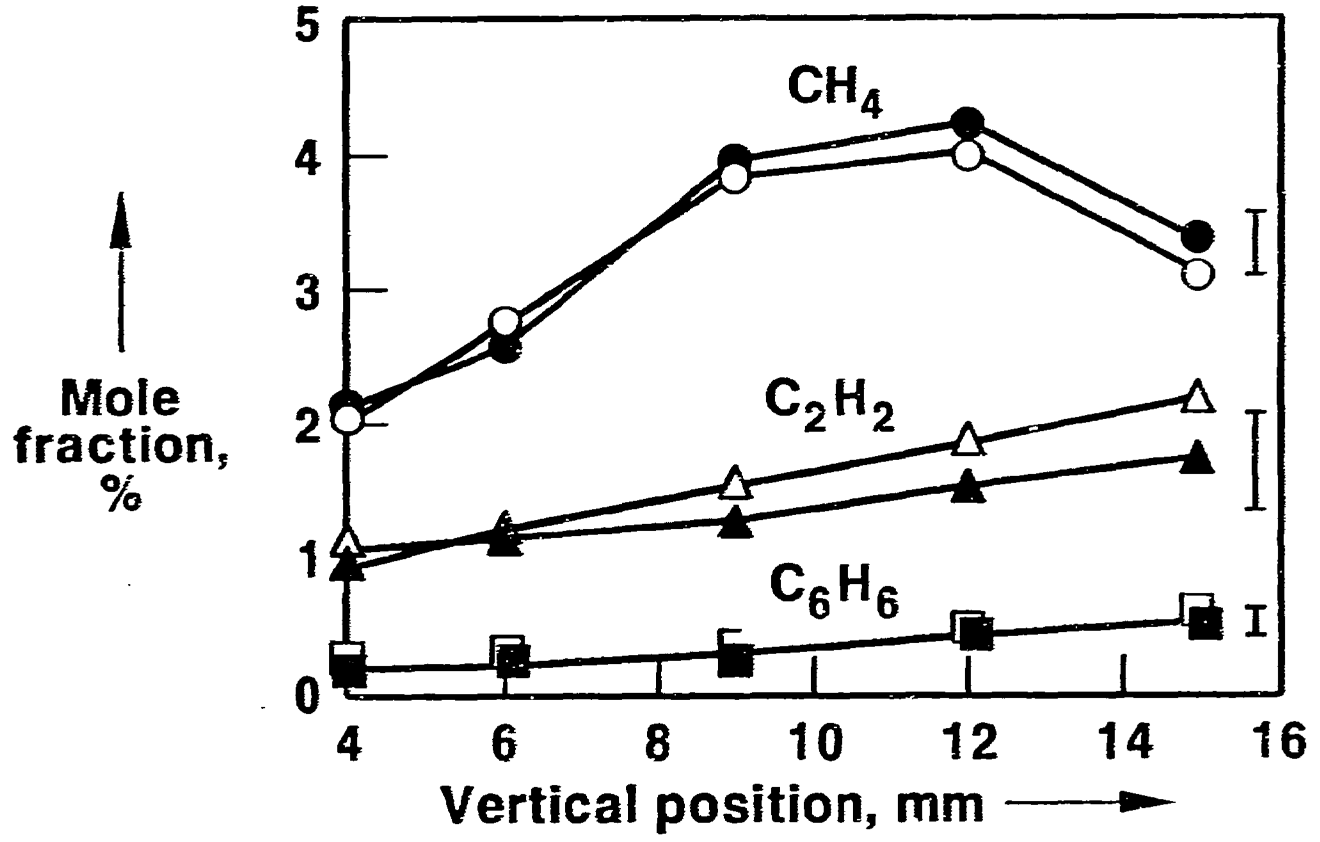

RA2745TX.002

C_2H_4, C_2H_6 CONCENTRATIONS

With (●,▲) and without (○,△) ferrocene

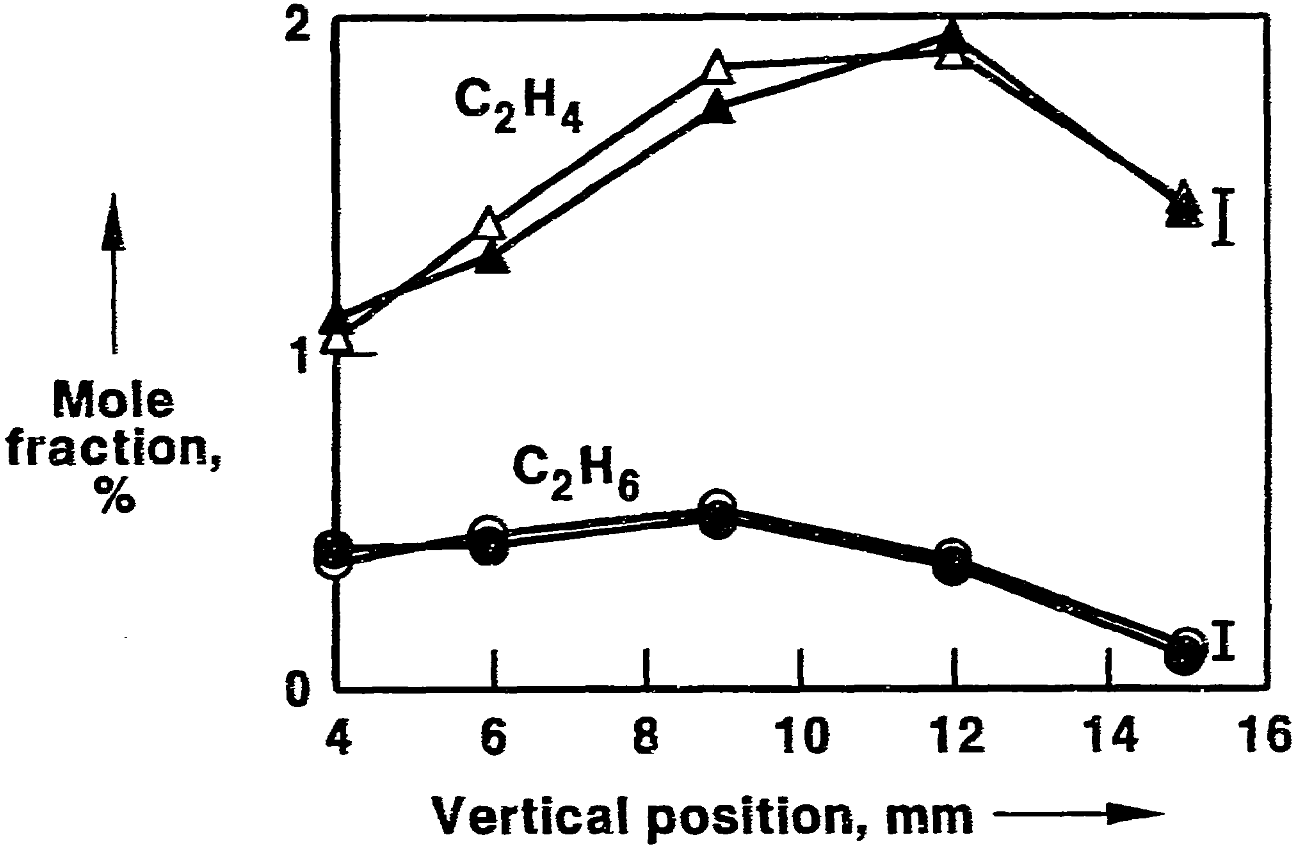

RC2745TX.003

C_4H_8, C_3H_4 CONCENTRATIONS

With (●,▲) and without (○,△) ferrocene

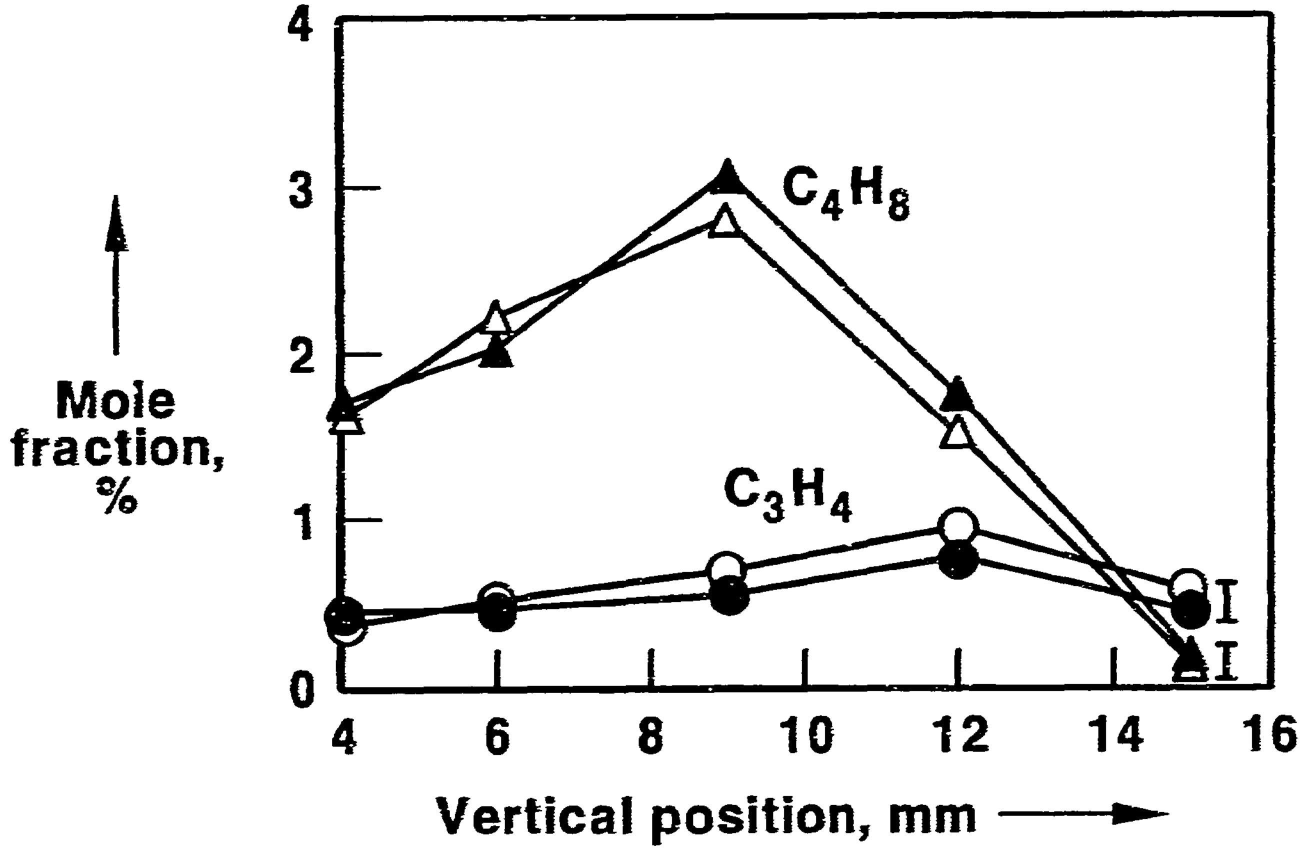

RC2745TX.004

Fig. 2.22

Fig. 2.23

R274531L.003

H_2 CONCENTRATION

With (▼) and without (▽) ferrocene

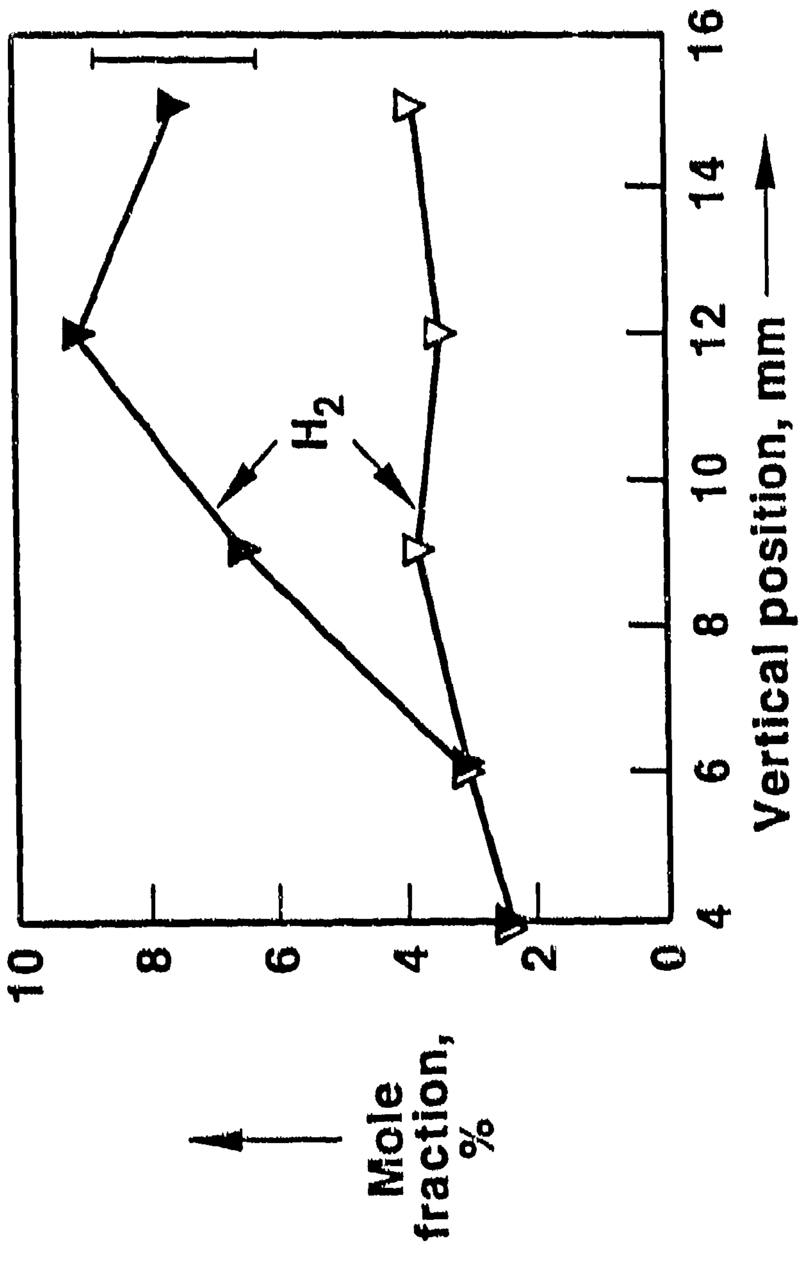

CO$_2$,CO AND C$_8$H$_{18}$ CONCENTRATIONS

With (●,▲,■) and without (○,△,□) ferrocene

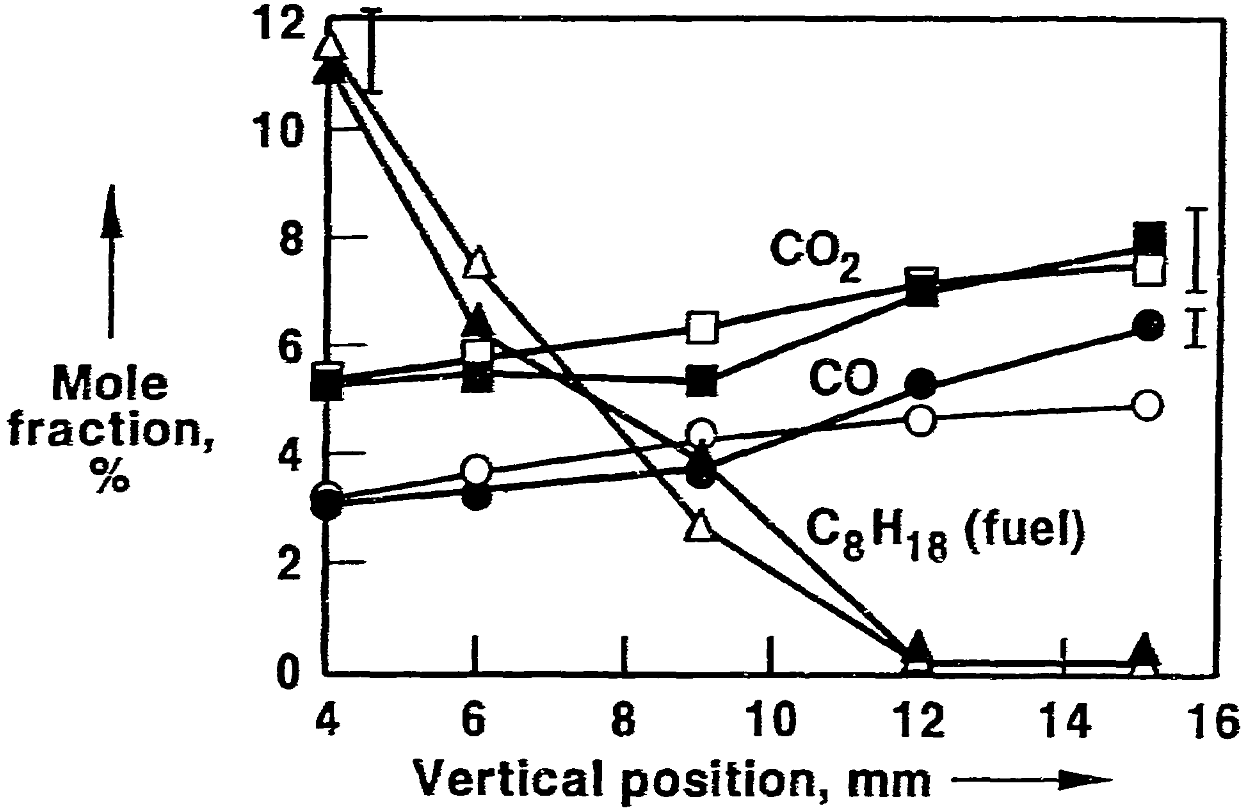

RA2745TX.006

TOTAL O_2 AND C CONCENTRATIONS

With (▲,▼) and without (△,▽) ferrocene

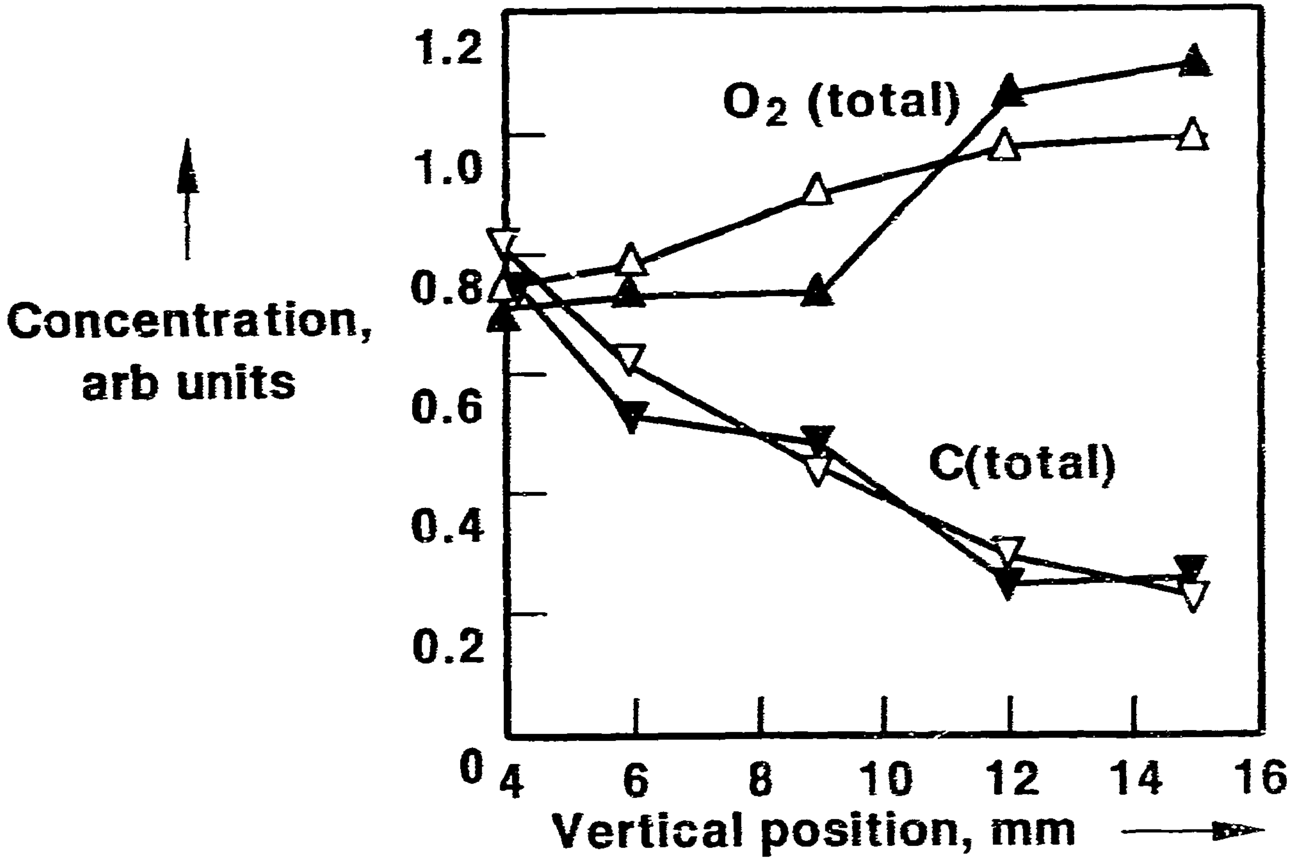

Fig. 2.25

TOTAL O_2 AND H CONCENTRATIONS

With (▲,●) and without (△,○) ferrocene

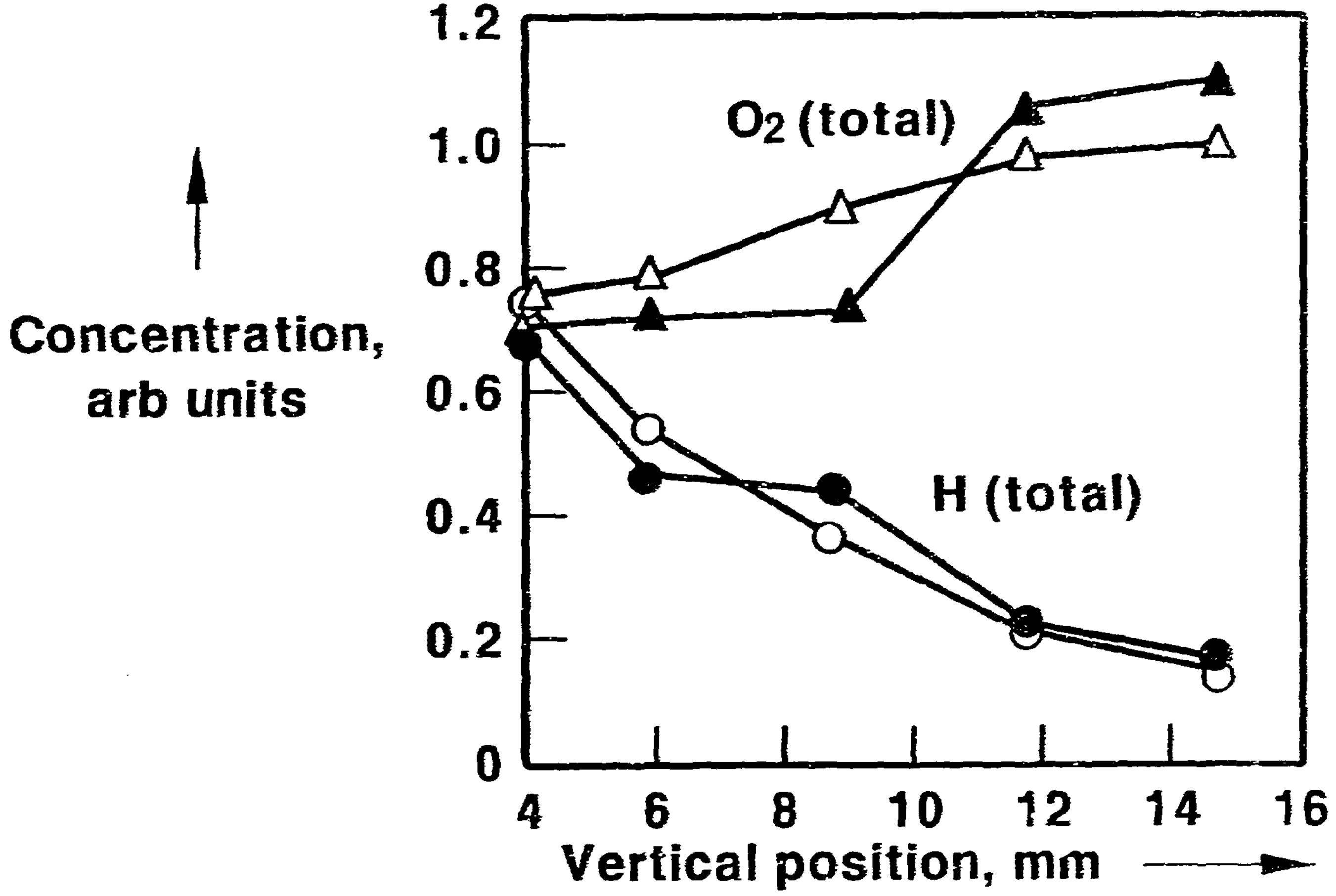

RA2745TX.004

is evidence against any significant increase or decrease of flame temperature due to ferrocene introduction. The total O_2 (or 2O), C and H data in Figs. 2.25 and 2.26 gives evidence that the gross compositions of the unseeded and seeded flames are very similar.

2.5 ESCA Solid Effluent Analysis

In premixed ethylene/air flames seeded with ferrocene, Ritrievi et al. (Ref. 2.13) have presented evidence that the ferrocene combustion product Fe_xO_y is occluded by the soot particulates, and that under favorable conditions the additive species may diffuse to the surface of the particulate and enhance soot oxidation. More specifically, the chemical state of the additive species within the soot and its ability to diffuse to the surface of the particulate determines the extent to which both growth and oxidation are affected.

In view of the above, experiments were carried out in order to look for occlusion in our flame. Since probe plugging prevented our sampling particulates from within the luminous zone, collection was done above the flame tip and well into the post flame effluent stream. There a water-cooled aluminum disk was placed for some tens-of-minutes, and a visible condensate was allowed to form. The sample was then subjected to chemical composition analysis versus depth using ESCA (Electron Scattering for Chemical Analysis). In this technique, the material to be analyzed is illuminated with a beam of soft x-rays. These cause both photo- and Auger-electrons to be emitted from surface layer atoms. Measurements of the kinetic energies of the emitted electrons may be converted to binding energies from which a species identification may be made. The atom fraction of a given element is a function of the area under the signal curve and an appropriate sensitivity factor. Depth profiles are obtained by controlled sputtering away of surface material with energetic argon cations done in sequence with the ESCA procedure described above. The ESCA sample analysis was done for us by Dr. Bruce L. Laube of our laboratory.

As mentioned, the unseeded flame in this experiment operates above its smoke-point. For a 0.3% ferrocene seed, the flame goes over to below smoke-point operation, and a red-orange condensate covers the aluminum disk. The results of the ESCA analysis of this condensate is shown in Fig. 2.27. The results for the surface layer (i.e., zero Å depth) are spurious in that the carbon present results most likely from atmospheric CO_2 contamination. This occurred since no special precautions were made to shield the surface during transfer of the discs to the ESCA laboratory. From the data at 50, 100 and 200 Å in Fig. 2.27, and the chemical shift of the binding energy of the Auger electron, it follows that the condensate is Fe_2O_3. These data provide no direct evidence concerning occlusion since carbon was not detected below the outermost surface layer. In view of this, samples were collected for conditions of very slight ferrocene seeding (smoke plume still visible, 0.01% ferrocene by weight in fuel). In this case, the condensate was principally carbon with, however, detectable quantities of iron present. The chemical state of the additive was elemental iron (Fe), and the results of the depth profile were inverse to that expected for occlusion. The depth profile is shown in Fig. 2.28 where the principal atomic constituent is carbon, and where the iron fraction decreases continuously with sputtering depth. In summary, we found no evidence for occlusion of Fe_xO_y by soot in our diffusion flame. This contrasts with the opposite conclusion reached by Ritrievi et al. (Ref. 2.13) for measurements in a premixed flame.

2.6 Temperature Measurements

Measurements were made to determine the effect, if any, of ferrocene seeding on flame temperature. The temperature measurement technique which was used is based on infrared emission tomography. To implement the technique, algorithms of Fourier transform tomography are applied to deconvolve local soot absorption coefficient and Planck function (temperature) from sets of line-of-sight measurements. The details of this technique and

ESCA ANALYSIS OF FLAME DEPOSITS

Composition of effluent in atomic percent units.
Ferrocene in fue! at 0.3% (wgt). Below smoke-point flame.

Depth, Å	Fe	O	C
0	32.0	53.1	14.8
50	40.4	58.2	1.1
100	43.6	56.4	-
200	43.3	56.7	-

RA2745TX.015

Fig. 2.27

ESCA ANALYSIS OF FLAME DEPOSITS

Composition of effluent in atomic percent units.
Ferrocene in fuel at 0.01% (wgt). Above smoke-point flame.

Depth, Å	C	Fe	O
0	88.3	1.7	10.0
50	96.2	1.6	2.2
100	97.6	1.3	1.1
200	98.6	0.9	0.5
500	99.0	0.8	0.3
1000	99.4	0.5	0.1
1500	99.5	0.5	-
2000	99.7	0.3	-
3000	99.8	0.2	-

RA2745TX.014

Fig. 2.28

one or two applications of it are described in Appendix I of this report. Here, the discussion is limited to a brief summary of pertinent issues not available elsewhere.

With one exception, a photograph of the apparatus which was used to make the temperature measurements is shown in Fig. 2.29. The exception is that the burner which is shown supports an ethylene/air flame, results for which are given in Appendix I, whereas for the ferrocene related work the burner shown in Fig. 2.2 was substituted in its place. The data required to implement the technique include line-of-sight measurements of 1) the flame's emission and 2) the lamp emission superimposed on that of the flame. Moreover, the data are taken for consecutively different radial points in the flame by scanning the burner in a direction transverse to the light-collection axis. The light source for these measurements is shown to the extreme left in Fig. 2.29. It is a tungsten filament lamp whose emission (and filament current) is controlled with a very stable current regulated power supply. The lenses which are shown are symmetrically positioned with respect to the flame. With them the tungsten filament and flame are imaged with 1x magnification onto a vertical slit located behind the fourth lens and in the vicinity of the upper right corner of Fig. 2.29. As such, the set-up is very similar to that for standard sodium-line reversal measurements (Ref. 2.14). Finally, it should be mentioned that the burner in Fig. 2.29 can be moved continuously in a vertical direction and repositioned accurately.

The dependence of temperature on radius was determined, with and without ferrocene, at $z = 10, 15, 20, 25, 30$ and 35 mm. The results at $z = 25$ and 30 mm are given in Figs. 2.30 and 2.31. Given is the dependence of the local emission rate on radius when ferrocene is absent, as well as the dependence of temperature on radius both with and without ferrocene present. In both cases, any change in temperature, if any, with ferrocene addition is very small and within experimental uncertainties of ± 30°K. The same results, i.e. no clear

Fig. 2.29

SOOT ABSORPTION/EMISSION APPARATUS

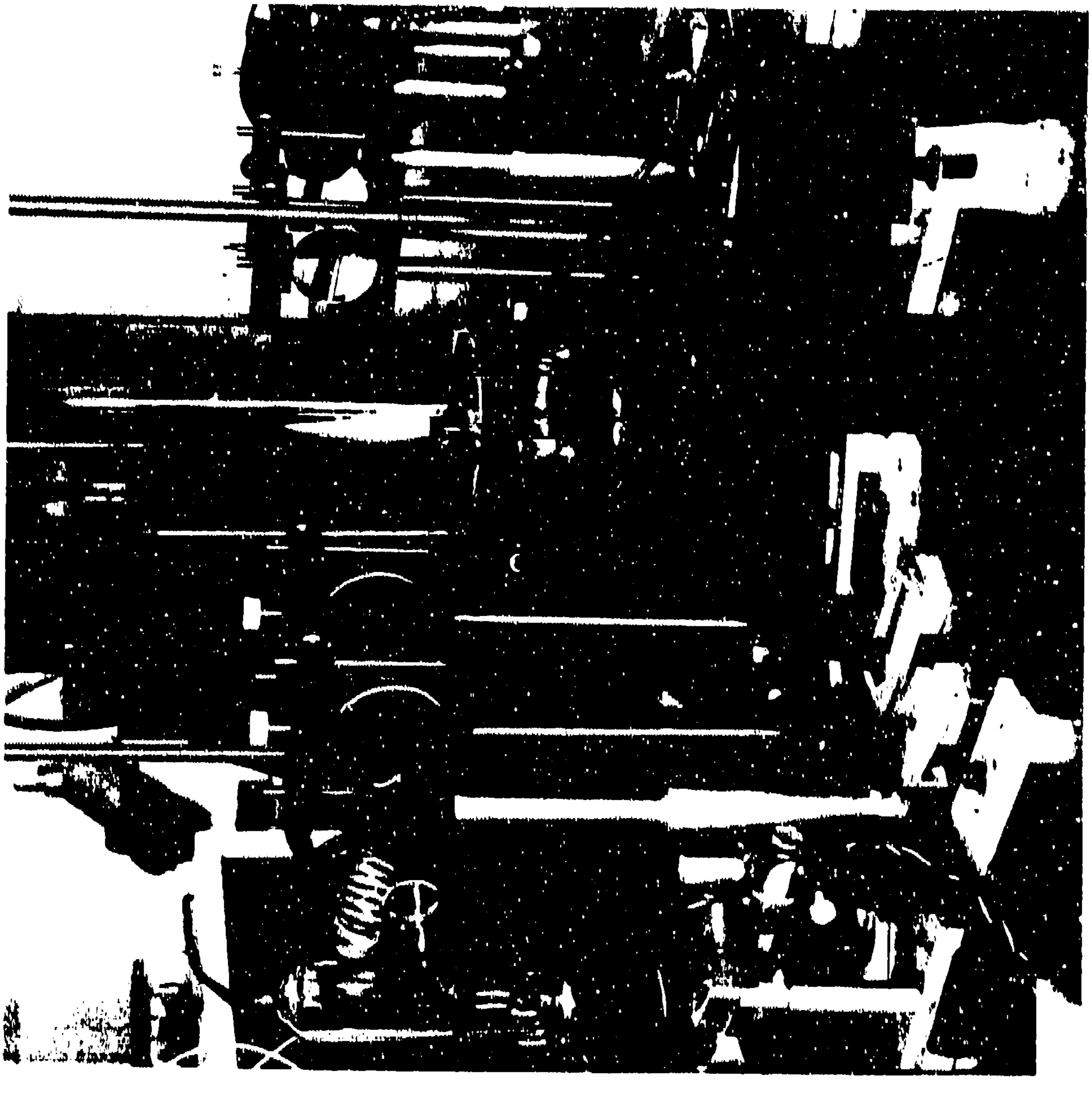

83—1—1—1

88—418

LOCAL TEMPERATURE AND EMISSION VIA TOMOGRAPHIC DECONVOLUTION

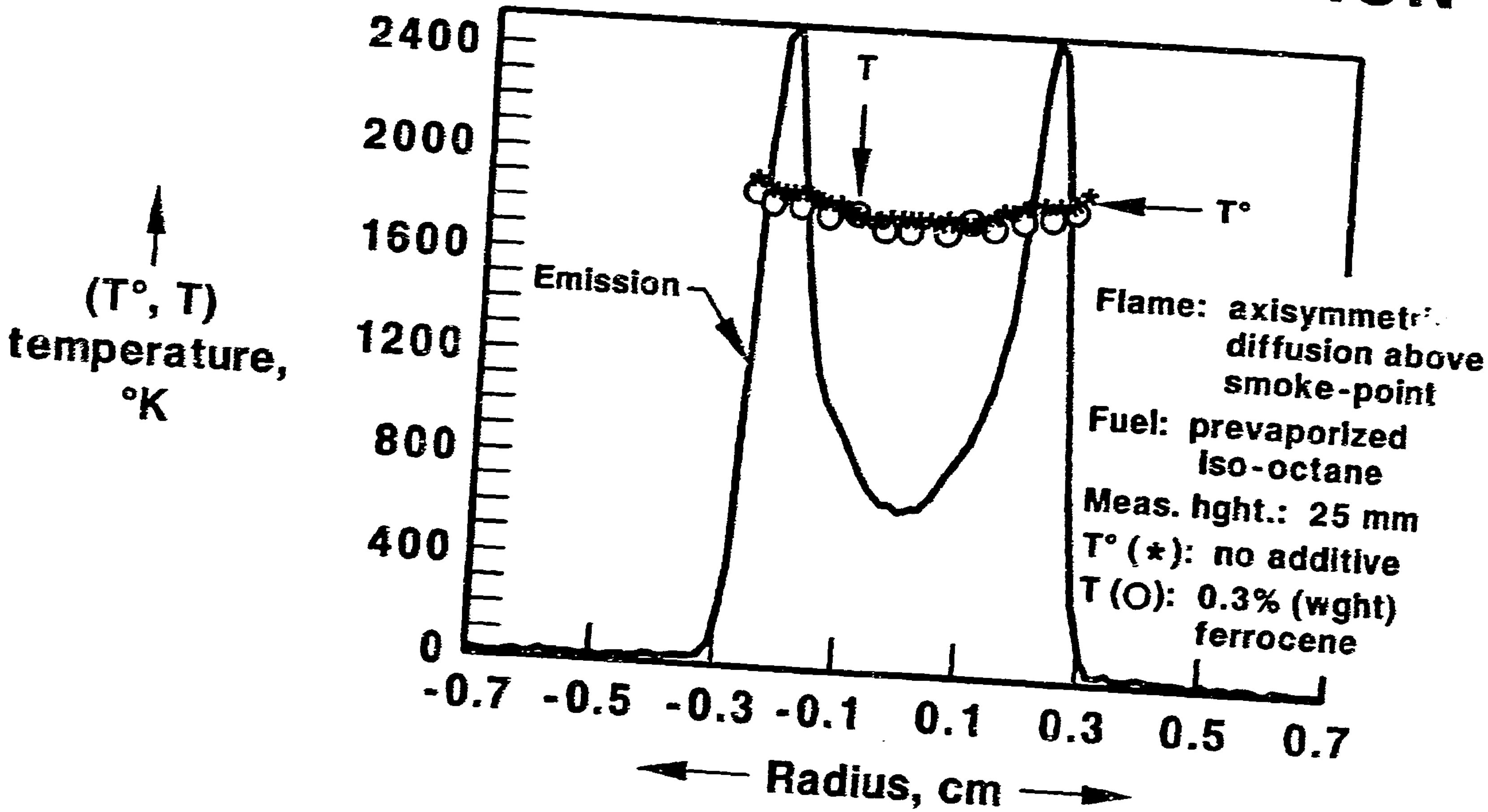

RC2745TX.002

Fig. 2.30

LOCAL TEMPERATURE AND EMISSION VIA TOMOGRAPHIC DECONVOLUTION

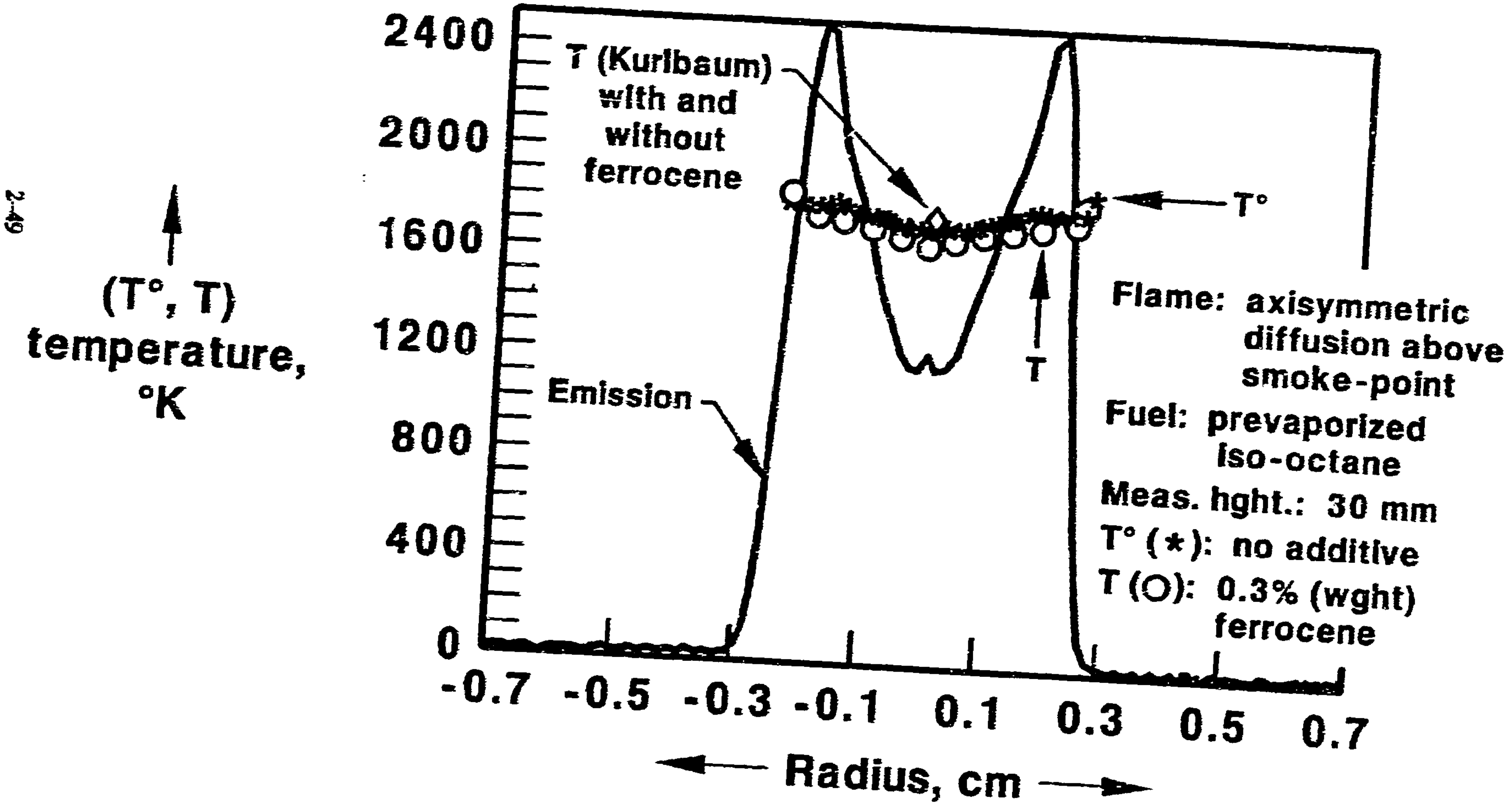

RC2745TX.001

Fig. 2.31

temperature perturbation by ferrocene, were obtained at all other vertical positions in the flame.

In order to verify the accuracy of the tomographic measurements of temperature, a few measurements of temperature were made at selected locations using the Kurlbaum method (Ref. 2.15). For tomography, the slit on which the flame and tungsten lamp filament are imaged is vertical with dimensions of 10^{-2} x 0.16 cm. The long dimension ensures that the depth-of-field as viewed by the detector exceeds the burner tube diameter; this is essential to the path integrated line-of-sight measurements fundamental to the tomographic approach. The 10^{-2} cm ensures good spatial resolution along a radial axis where strong absorption inhomogeneities are present. In order to implement the Kurlbaum method (Ref. 2.15), only minor changes in the Fig.2.29 set-up are required. The vertical slit is replaced with a 25-micron diam. pinhole, and 1 cm diam. obscuration discs (Ref. 2.16) are attached to the faces of the two lenses nearest the burner tube in Fig. 2.29. In this configuration, the depth-of-field is about 2 FA = 150-microns, where F (= 3) is the lens F# and A (= 25 microns) is the pinhole diameter. With theses changes, the temperature on the burner z-axis at 30 mm height was found to be in good agreement with the corresponding result from tomography, and was not affected by ferrocene seeding. The Kurlbaum results are shown as a single data point in Fig. 2.31.

2.7 Discussion

In this section, a few of the more important difficulties and limitations encountered in the work described above are discussed, and comparisons are made between the results of this work and previous ferrocene seeded flame studies.

In order to understand the behavior of ferrocene [$=(C_5H_5)_2Fe$] in relation to soot even better, it would have been useful, perhaps, to seed the iso-octane flame with closely analogous compounds like chromocene [$=(C_5H_5)_2Cr$] or nickelocene [$=(C_5H_5)_2Ni$]. Several attempts to pursue this course were not successful for the following reason. In order to study a metallocene additive in the iso-octane flame, at least three conditions must be satisfied. These are that the additive must 1) be stable against decomposition up to and slightly above the fuel boiling point temperature, 2) be soluble and chemically inactive in the liquid fuel, and 3) have a significant (several Torr or more) and known vapor pressure at the temperature in 1) above. In this connection, for example, we have been unable, despite intense searching, to find reliable vapor pressure data for chromocene in the open literature and, moreover, have observed it to be insoluble in iso-octane. Equally disappointing, although good vapor pressure data for nickelocene exist, its thermodynamic stability is considerably less than that of ferrocene (Ref. 2.17). In addition, although nickelocene initially will dissolve well in iso-octane, it subsequently reacts with even small amounts of air (oxygen) to form an observable precipitate. This latter difficulty may be circumvented, possibly, by purging the fuel of air with an inert gas, but in general extension of the ferrocene studies to other metallocenes is not straightforward. In view of the above, emphasis in this work was on ferrocene alone.

In seeking to understand the details of the behavior of ferrocene in relation to soot suppression, a fundamental issue to resolve is whether the additive intervenes at an early or late combustion stage. For purposes of discussion, early and late stages will be taken to be synonymous with pre- and post particle formation chemistry. In this case, then, the probing of soot precursor species described in Section 2.4 above is that portion of the present study which is relevant to the impact of ferrocene on early stages of combustion. In Section 2.4 above, data are given in Figs. 2.20 and 2.23 which appear to indicate that ferrocene reduces acetylene concentration while simultaneously increasing the molecular hydrogen and carbon monoxide (Fig. 2.24, $z = 15$ mm) mole fractions. The suggestion was made above that this may be evidence that at least one aspect of ferrocene behavior may be to enhance acetylene oxidation. This follows since an important step for acetylene removal in a flame is via C_2H_2

+ O → CO + CH_2 followed by CH_2 + O_2 → CO_2 + H_2 (Refs. 2.18, 2.19, 2.20), with CO and H_2 disappearing through CO + OH → CO_2 + H and H_2 + OH → H_2O + H, respectively (Ref. 2.21). The preceding reaction sequence is, of course, not nearly the entire picture of acetylene oxidation which is described more fully in Refs. 2.18 and 2.19. The above reactions do, however, indicate the source of H_2 and CO release resulting from C_2H_2 oxidations, and serves to clarify the explanation of ferrocene action given above in Section 2.4.

As concerns the effect of ferrocene on post nucleation soot, the results given in Section 2.3 above clearly indicate an interactive process that is both complex and bi-directional with respect to soot enhancement/suppression. Low in the flame operating below its smoke-point, ferrocene enhancement of the volume fraction in Fig. 2.6 is reasonably well established; however, the accuracy of the D and N data in Figs. 2.7 and 2.8 are such that it is not possible to assess the relative importance of the latter two parameters to said enhancement. The data in Table 2.1 are better and somewhat more consistent; there, it is apparent that with the exception of $z = 11$ mm the volume fraction increase is due to an increase in both D and N. In Figs. 2.12 and 2.13, evidence was presented that ferrocene causes soot to appear at an earlier residence time than otherwise would be the case, and that because of the seeding Fe_xO_y solid particles are formed and appear prior to soot inception. It may be that in Table 2.1 the increase in number density with seeding is due to increased nucleation sites for soot provided by the Fe_xO_y. This hypothesis prompted the ESCA measurements discussed above in Section 2.5. As seen there, evidence for such occlusion could not be found, a result which appears to contradict the work of others (Ref. 2.13). Higher in the flame at and near its terminus, both flames (above and below smoke-point) exhibit a soot decrease with ferrocene addition which is brought about by a reduction in both size and number density. The data for the flames near their termini are much cleaner than corresponding data taken much nearer the burner lip. Near the terminus, the size decrease with ferrocene present may be due to enhanced burnout (oxidation) of the soot via a process like, $M_xO_y + C_{solid} \rightarrow CO + M_xO_{y-1}$ (M = metal atom), where incorporation of the metal oxide by the soot would clearly enhance catalytic activity. The observed reduction in number density of soot may be due then to burnout induced size reduction to diameters below the lower limit of sensitivity of the 20/160° angular dissymmetry scattering technique used in this study. Unfortunately, this hypothesis cannot be developed further since Fe_xO_y occlusion by soot could not be confirmed in this work.

The ferrocene work described in this report was preceded by experiments done by others in diffusion (Ref. 2.22) and premixed (Refs. 2.13 and 2.23) flames, in a complex flow swirl-stabilized combustor (Ref. 2.24), and finally in gas turbine engines (Ref. 2.8).

In earlier diffusion flame studies (Ref. 2.22), n-heptane fuel with dissolved ferrocene was atomized by driving nitrogen gas through an atomizer situated at the base of a vertical pyrex tube. The gas drives the fuel-additive fog up toward the top of the tube where it combines with the outside air and burns as a cone-shaped sooting flame. Combustion products were drawn from the flame with a quartz tube, and several wet chemical and chromatographic techniques were used to assess the impact of ferrocene on soot and its precursor species. These techniques demonstrated a reduction of bulk soot by ferrocene as well as a nearly corresponding decrease in pcah (individual species not differentiated). In order to determine the effect of ferrocene on acetylene, the acetylene formed in the flame was precipitated as copper acetylate, and its quantity determined. It was shown in this way that the addition of ferrocene to the fuel did not affect the formation of acetylene. Finally, having shown also that metals and metal oxides do not accelerate the combustion of soot, the authors of Ref. 2.22 concluded that ferrocene action begins after the formation of acetylene but before the formation of soot particles. Clearly there are significant differences between the work reported here and that reported in Ref. 2.22.

A very systematic study of the effect of ferrocene on soot and soot precursors formed in a premixed $C_2H_4/O_2/N_2$ flame has been carried out recently (Refs. 2.13 and 2.23). In it, soot size, number density and volume fraction were determined via a combination of light scattering and extinction for seeded and unseeded flames. The profile of stable hydrocarbon species was determined by gas chromatographic analysis of quartz probe sampled flame gases. Particulates were collected from the flame using a stainless steel water-cooled probe with nitrogen dilution at the probe tip. The spatial distribution of the elements iron and carbon in the particulates was determined via Auger spectroscopy, and the chemical state of the iron via Mossbauer spectroscopy. The key results of this systematic and important experimental study are as follows. Ferrocene was observed to only enhance soot by factors of 13.5 to 1.2 over the range of flame C/O ratios studied, with progressively less enhancement evident for progressively richer flames. The enhancement appears to be due to an increase in both size and number density, with the latter increases being most evident at long and short residence times, respectively. The observed occlusion of iron in soot was consistent with a modelling prediction that Fe_xO_y particles would form in advance of soot formation. This prediction was not verified in Ref. 2.13, but perhaps very importantly this latter prediction is directly supported by evidence presented in this report in Figs. 2.12 and 2.13 and the accompany discussion. For C_1 to C_4 hydrocarbons, the authors of Ref. 2.13 state that none of these were affected appreciably by the presence of iron in the flame. In particular, the acetylene and hydrogen changes induced by ferrocene and shown in Figs. 2.20 and 2.23 above were not observed. For pcah, the results were not as consistent. Some increase with seeding was seen for heavier pcah with more numerous rings like fluoranthene and pyrene. The authors suggest that this result may indicate ferrocene's effectiveness in not only enhancing soot, but augmenting pcah growth rate as well. Unfortunately, in the work reported here good pcah measurements could not be made, so their is no meaningful basis for comparison with the Ref. 2.23 pcah results. It may be that the results described in Refs.

2.13 and 2.23 could be relevant to this work since the chemical state of the additive within the soot and its ability to diffuse near to the particulate's surface determines its relative potential for promoting growth or oxidation. The difficulty is as stated earlier, that Fe_xO_y occlusion by soot could not be verified in this research.

Ferrocene measurements have been made in a turbulent, recirculating model laboratory combustor (Ref. 2.24). A laser-based intensity ratio scattering technique was implemented for the purpose of making size and number density measurements of particulates in a 800 to 3800 Å range of diameter. In this way the spatial distribution of soot was mapped, and the effects of fuel structure, loading and additive (ferrocene) presence were examined. Measurements were also made of the effect of ferrocene on smoke number. For iso-octane/toluene and iso-octane/1-methylnaphthalene fuel blends, the additive was effective in raising the smoke-point in both cases, which indicates that the tendency to soot was reduced. Without further clarification, the additive's effectiveness is stated to depend on the fuel type. In the spatial mapping, the soot number density either increased or decreased in the presence of ferrocene depending on the measurement location in the downstream zone of the dilute swirl combustor. This work served to call attention to the complex impact of ferrocene on soot in a model combustor (fuel type and equivalence ratio dependence, e.g.), but gave no further results of fundamental interest.

Measurements have been made of the effect of ferrocene on U. S. Navy gas turbine emissions (Ref. 2.8). Specifically, the additive's impact on hydrocarbon, particulate and smoke emissions was evaluated. The particulate emissions were extracted isokinetically at the engine exhaust plane and subjected, by standard procedures, to both total mass and size distribution analysis. As concerns the total mass emissions, the results depended on the particular engine type tested, and for a given engine whether it operated at idle, normal rated or full military power. For the most part mass emissions were reduced by up to 50%, but for at least one engine at military power an increase was observed. The additive's effect on size was very complex; in some cases there was a reduction across all aerosol diameters, while in other cases there were fewer small and more large particulates. With respect to number density, with one exception ferrocene acted as a suppressant. Hydrocarbon emissions were assessed by extracting them with appropriate probes and then subjecting the samples to gas chromatographic analysis. The most dramatic change observed with ferrocene addition was an increase in ketones and aldehydes and a decrease in acetylene and alkenes. Individual species were not isolated, and the percent changes were poorly quantified. The significance of this work as a whole is that it brought attention to the potential significance of ferrocene as a suppressant of undesirable emissions from practical combustion devices.

2.8 Conclusions

The principal conclusions of this work are briefly as follows: 1) Ferrocene, provided that it is introduced in sufficient quantity, is a very effective suppressant of soot formed in laminar hydrocarbon/air diffusion flames. This is most clearly manifested in its ability to raise the smoke-point of a flame. 2) The time of first appearance of soot is shortened by ferrocene; to our knowledge, this is an entirely new observation. 3) Following its appearance (or nucleation), the particulate's size and number density are perturbed by ferrocene in a somewhat complex manner as a function of residence time; increases and decreases are observed at early and late times, respectively. 4) For the most part, ferrocene does not affect the pre-particle or soot precursor chemistry. A possible exception to this is our as yet marginal evidence that ferrocene accelerates acetylene oxidation. 5) With modest levels of seeding, ferrocene does not alter flame temperature; the negative result obtained in this work has a precision of ± 30°K. 6) Ferrocene accelerates soot burnout at late combustion stages. A possible mechanism for this would be the catalytic action of solid Fe or Fe_xO_y occluded within soot; but our attempts to verify occlusion were negative. 7) Additional, careful and systematic measurements in diffusion flames are required to further understand ferrocene's behavior. With the exception of the important premixed flame work of Ritrievi (Refs. 2.13 and 2.23), sporadic measurements of the type described in Section 2.7 above have not been very helpful.

Section 2.0 References

2.1 Eisch, J. J.: The Chemistry of Organometallic Compounds - The Main Group Elements, Macmillan, New York, p. 145 (1967).

2.2 Isaenko, V. A., S. P. Gubin, and M. Ya. Nikulin: *Solubility of Ferrocene in some Organic Solvents.* Izvestiya Sibirskogo Otdeleniya Akademii Nauk SSSR, Seriya Khimicheskikh Nauk, No. 2, pp. 80–82 (in Russian) (1984).

2.3 Lewis, K. E., and G. P. Smith: *Bond Dissociation Energies in Ferrocene.* J. Am. Chem. Soc. 106, 4650–4651 (1984).

2.4 Jacobs, M. H. G., P. J. van Ekeren, and C. G. de Kruif: *The Vapor Pressure and Enthalpy of Sublimation of Ferrocene.* J. Chem. Thermodynamics 15, 619–623 (1983).

2.5 Frazee, J. D., and R. C. Anderson: *Effect of Ferrocene on Carbon Formation from Acetylene.* Fuel 38, 329–331 (1959).

2.6 Yin, Jung-Chun: *Eliminating Smoking in Combustion of Petroleum Hydrocarbons by Ferrocene and Synthesis of Ferrocene.* Chem. Abstracts 94:124292g (1981).

2.7 Kracklauer, J. J.: *Conditioning Diesel Engines.* Chem. Abstracts 99:73651s (1983).

2.8 Klarman, A. F.: *Evaluation of the Extended Use of Ferrocene for Test Cell Smoke Abatement; Engine and Environmental Test Results.* Naval Air Propulsion Test Center Report No. NAPTC-PE-110, Trenton, New Jersey, October (1977).

2.9 Bonczyk, P. A.: *Investigation of Fuel Additive Effects on Sooting Flames.* Final Technical Report under AFOSR Contract No. F49620-83-C-0113, 31 July (1986).

2.10 Bonczyk, P. A.: *Measurement of Particulate Size by In-Situ Laser-Optical Methods-A Critical Evaluation Applied to Fuel-Pyrolyzed Carbon.* Combust. Flame 35, 191-206 (1979).

2.11 Senftleben, H., and E. Benedict: Uber die Optischen Konstanten und die Strahlungsgesetze der Kohle. Annalen der Physik 54, 65 (1918).

2.12 Kaiser, E. W., W. G. Rothschild, and G. A. Lavoie: *Chemical Species Profiles of Laminar Propane-Air Flames.* Combust Sci. Tech. 41 271-289 (1984).

2.13 Ritrievei, K. E., J. P. Longwell, and A. F. Sarofim: *The Effects of Ferrocene Addition on Soot Particle Inception and Growth in Premixed Ethylene Flames.* Combust. Flame 70, 17-31 (1987).

2.14 Gaydon, A. G., and H. G. Wolfhard: Flames - Their Structure, Radiation and Temperature, 4th Ed., Halsted Press (Wiley), New York, pp. 269-271 (1979).

2.15 Gaydon and Wolfhard, loc. cit., p. 283.

2.16 Eckberth, A. C., and J. W. Davis: *Spatial Resolution Enhancement in Coaxial Light Scattering Geometries.* Appl. Opt. 16, 804-806 (1977).

2.17 Wilkinson, G., P. L. Pauson, and F. A. Cotton: *Bis-cyclopentadienyl Compounds of Nickel and Cobalt.* J. Amer. Chem. Soc. 76, 1970-1974(1954).

2.18 Miller, J. A., R. E. Mitchell, M. D. Smooke, and R. J. Kee: *Toward a Comprehensive Chemical Kinetic Mechanism for the Oxidation of Acetylene - Comparison of Model Predictions with Results from Flame and Shock Tube Experiments.* Nineteenth Symposium

(Internat.) on Combustion, The Combustion Institute, Pittsburgh, PA, pp. 181-196 (1982).

2.19 Warnatz, J., H. Bockhorn, A. Moser, and H. W. Wenz: *Experimental Investigations and Computational Simulation of Acetylene-Oxygen Flames from Near Stoichiometric to Sooting Conditions.* Nineteenth Symposium (Internat.) on Combustion, The Combustion Institute, Pittsburgh, PA, pp. 197-209 (1982).

2.20 van Dooren, J., and P. J. van Tiggelen: *Reaction Mechanisms of Combustion in Low Pressure Acetylene-Oxygen Flames.* Sixteenth Symposium (Internat.) on Combustion, The Combustion Institute, Pittsburgh, PA, pp. 1133-1144 (1976).

2.21 Browne, W. G., R. P. Porter, J. D. Verlin, and A. H. Clark: *A Study of Acetylene-Oxygen Flames.* Twelfth Symposium (Internat.) on Combustion, The Combustion Institute, Pittsburgh, PA, pp. 1035-1047 (1968).

2.22 Spengler, G. and G. Haupt: *Formation of Soot and Polycyclic Aromatic Hydrocarbons in Simple Hydrocarbon-Air Diffusion Flames and its Inhibition by Additives.* Erdoel Kohle, Erdgas, Petrochem. 22, 679-684 (in German) (1969).

2.23 Ritrievi, K. E., *The Effects of Iron on Soot Particle Formation and Growth,* D. Sc. Thesis, Mass. Inst. Technol. (1984).

2.24 Samuelsen, G. S., C.P. Wood, and T. A. Jackson: *Optical Measurements of Soot Size and Number Density in a Complex Flow, Swirl-Stabilized Combustor.* Presented at the 62nd Symposium on Combustion Problems in Turbine Engines, Cesme, Turkey, October (1983).

SECTION 3.0

ALKALI AND ALKALINE-EARTH SEEDED PREMIXED FLAMES

This section summarizes measurements of soot particulate and precursor species in a premixed $C_2H_4/O_2/N_2/Ar$ flame with and without alkali and alkaline-earth salts (LiCl, $CaCl_2 \cdot 2H_2O$, etc.) present as fuel additives. The principal experimental techniques which have been employed include Mie scattering and optical extinction for soot particulate size, number density and volume fraction, and gas chromatographic analysis of quartz probe collected samples for the determination of soot precursor species concentrations. Data are presented which give the effects of the above metallic salts on soot particulates for three well-defined but different ethylene flames. Also presented is the effect of a cesium additive on soot precursor hydrocarbon species at various locations in one of the flames. Temperature is the principal parameter differentiating the three flames, and various methods which were employed to estimate it are discussed as well. Metal species concentrations were not measured directly in this work, but rather, as shown below, they were estimated from analytical expressions known to be reliable in premixed flame measurements. The section concludes with a discussion of results and where appropriate their relation to earlier work of others.

3.1 Background

When alkali or alkaline-earth metals are present as additives in flames, a significant reduction in the soot volume fraction may occur. This has been observed in laboratory-scale diffusion (Refs. 3.1, 3.2, 3.3, 3.4, 3.5 and 3.6) and premixed (Refs. 3.7 and 3.8) flames, as well as in practical combustion media (Refs. 3.9, 3.10 and 3.11).

Feugier (Ref. 3.7) determined the effect of nitrates or chlorides of alkali and alkaline-earth metals on the soot emitted by premixed $C_2H_4/O_2/N_2$ flames operating at atmospheric pressure. Metals were added to the flame by electrically heating solid samples of their respective salts and, then, using a flow of nitrogen to purge the resulting metallic vapors into the flame. In this work only the soot volume fraction was determined by means of an optical method. In this method, the flame luminosity is measured and compared with the intensity received through the same optical system by a calibrated tungsten lamp. It may be shown (Ref. 3.7) that such data, if properly interpreted, yield not only the volume fraction but also the flame's temperature. It should be mentioned parenthetically that related information concerning soot particulate size and number density and the effect of fuel additives thereon are not accessible to the Ref. 3.7 method. Measurements were made at a height in the flame where the temperature was constant, and where growth of the primary soot particulates was complete but agglomeration had not yet set in. Nine different flames were studied and all were very fuel rich, with equivalence ratios ranging from 2.61 to 3.00 and volume fractions from 1.2×10^{-7} to 1.6×10^{-6} cm^{-3}/CM^{-3}. Results obtained for the alkali metals demonstrated that their principal tendency was to promote the formation of soot. Exceptions to this were cesium at low mole fraction and potassium in the heaviest sooting flame; in the latter two cases, soot inhibition was observed. The behavior of the alkaline-earth metals was equally complex, with, e.g., both inhibition and promotion being observed for barium. The inhibiting effect observed for barium was ascribed to a chemical mechanism by which the additive produces hydroxyl radicals and, thereby, enhances soot removal, a hypothesis subsequently shown to be incorrect by Bonczyk (Ref. 3.5).

Haynes, et al. (Ref. 3.8) have made measurements as well of the effect of alkalis and alkaline-earths on soot in premixed flames. The principal difference between this work and Ref. (3.7) is that in the former case the soot particulate size, number density and volume fraction were determined via laser light scattering and extinction methods with and without additives present. In addition, additive behavior in relation to soot was mapped continuously along the entire symmetric z-axis of the flame. As in Ref. 3.7, the additive effects were determined for several $C_2H_4/O_2/N_2$ flames differing principally in their C/O ratio and temperature. Metals were inserted into the flame somewhat differently. Starting with aqueous solutions (10^{-4} to 0.5 molar) of their salts, the solution was then atomized (perhaps pneumatically, but this was not made clear) and mixed with the flow of cold combustion gases to the burner. The principal effect of the alkali metals on soot is to decrease and increase size and number density, respectively, with the degree of perturbation increasing with elapsed residence time in the flame. This led to the conclusion that the alkali metals inhibit the coagulation of soot by enhancing the charging of soot particulates, in that coagulation and agglomeration are resisted by Coulombic repulsion. The smaller particulates thus produced burn out more rapidly in the oxidation zone of the flame, and thereby soot emission is reduced. With respect to the alkaline-earth metals, calcium, strontium and barium were shown capable of removing soot, but only barium had the capability of increasing soot number density. In view of this result, an argument was made for a second chemical mechanism to explain the data, but the nature of this "chemistry" was left unclear save to point out that it differed from the Coulombic argument appropriate to the alkali metals and barium. Some weak attempt was made to relate the "chemistry" to metal-induced OH enhancement, but as pointed out above this has been since discredited (Ref. 3.5).

Prior to the work described in this report, a considerable effort was made at UTRC to understand the behavior of alkali and alkaline-earth metals as fuel additives in laboratory-scale sooting diffusion flames (Refs. 3.4 and 3.6). As concerns the alkali metals, these were introduced into an axisymmetric flame by atomizing dilute alkali chloride solutions into the oxidant flow stream and changes in particulate size, number density and volume fraction were measured from an analysis of Mie scattered cw laser radiation at 45- and 135-degrees. The concentrations of additive atoms in the flame was inferred from the emission intensities of their respective resonance lines. The additive cation density was evaluated analytically, assuming a Saha equilibrium between charged and neutral species, where the required flame temperature was determined via a standard spectral line reversal procedure. Two different propane/oxygen flames diluted with nitrogen were studied, one being 200°K higher in temperature than the other. For the cooler of the two flames, alkali metals with the lowest ionization potentials strongly increased and decreased soot number and size, respectively, while leaving the volume fraction virtually unperturbed. For the hotter flame, the results were different. The size still decreased, but the soot number density as a function of additive molarity first increased to roughly twice its value in the unseeded flame, and then it decreased. This caused the volume fraction to decrease as well, with (60-70) percent of the soot removed at the highest additive seeding level. Since the hotter flame had more metal cations, the latter were judged to be critical to soot suppression. In Ref. 3.4, an argument was presented that the alkali additives affect both the nucleative and agglomerative phases of soot formation. This was based then on the assumption that the cyclopropenium ion, $C_3H_3^+$, is a soot precursor (Ref. 3.12), a view which is currently in serious doubt (Ref. 3.13). Consequently, the Ref. 3.4 work is in retrospect only supportive of alkali intervention at a late combustion stage. Finally, the additive measurements in Ref. 3.4 were made only at one point on the x-axis of the flame. More extensive mapping of a seeded, slightly different diffusion flame was carried out in a measurement described immediately below.

For the alkaline-earths, measurements were carried out at UTRC in a nearly two-dimensional overventilated ethylene/air diffusion flame emanating from a symmetric Wolfhard-Parker burner (Ref. 3.6). Additives were introduced by aspirating aqueous solutions of their respective salts into the oxidant slots of the burner. The effect of the additives on soot size, number density and volume fraction was determined from a comparison of the angular dissymmetry of Mie scattered laser light with and without additives present. Alkaline-earth metals were found to reduce soot size, number density and volume fraction, with the degree of alteration being dependent on both the particular metal selected (e.g., barium or strontium) and the measurement position in the flame. Optical emission measurements were made in order to identify the significant additive derived species present in the flame, and for barium (Ba), for example, these were: Ba, BaO, BaOH, $Ba(OH)_2$, Ba^+ and $BaOH^+$. By making laser absorption and fluorescence measurements on certain of these species, and by making use of known equilibrium relations between them and unseeded flame radicals, it was possible to estimate the concentrations of neutral and charged Ba, strontium (Sr), and calcium (Ca) species. In addition to soot and additive species measurements, temperature was determined via sodium line reversal methods at points throughout the flame. The most significant results of this study of the alkaline-earths in relation to soot suppression are briefly as follows. First, the relative effectiveness of the alkaline-earths is in the order Ba > Sr > Ca. Second, the effectiveness of a given metal is temperature dependent, maximizing in peak temperature zones which, significantly, also contain the largest concentrations of unseeded flame H and OH radical species. Third and finally, it is possible with reasonable certainty to implicate the charged species MOH^+ ($M = Ca$, Sr or Ba) as responsible for soot suppression.

In the work reported here, the earlier alkali and alkaline-earth fuel additive measurements have been extended from diffusion to premixed flames. The metals are added to $C_2H_4/O_2/N_2$ mixtures which burn as a laminar sooting flame at atmospheric pressure. The methodology used to study additive behavior is similar in several respects to that described in Section 2.0 above for the ferrocene experiments. Here, Mie scattering is employed, but optical extinction is coupled to it for the purpose of characterizing soot particulate size, number density and volume fraction with and without additives present. Except for a slightly modified quartz probe, soot precursor species measurements are done as in the case of ferrocene; namely, samples are drawn from the flame with the probe, collected in a bottle at room temperature or in a metal trap at 77°K, and subjected to gas chromatographic analysis to identify species and determine their mole fraction content.

Flame temperature was determined in two different ways. In one case, its adiabatic limit was estimated from a chemical equilibrium analysis. In the other case, it was evaluated from the Wien equation after inserting in it appropriate, measured values for the brightness temperature and absorptivity of the flame. Finally, the metal atom concentrations were estimated from known parameters associated with additive seeding and fuel combustion. Further details of this work are described in full below.

3.2 Burner and Fuel/Additive Feed

The premixed flame burner used in the experiments described here is shown in Fig. 3.1; a quartz shroud and flame stabilization plate have been removed for clarity of presentation and discussion. The chamber through which the combustion gases flow is machined form 75 mm diam. x 67 mm long solid brass rod. The gases mix in the 71 mm diam. x 51 mm long chamber, and enter the flame zone after passing through 357 equally-spaced 1 mm diam. holes partially visible in Fig. 3.1. As seen, these holes occupy almost all of the 75 mm diam. face of the brass rod. In addition, the length of brass through which the holes are bored is 16 mm, so that L/D = 16/1 for the passage of gas where L and D are the hole depth and diameter, respectively. The brass combustion chamber is enclosed by a 13 mm thick sintered bronze ring having an i.d. and o.d. of 75 and 135 mm, respectively. This ring, shown in Fig. 3.1, has a 15-micron porosity, and a 3 mm o.d. copper coil permanently encapsulated in it through which water passes to cool the brass cylinder enclosed by it. Although water cooling was not required in principle for the temperate flames studied here, it was nevertheless prudently used. Nitrogen is passed through the bronze ring to shroud the flame from extraneous room air. Finally, shown in the upper right corner of Fig. 3.1 is the leading portion of the quartz sampling probe used in this work about which more will be mentioned later.

PREMIXED FLAME BURNER

Without shroud and plate

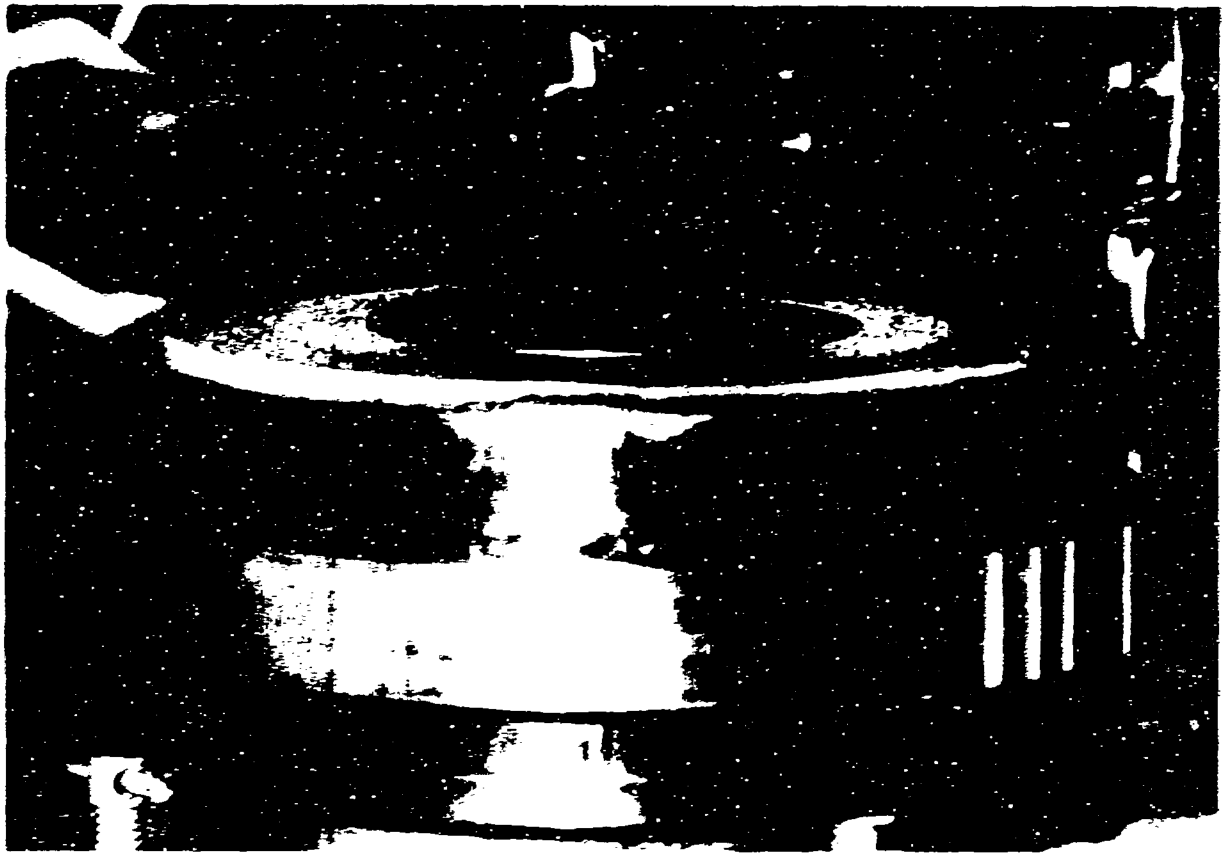

C89-264A-7

89-7-41-1

A more complete view of the burner is given in the photograph shown in Fig. 3.2. The difference there is that the quartz shroud and flame stabilization plate are shown in their assembled positions. The 20 cm diam. stabilization plate is made from 3 mm thick cold roll steel, is uncooled, and is permanently fixed and held parallel to and 30 mm above the burner face. The quartz cylindrical shroud tube in Fig. 3.2 is used to further shield the flame from external disturbances. It has a 143 mm i.d., and its height is such that there is a 3 to 4 mm air gap between the top of the quartz tube and the bottom face of the steel plate. This gap necessarily facilitates the exit of soot and gases which comprise the flame's effluent flow. In addition, it helps to prevent soot from building up on the inside quartz surface which would be detrimental to the light scattering measurements discussed below. Rectangular slots about 7 mm wide are cut into the sides of the quartz tube to facilitate either the movement of the quartz probe in and out of the flame center or unimpeded passage of either one of two laser beams as discussed below.

The use of a plate to stabilize a premixed flame is not a unique concept; prior to this work, it had been employed successfully by others (Refs. 3.14 and 3.15). In both of these works, the reader is left with the impression that a coannular flow of nitrogen and a stabilization plate is all that is required to achieve a "quiet" (motionless) flame suitable for light scattering/extinction measurements. In our experience, this was very painfully not the case. Although it would have been preferable not to use the quartz shroud (soot buildup, scattering of laser light, etc.), its addition to the burner assembly was essential to the success of these experiments.

The premixed flames studied were of the $C_2H_4/O_2/N_2/Ar$ type. As will be discussed, the argon is essential but not sufficient to actuate the atomization of additive salt solutions. It was present at a fixed flow setting (~ 0.75 l/min) with or without seeding. In addition, since metals were introduced as atomized aqueous solutions of their respective salts, the flow to

PREMIXED FLAME BURNER

With shroud and plate

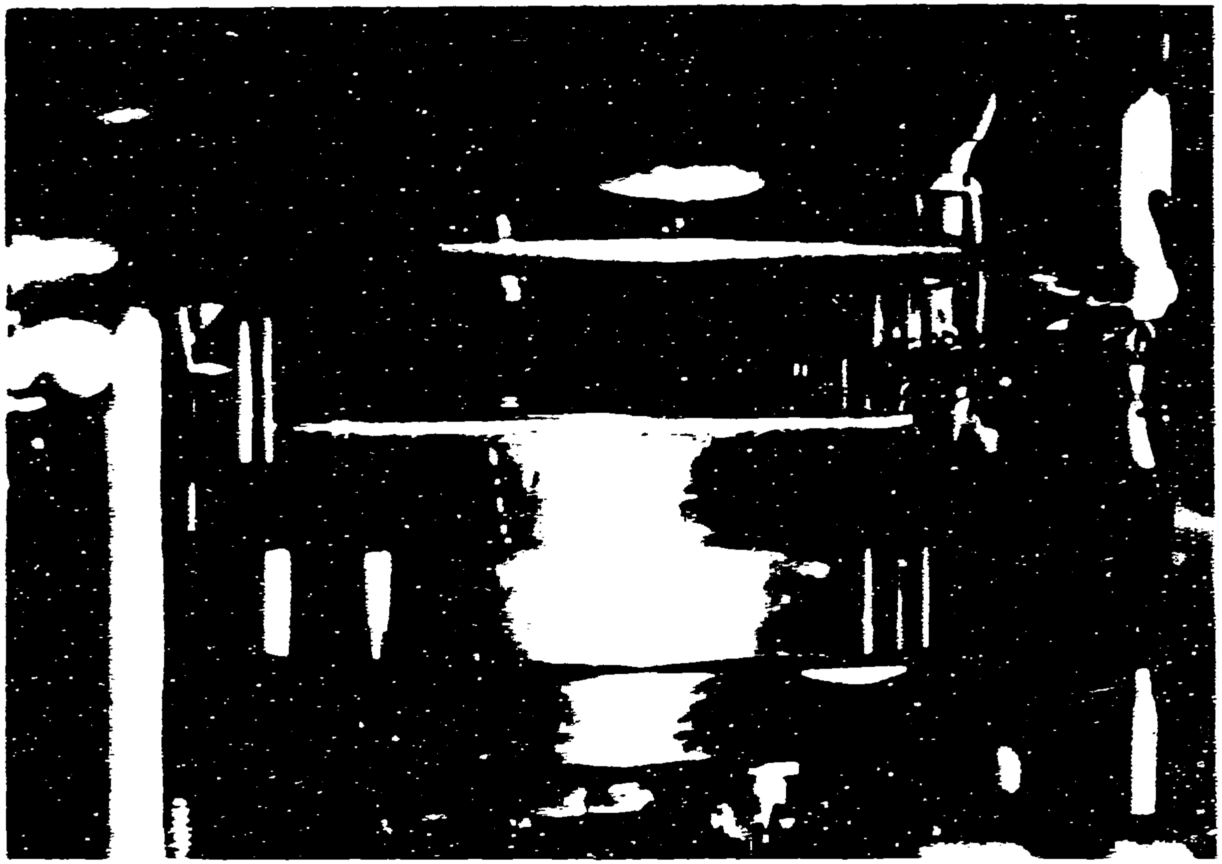

C83—264B—7

89—7—41—2

the burner included a small amount (0.032 cc/min) of water as well. In addition to the N_2 in the flow of combustion gases, a separate source was used to provide a nitrogen flow of roughly 15 l/min through the burner's porous bronze ring. An example of a typical sooting flame is shown in Fig. 3.3. It is referred to in the text below and in Table 3.1 as Flame #ETH2. Conditions appropriate to Fig. 3.3 are C/O = 0.716, and aspiration of the above quantity of pure, distilled water, i.e., no metallic salt dissolved therein. The stoichiometric C/O for this flame type is 0.33, and the onset of soot should begin at about C/O = 0.60 (Ref. 3.16). Finally, for comparison and to visually judge the flame's flatness, side-by-side end-on and elevated views of the flame under very fuel lean conditions are shown in Fig. 3.4. Except for some slight distortion near its edges the flame front is reasonably and, hence, satisfactorily flat.

TABLE 3.1

Principal combustion parameters for the flames studied.

Flame Symbol	**ETH1**	**ETH2**	**ETH3**
C_2H_4 flow, l/min	1.46	1.66	1.85
O_2 flow, l/min	2.04	2.32	2.58
N_2 flow, l/min	6.25	5.78	5.33
Ar flow, l/min	0.75	0.75	0.75
H_2O flow, cc/min	0.032	0.032	0.032
N_2 (shroud), l/min	15.0	15.0	15.0
C/O	0.716	0.716	0.716
Temp.(adiabatic),°K	1920	2070	2195
$O_2/(O_2+N_2)$	0.246	0.286	0.326

PREMIXED $C_2H_4/O_2/N_2$ FLAME

Fuel-rich sooting condition

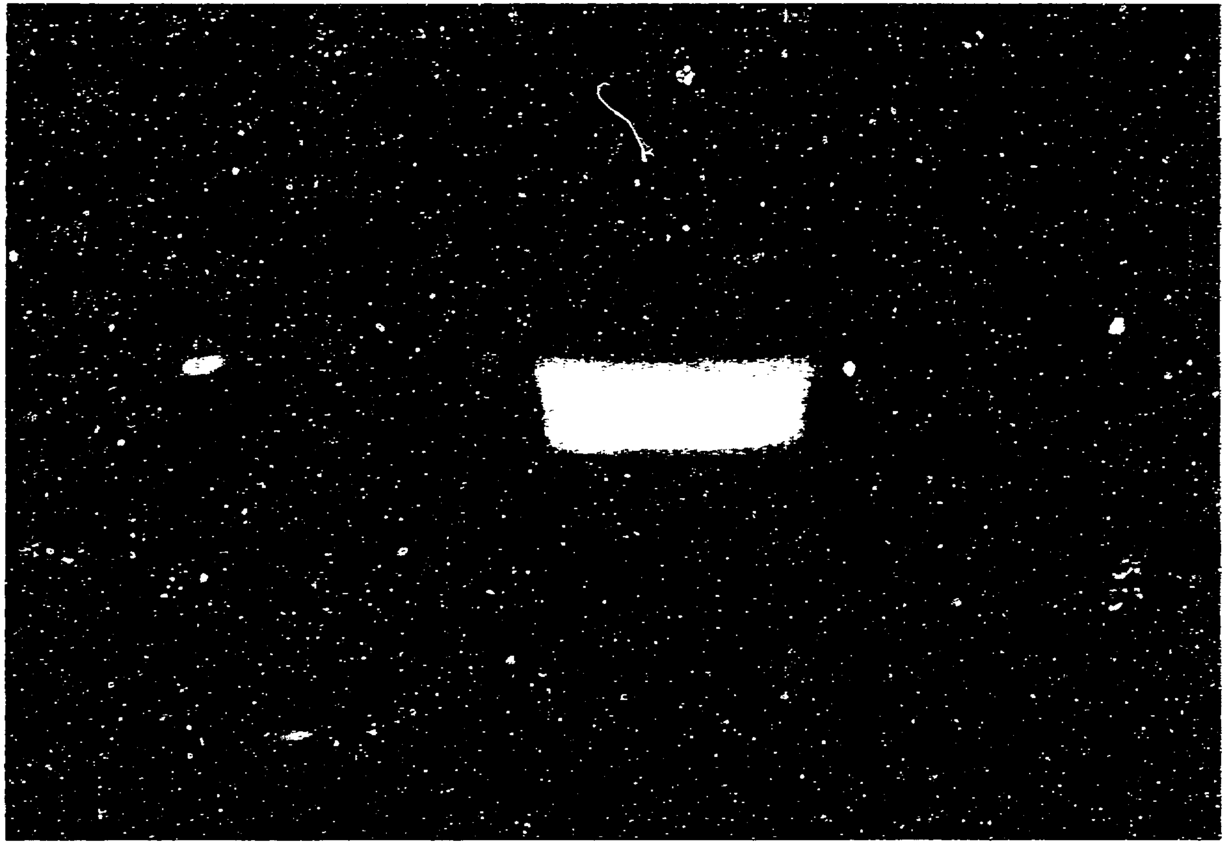

C89—264C—14

89-7—41—3

Fig. 3.3

PREMIXED $C_2H_4/O_2/N_2$ FLAME

Fuel-lean condition

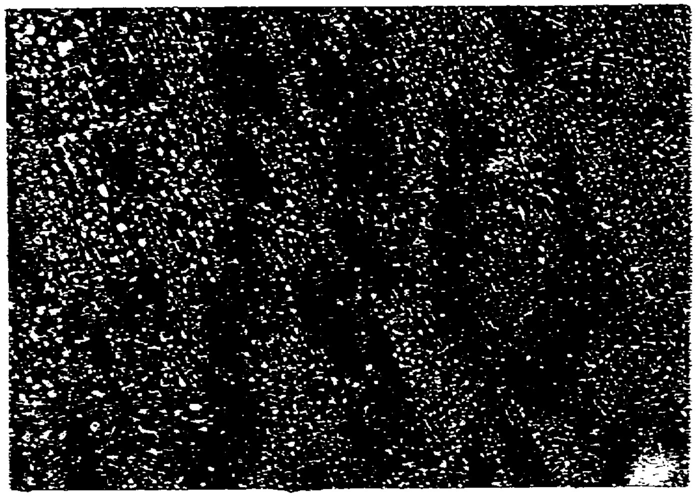

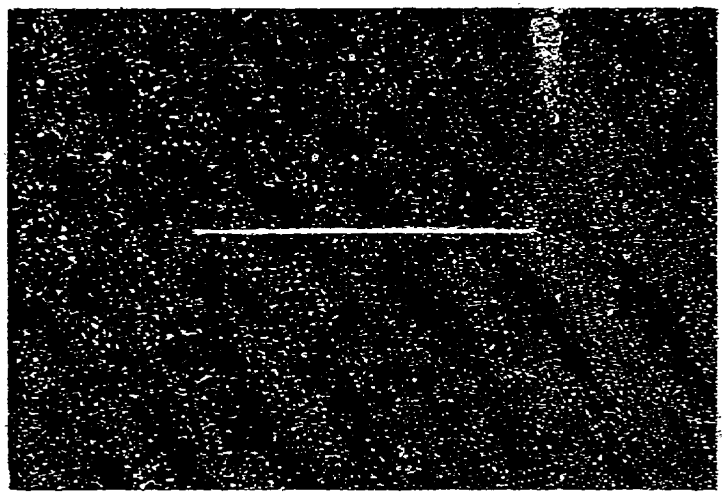

789—2640—4 789—2540—8

89—7—41—5

In previous work with diffusion flames at UTRC (Refs. 3.4 and 3.6), additives were introduced by aspirating an aqueous solution of a metallic salt into the oxidant flow stream using a Varian #99-100236-00 adjustable nebulizer (Refs. 3.17 and 3.18). It normally functions as a component of the Varian Model AA-575 double-beam atomic absorption spectrophotometer; but it may be purchased separately from Varian. The nebulizer operates on a pneumatic principle; the sample solution is driven through a capillary tube by the pressure differential generated by the concentric streaming action of a high velocity gas flow through a nozzle, with the solution flow rate governed by the Poiseuille equation (Ref. 3.19). The nebulizer is made of stainless steel, and includes a corrosion resistant platinum/iridium capillary. There is provision for micrometer control of the sample uptake rate between zero and 10 cc/min. The difficulty with this particular nebulizer are its high gas flow requirements; it requires a (2-3) liters/min carrier gas flow rate for threshold operation, and near 5 liters/min for optimum performance. For a fixed (fuel, oxidant flow rates, stoichiometry, etc.) flame in a conventional spectrophotometer where nebulizer and flame operation are matched, there is no problem; but for other seeded research flames for which, for example, flow rates and stoichiometry are varied, the nebulizer properties can seriously limit the range of flame operation. An example of this occurred in past UTRC $C_2H_4/O_2/N_2$ (Ref. 3.4) and C_2H_4/air (Ref. 3.6) diffusion flame experiments wherein additive insertion into the fuel stream was desired but could not be achieved due to nebulizer properties. In order to avoid this difficulty, a nebulizer of different construction was used for the present premixed flame studies. It is a Model 90-790 non-adjustable cross flow nebulizer purchased from Allied Analytical Systems of Waltham, Mass, and is based on a design described by Novak et al. (Ref. 3.20). It is suitable for use with both aqueous and organic samples, has a polymer body. a teflon capillary tube for sample uptake, a noble alloy needle for sample flow, and a saphire gas flow orifice. The device is designated "cross-flow" since the sample uptake and carrier gas tubes are orthogonal to one another. Like the Varian nebulizer described above, the cross-flow nebulizer operates on a pneumatic principle (Ref. 3.20); however, the principal difference is that the carrier gas flow rate required for sample aspiration is low, < 1 liter/min. Specifically, only 0.75 liters/min of Ar flow will aspirate 2 cc/min of aqueous solution; in contrast the Varian nebulizer requires an actuating flow of about 3.8 liters/min for the preceding aspiration rate (Ref. 3.21). In view of this fact, principally, the cross-flow nebulizer is often more suited to fundamental flame studies. (Similar arguments may be given for its accepted use in providing controlled seeding of inductively coupled plasmas.) There is one caveat for the preceding discussion, however; it is that the Varian nebulizer is a high solids device which will continue to function up to about 0.5 molar salt (in water) solutions. The cross-flow nebulizer is operable only up to and about 0.1-0.2 molar. There are modified versions of the Model 90-790 nebulizer which address this difficulty (Ref. 3.22), but they will not be discussed here. Reference 3.22 gives a complete description of the properties of the 90-790 nebulizer including its aerosol transport efficiency. It is important to note that although the solution uptake rate is 2 cc/min, only 1.6% of it, or 0.032 cc/min, is transported to the flame, with the remainder drained off as waste. (We operate the 90-790 without a pump, and arbitrarily have taken the transport efficiency to be the same as that given for "with pump" operation in Ref. 3.22.) All pneumatically operated nebulizers are roughly similar with respect to low transport efficiency.

A photograph which shows the cross-flow nebulizer, spray chamber, drain tube and reservoir, suction tubing, and cesium salt solution sample is given in Fig. 3.5. The white cylinder almost at the photo center is the polymer body of the nebulizer. The clear polyethylene tubing connected to it at its base carries the argon flow, while the white teflon tube emanating from its side draws the salt solution from the beaker labeled "cesium". For flame data with no additive present, the beaker contains distilled water, or in some cases the teflon tube is withdrawn from the beaker to cease suction. A grey colored stainless steel

BURNER, PROBE AND ADDITIVE ASPIRATOR

69—7—41—7

[illegible]

spray chamber is attached to the polymer body. The blue polyethylene tube entering it carries the premixed cold combustion gases, while the yellow surgical tubing projecting downward from it carries the solution run-off to the pyrex dish located directly behind the beaker. There is a teflon aerosol spoiler (baffle) located in the spray chamber between the drain outlet and the combustion gas inlet; it serves to prevent droplets larger than roughly 5-micron diam. from reaching the flame (Ref. 3.20).

3.3 Light Scattering/Extinction and Particulate Sizing

A schematic diagram of the apparatus used to determine soot particulate size, number density, and volume fraction with and without additives present is shown in Fig. 3.6. The apparatus indicated therein allows for both optical scattering and extinction measurements. The light source used for scattering measurements is the 5320 Å (0.532 µ) 2x Nd:Yag laser. The Pellin-Broca prism, PBP, rotates the 5320 Å output by 90°, and refracts the 10,600 Å (1.06 µ) 1x Nd:Yag residual output into the light trap, T. The half-wave plate, λ/2, rotates the polarization axis of the 5320 Å radiation to a direction normal to the scattering (or Fig. 3.6) plane. The resulting laser light is reflected by the two successive mirrors, M, and focussed at the burner center to about 0.025 cm diam. with the lens, L. The transmitted light is then recollimated by a second lens, L, reflected by a mirror, M, attenuated by a neutral density filter, NDF, passed through a 5320 Å narrow-band optical filter (not shown), and detected by a photomultiplier, PMT, and EG&G/Princeton Applied Research boxcar averager (not shown). The detection arm at 160° records the light scattered by the soot particulates. In it, the two lenses, L, (150 mm focal length, 13 mm diam. effective aperture) and 0.05 cm diam. aperture, A, define a 5×10^{-3} sr light collection solid angle and 1.5 mm long sample length. (The sample diam. is 0.025 cm as defined by the focussed laser beam.) The 160° arm also contains a polarization analyzer, P, aligned with the laser polarization axis, a narrow-band filter, F, centered at 5320 Å, and a photomultiplier, PMT. As above, the

SOOT MEASUREMENT SCHEMATIC

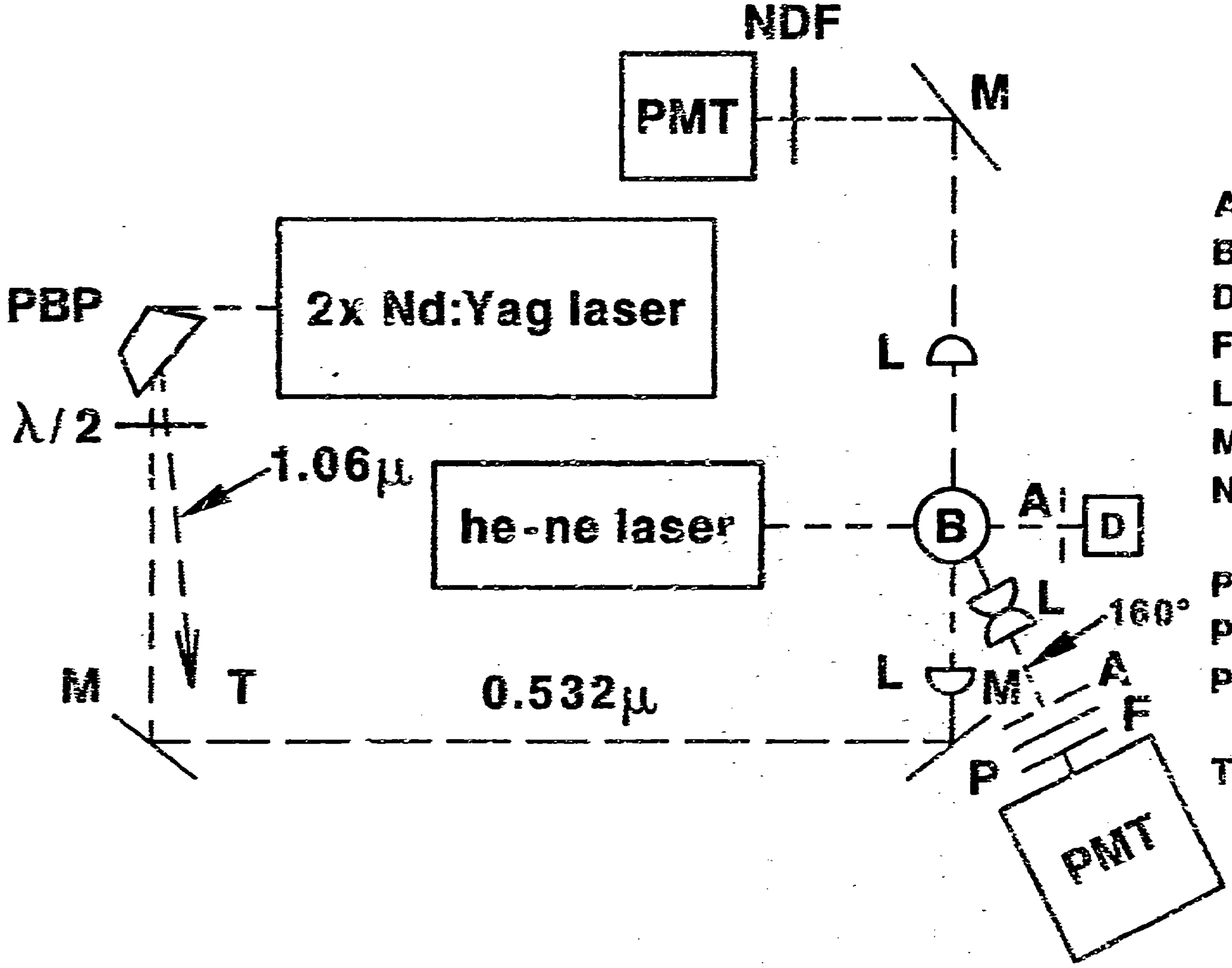

A, aperture
B, burner
D, detector
F, optical filter
L, lens
M, mirror
NDF, neutral density filter
P, polarizer
PBP, prism
PMT, photo-multiplier
T, light trap

RC2745TX.6:4

Fig. 3.6

PMT signal is processed with a boxcar averager (not shown). Finally, a provision for light attenuation measurements at the 6328 Å wavelength of a low power cw helium-neon laser are shown in Fig. 3.6. This red light intensity was passed through a 6328 Å narrow band optical filter and measured with a conventional photodiode, D, with the output displayed on a strip chart graphic recorder. Some of the apparatus components discussed above and physically located nearest to the burner are shown in the Fig. 3.7 photograph. There are one or two noncritical apertures therein which have not been shown in Fig. 3.6. The blue-grey cylindrical housing to the right of center in Fig. 3.7 contains the PMT; the 5320 Å filter, F, (not visible) is attached to the front face of the housing. The liquid-nitrogen dewar and valve (orange handles)/tubing assembly immersed in it are relevant to quartz-probe soot precursor hydrocarbon species sample collection and will be discussed further on.

For an aerosol with a monodisperse size distribution, and for which the refractive index is known, size, number density and volume fraction may be determined by a combination of only two measurements, extinction and scattering (Ref. 3.23). There is one inconvenience in applying this particular sizing method, which is that several apparatus parameters such as sample volume size and photomultiplier sensitivity must be known, and the latter may not always be estimated accurately. This difficulty may be overcome, however, by making an additional Rayleigh measurement of scattered light from room temperature air or other gas of known composition, and thereby "calibrating" the apparatus. Alternatively, ratios of Mie to known Rayleigh intensities may be used to ratio-out dependences on apparatus parameters. This procedure was used in the premixed flame work reported here, and the details of it are as follows.

PREMIXED FLAME FUEL-ADDITIVES APPARATUS

Burner, soot and precursor detection

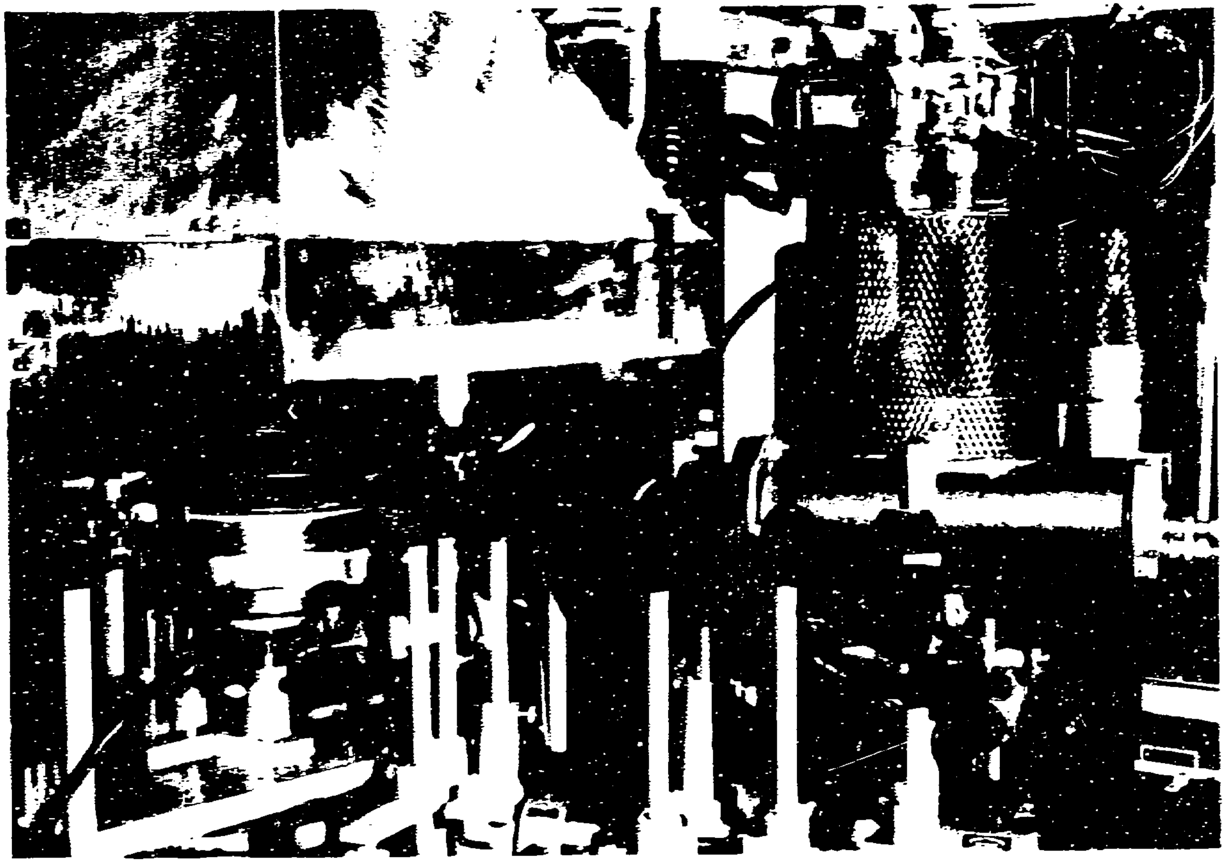

89—7—41—8

89—2648—[illegible]

For Mie scattering the intensity, I_M, is given by

$$I_M = (\lambda/2\pi)^2 \, I_M^o \, \phi \, N \, \Omega \, \ell \, \epsilon \qquad (3.1)$$

where λ is the wavelength of the incident and scattered light; I_M^o, the incident laser intensity; ϕ, the complex function of refractive index, wavelength, particulate size, scattering angle, and light polarization direction; N, the number density of particulates; Ω and ℓ, the light collection solid angle and sample length, respectively; ϵ, the light collection efficiency. For Rayleigh scattering the intensity, I_R, is given by

$$I_R = I_R^o \, n \, (\partial\sigma/\partial\Omega) \, \Omega \, \ell \, \epsilon \qquad (3.2)$$

where I_R^o is the incident laser intensity for Rayleigh scattering; "n", the number density of molecular scatterers; $\partial\sigma/\partial\Omega$, the differential Rayleigh cross-section; Ω, ℓ and ϵ as in Eq. (3.1) above. By combining Eqs. (3.1) and (3.2), it is readily apparent that

$$\phi N = (I_M/I_M^o) \, (I_R/I_R^o)^{-1} \, (2\pi/\lambda)^2 \, n \, (\partial\sigma/\partial\Omega) \ . \qquad (3.3)$$

The left-hand side of Eq. (3.3) is basically the product (or function) of both size and number density, while the right-hand side of the equation contains parameters which are either known constants (n, λ, $\partial\sigma/\partial\Omega$) or are measured experimentally. Importantly, Eq. (3.3) does not contain any difficult to estimate apparatus parameters; however, it is not sufficient, clearly, to separately determine particulate size and number density. For this purpose an additional measurement is required, to which end optical extinction may be seen to be appropriate. The extinction is given by

$$I_e = I_e^0 \left[\exp\left(-N\sigma_e L\right)\right] \qquad (3.4)$$

from which it follows that

$$N\sigma_e = -L^{-1} \ln\left(I_e/I_e^0\right) \qquad (3.5)$$

where σ_e is the extinction cross-section; L, the extinction path length; I_e^0 and I_e the incident and transmitted light intensities, respectively; N as in Eq. (3.1) above. An expression suitable for determining size may be obtained by dividing Eq. (3.3) by Eq. (3.5), with the result that

$$(\phi/\sigma_e) = (I_M/I_M^0)\,(I_R/I_R^0)^{-1}\,(2\pi/\lambda)^2\, nL\,(\partial\sigma/\partial\Omega)/\ln\left(I_e/I_e^0\right) \qquad (3.6)$$

If the refractive index, $\hat{n}$, scattering angle, wavelength and polarization are taken as known, a procedure adopted here ($\hat{n} = 1.94 - 0.66\,\hat{i}$, Ref. 3.25), then (ϕ/σ_e) is a function of size alone, and since the right side depends on known constants and measured quantities, size may be determined from the preceding equation. As pointed out above, in Mie theory (ϕ/σ_e) is a complex function. Fortunately, however, it is computationally tractable, and at UTRC (Ref. 3.24) and elsewhere tabulations of ϕ, σ_e and (ϕ/σ_e) versus size are available using computer codes. The remaining evaluation of soot parameters is straightforward. Having diameter, D, and σ_e from the code, Eq. (3.5) may be used to evaluate N. Then, the volume fraction, f_v, is calculated (not measured!) from $f_v = \pi(D^3/6)N$.

The approach outlined above is applicable to a monodisperse aeros[illegible]t not general to a polydisperse one since then more than two particulate parameters are involved. If, however, the width of the polydispersion is assumed known, then the preceding approach is applicable to it. The parameters ϕ and σ_o in the equations above are replaced by $<\phi>$ and $<\sigma_o>$, where the braces that enclose the preceding parameters indicate that these quantities are averaged over a distribution function; N, the total number density, retains its previous meaning. Evaluation of mean size, $\bar{D}$, and total number density follows from equations very similar to Eqs. (3.3) and (3.5) above, with $f_v = (\pi/6)(\bar{D})^3N$. The preceding approach was taken here, where the polydisperse aerosol was taken to be described by a zeroth-order logarithmic size distribution (ZOLD) (Ref. 3.26). For it, the mean diameter, $\bar{D}$, is given by $\bar{D} = D_m \exp(3\sigma_o^2/2)$, where D_m is the modal value of D or that value at which the distribution function has its maximum value, and σ_o (taken equal to 0.3) is a measure of the distribution width. The justification for using ZOLD with $\sigma_o = 0.3$ is that a nearly identical lognormal distribution has been shown to describe actual soot sizes satisfactorily (Refs., 3.27 and 3.28), and because it is very similar to the self-preserving size distribution which many coagulating aerosols fit (Ref. 3.29). Finally, then, it should be noted that numerical values given in the text below for size, number density and volume fraction are appropriate respectively to $\bar{D}$, N and f_v as defined above in this paragraph.

Light scattering/extinction measurements were made for three different premixed flames whose principal combustion characteristics are given in Table 3.1. The measured extinction coefficients, in $cm^{-1} \times 10^{-3}$ units, were small for the three L = 57 mm flames at z = 15 mm, being 8.56, 11.25 and 16.59 for ETH1, ETH2 and ETH3, respectively. Table 3.2 gives results for measured soot parameters as a function of vertical position in flame ETH3. The data are for a condition in which no water is added to the flame. They are, nevertheless, representative since with water injection D_o, N_o and f_o change by less than 10% at, for example, $z = 15$ mm. The data in Table 3.2 display the well known size and volume fraction increase with residence time (or height), along with a concomitant decrease in number density for the coagulating aerosol. As such these data are not new (see, for example, Ref. 3.8); they serve principally to confirm the validity of the soot parameter characterization approach used here, and to provide a reference for the soot evolution stage (or residence time) at which detailed additive measurements were made. In this connection, preliminary tests demonstrated that all of the additives increased their effectiveness with residence time, but that the induced changes were small and difficult to measure for $z < 10$ mm. For this reason, efforts were limited to data collection at $z = 10$ and 15 mm. At 15 mm the additive effects were measurably large, but the measurement point was not so high as to overlap any turbulent zones near the flame stabilization plate. At $z = 10$ mm, the effects of shortened residence time could be observed; careful study of the interval $10 < z < 15$ mm was judged not necessary.

Data which show the effect of alkali and alkaline-earth chlorides on soot for flame ETH3 at $z = 10$ and 15 mm height are given in Tables 3.3 and 3.4 respectively. For these data, any additive induced change in D^o, N^o or f_V^o which is less than about 10% is not considered significant since systematic and other sources of error are of this order. Clearly, then, for flame ETH3 the alkaline-earth metals, i.e. Ca, Sr and Ba, are not effective at both 10 and 15 mm. On the other hand, three of the alkali metals perturb soot with a $\mathrm{Cs} > \mathrm{Rb} > \mathrm{K}$ order of effectiveness, the magnitude of the perturbation for each metal being greater at 15 than at 10 mm. Accordingly, the data demonstrate that additive influence increases with residence time, and since ionization potentials for the alkali metals ascend in the order $\mathrm{Cs} < \mathrm{Rb} < \mathrm{K} < \mathrm{Na} < \mathrm{Li}$, their relative effectiveness is in inverse relation to the latter potential. This result is very similar to that obtained by us and others in diffusion flames (Refs. 3.4, 3.6 and 3.2), and by others in premixed flames (Ref. 3.8).

TABLE 3.2

Dependence of soot size (D_o), number density (N_o), and volume fraction (f_o) on vertical position for zero aspiration rate of the 0.1 molar metallic salt solution. Data are for flame ETH3.

z(mm)	D_o(Å)	N_o(cm^{-3} x 10^9)	f_o(cm^{-3}/CM^{-3} x 10^{-7})
6	42	903	0.35
7	84	159	0.49
8	135	48	0.61
9	172	33	0.88
10	222	16	0.94
11	264	11	1.08
12	295	9	1.16
13	312	8	1.33
14	329	8	1.46
15	348	7	1.52

TABLE 3.3

Soot parameters in a metal seeded flame(D,N,f_v) relative to those for water injection alone (D^o, N^o, f_v^o) for flame ETH3 at 10 mm height. For water alone: D^o = 215 Å, $N^o = 17 \times 10^9$ cm^{-3}, $f_v^o = 0.88 \times 10^{-7}$ cm^{-3}/CM^{-3}. Aspirated solutions: 1/10 molar MCl (M = Li, Na, K, Rb and Cs), $CaCl_2 \cdot 2H_2O$, $SrCl_2 \cdot 6H_2O$ and $BaCl_2 \cdot 2H_2O$.

Additive Metal	D/D^o	N/N^o	f_v/f_v^o
Li	1.00	1.01	1.00
Na	0.96	1.13	1.00
K	0.53	5.87	0.89
Rb	0.51	6.03	0.79
Cs	0.47	7.74	0.82
Ca	0.98	1.02	0.95
Sr	1.00	0.98	0.98
Ba	1.01	0.96	0.98

TABLE 3.4

Soot parameters in a metal seeded flame(D,N,f_v) relative to those for water injection alone (D^o, N^o, f_v^o) for flame ETH3 at 15 mm height. For water alone: D^o = 336 Å, N^o = 8 x 10^9 cm^{-3}, f_v^o = 1.63 x 10^{-7} cm^{-3}/CM^{-3}. Aspirated solutions: 1/10 molar MCl (M = Li, Na, K, Rb and Cs), $CaCl_2 \cdot 2H_2O$, $SrCl_2 \cdot 6H_2O$ and $BaCl_2 \cdot 2H_2O$.

Additive Metal	D/D^o	N/N^o	f_v/f_v^o
Li	1.02	0.95	1.01
Na	0.92	1.23	0.97
K	0.43	10.03	0.81
Rb	0.39	12.79	0.74
Cs	0.32	23.30	0.78
Ca	1.02	0.94	0.99
Sr	1.01	0.97	0.98
Ba	0.99	1.06	1.04

Data are given in Tables 3.5 and 3.6 for flames ETH2 and ETH3, respectively. The trends there are the same as in Table 3.4, except that the magnitude of the soot perturbation is reduced; indeed, said perturbation of f_v^0 for flame ETH1 is only marginally evident. More specifically, it is clear that for a given metal, and all of the three ratios, the perturbation of unseeded flame parameters increases in progressing from ETH1 to ETH2 to ETH3. For example, for potassium seeding and in the sequence ETH1, ETH2, ETH3 the data give: D/D^o = 0.59, 0.49, 0.43; N/N^o = 4.50, 7.73, 10.03; f_v/f_v^0 = 0.91, 0.88, 0.81. Since from Table 3.1 the principal difference among the combustion characteristics is temperature, and since it increases in the same sequence as just given, additive effectiveness may be judged to be regulated closely by the temperature of the flame.

TABLE 3.5

Soot parameters in a metal seeded flame(D,N,f_v) relative to those for water injection alone (D^o, N^o, f_v^o) for flame ETH2 at 15 mm height. For water alone: D^o = 283 Å, $N^o = 9.5 \times 10^9$ cm^{-3}, $f_v^o = 1.12 \times 10^{-7}$ cm^{-3}/CM^{-3}. Aspirated solutions: 1/10 molar MCl (M = Li, Na, K, Rb and Cs), $CaCl_2 \cdot 2H_2O$, $SrCl_2 \cdot 6H_2O$ and $BaCl_2 \cdot 2H_2O$.

Additive Metal	D/D^o	N/N^o	f_v/f_v^o
Li	1.02	0.91	0.98
Na	0.92	1.32	1.05
K	0.49	7.73	0.88
Rb	0.43	9.22	0.76
Cs	0.38	13.98	0.78
Ca	1.03	1.10	1.20
Sr	1.00	0.97	0.98
Ba	1.01	0.96	0.98

TABLE 3.6

Soot parameters in a metal seeded flame(D,N,f_v) relative to those for water injection alone (D^o, N^o, f_v^o) for flame ETH1 at 15 mm height. For water alone: D^o = 178 Å, $N^o = 30.4 \times 10^9$ cm^{-3}, $f_v^o = 0.88 \times 10^{-7}$ cm^{-3}/CM^{-3}. Aspirated solutions: 1/10 molar MCl (M = Li, Na, K, Rb and Cs), $CaCl_2 \cdot 2H_2O$, $SrCl_2 \cdot 6H_2O$ and $BaCl_2 \cdot 2H_2O$.

Additive Metal	D/D^o	N/N^o	f_v/f_v^o
Li	1.09	0.76	0.99
Na	0.99	1.10	1.05
K	0.59	4.50	0.91
Rb	0.53	6.55	0.98
Cs	0.47	8.26	0.88
Ca	1.03	1.00	1.09
Sr	1.02	0.94	1.00
Ba	0.99	1.04	1.00

3.4 Quartz Probe Species Sampling

A sampling probe and gas chromatographic analysis have been used to determine soot precursor hydrocarbon species concentrations in premixed flame ETH2 with and without a cesium additive present. The apparatus used for these measurements was identical to that shown in Fig. 2.17 above. Similarly, the approach taken in carrying out the measurements was essentially the same as that described in Section 2.4. The probe which was used for the premixed flame measurements is shown in Fig. 3.8. There was a slight change made in the shape of this probe so that it could be accommodated within the relatively narrow gap defined by the exit face of the burner and the lower face of the stabilization plate. It should be noted that the probe's aperture was not changed, being 0.15 mm diam. or about the same as for the previous one in Fig. 2.14 above. There was a small change made in the measurement approach as well. Whereas sampling in the diffusion flame was done typically at 3 Torr (pressure at probe tip), and in no case at greater than 10 to 12 Torr, all of the sampling of the premixed flame (steel cylinder bottle and liquid-nitrogen cooled u-tube) was done at roughly 30 Torr in order to increase the number of different species observed and enhance the sensitivity of their detection. Since the principal objective was to compare the concentrations of as many species as possible with and without an additive present, any slight distortion of the absolute concentration values introduced by sampling at higher pressure was judged to be of secondary concern. In at least two respects sampling of the premixed flame was more straightforward than was the case for the diffusion flame. First, flame perturbations of the type shown in Figs. 2.15 and 2.16 above were not observed for the premixed flame. This is evident in Fig. 3.9 where the probe is shown sampling the center of premixed flame ETH2 at 6 mm height without any visible distortion of the flame. Second, attempts were not successful to collect enough condensible hydrocarbons with the u-tube from the diffusion flame for meaningfully accurate concentration analysis. The probe plugged irreversibly after 5 min or so, or long before sufficient sample material was

QUARTZ SAMPLING PROBE

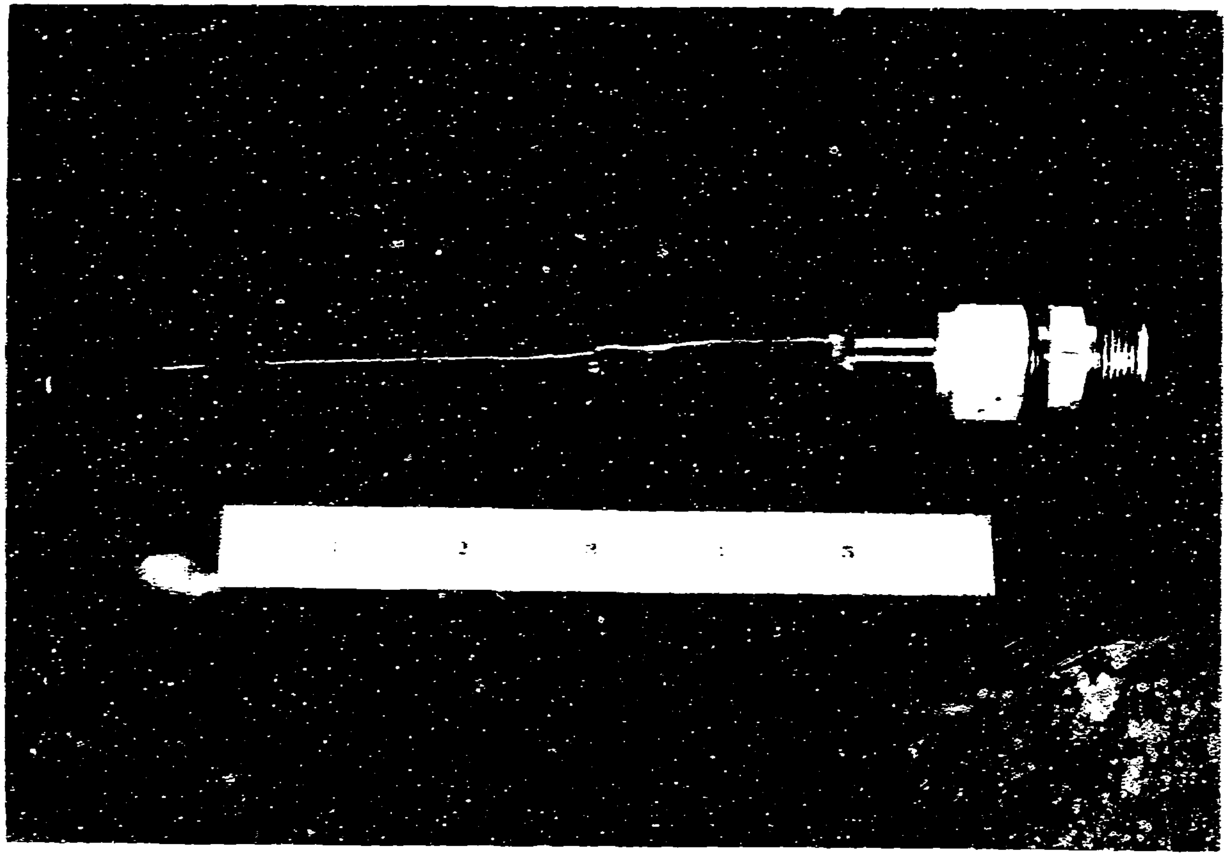

89—7—41—9

Fig. 3.9

PREMIXED $C_2H_4/O_2/N_2$ FLAME

Sooting condition, probe inserted

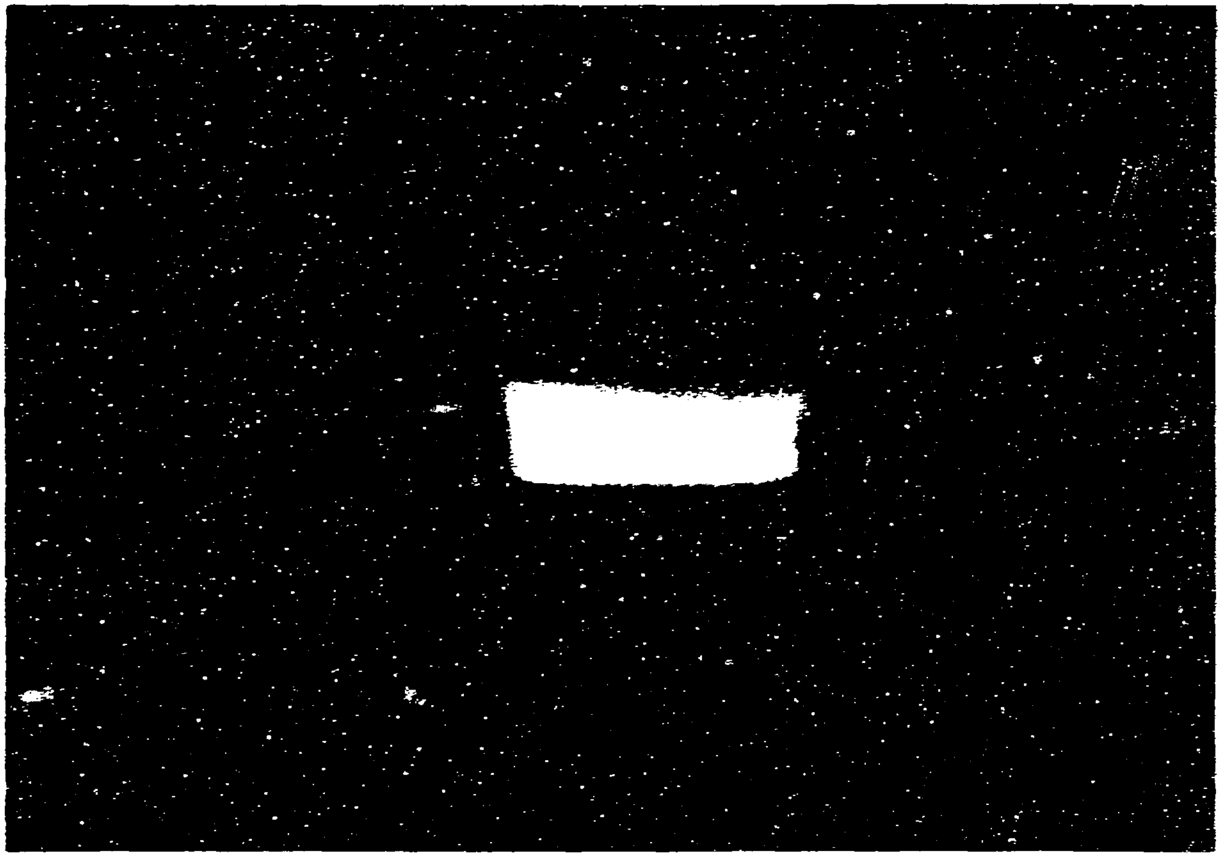

89—7—41—4

C89—264C—20

collected. For the premixed flame, there was no such difficulty, and collecting was done routinely for up to 15 min both with and without aspiration of a cesium salt into the flame.

A complete compilation is given in Table 3.7 of the gas-phase species collected in the Fig. 2.17 sample bottle, along with their concentrations at several different vertical positions in the flame with and without seeding present. The ppm concentrations are raw data; the number of significant figures is not representative of the measurement accuracy which is probably not much better than 5 to 10% for species at the 10^3 ppm or higher level, and even less for the other minor species like benzene and phenylacetylene. Accordingly, it may be concluded that there is no additive perturbation evident for any of the species in Table 3.7. This conclusion is perhaps even clearer in Figs. 3.10 and 3.11 wherein some of the data from Table 3.7 have been presented graphically.

Results which were obtained by freezing-out samples at 77°K in the Fig. 2.17 u-tube are given in Table 3.8. Again, the data are presented in raw form, unbiased by any corrections or reductions. The quantities given in the first two columns are relative (arb units) since it was deemed too difficult, too imprecise and beyond the scope of this work to determine the collection efficiencies of all of the species listed. Even the comparison of the amount of a given species present with and without cesium was not done (i.e., division of column 2 values by column 1) for fear that in taking the u-tube out (for "without cesium" analysis) and then replacing it (for "with cesium" collection) the trapping efficiency might not be the same. Accordingly, the data in Table 3.8 are presented in what is in our opinion a conservative manner; i.e., the results are referenced to the benzene concentration as in columns 3 and 4 in Table 3.8. With the exception of naphthalene (decrease), the trend is that of increased concentration for several of the detected species.

CH_4, C_2H_2, C_4H_2, C_6H_6 AND C_8H_6 CONCENTRATIONS IN PREMIXED $C_2H_4/O_2/N_2$ FLAME

With (■,▼,●,▲,◆) and without (□,▽,○,△,◇) ferrocene

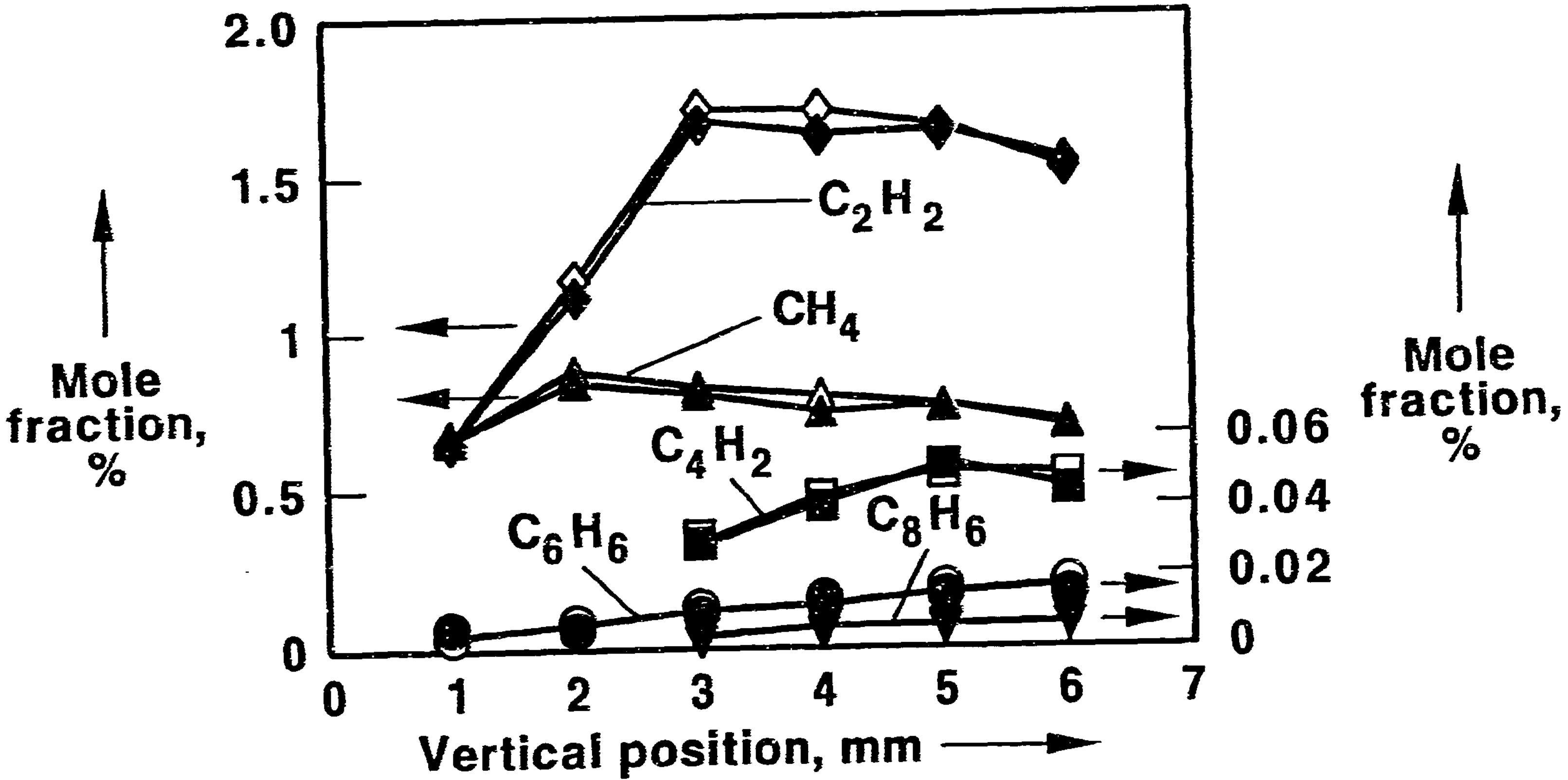

RC2745TX.0

Fig. 3.10

CO, H_2 AND CO_2 CONCENTRATIONS IN PREMIXED C_2H_4 / O_2 / N_2 FLAME

With (●, ▲, ◆) and without (○, △, ◇) ferrocene

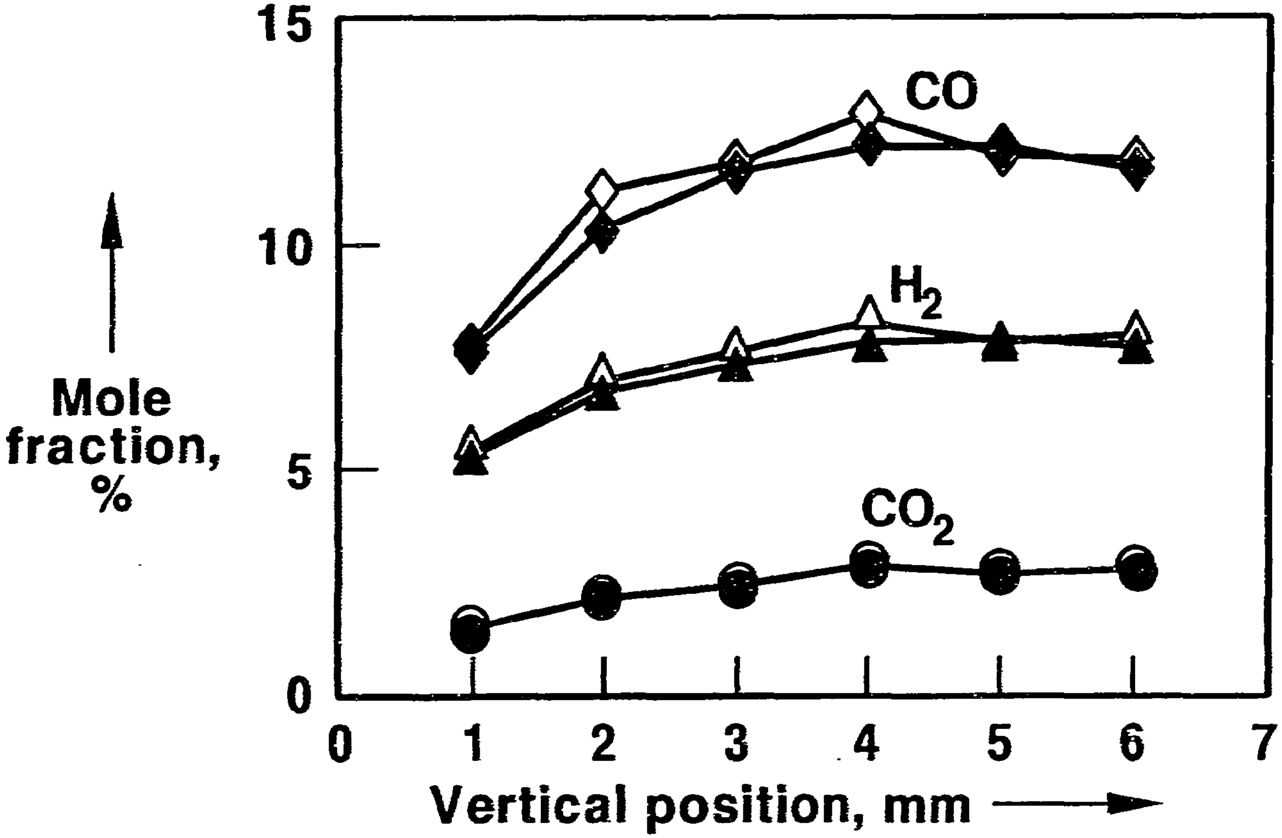

RC2745TX.009

TABLE 3.7

Selected gas phase species concentrations determined via chromatographic analysis of probe samples from flame ETH2. Unbracketed and bracketed numerical values are for water (alone) and 1/10 molar CsCl seeding, respectively.

		Concentration (ppm)					
	z(mm)	1	2	3	4	5	6
Chemical Symbol	**Species**						
H_2	hydrogen	53,476 [52,230]	69,132 [66,808]	75,319 [72,571]	82,009 [77,735]	77,349 [78,659]	79,458 [76,631]
CO	carbon monoxide	77,626 [75,174]	111,651 [103,355]	117,780 [115,768]	128,244 [121,380]	119,199 [120,350]	118,269 [115,280]
CO_2	carbon dioxide	14,514 [14,198]	21,483 [19,971]	23,857 [23,917]	28,415 [27,632]	26,825 [26,917]	27,302 [26,472]
CH_4	methane	6,723 [6,616]	8,837 [8,435]	8,280 [8,053]	8,018 [7,460]	7,706 [7,639]	7,037 [7,132]
C_2H_4	ethylene	48,185 [49,395]	20,576 [19,605]	1,967 [1,717]	495 [434]	450 [385]	296 [295]
C_2H_2	acetylene	6,634 [6,553]	11,758 [11,220]	17,260 [16,840]	17,229 [16,449]	16,690 [16,506]	15,256 [15,507]
C_2H_6	ethane	671 [660]	809 [710]				
C_4H_2	diacetylene			331 [324]	484 [463]	565 [577]	550 [502]
C_6H_6	benzene	38 [40]	71 [69]	119 [108]	133 [152]	179 [178]	199 [198]
C_7H_8	toluene			20 [17]			
C_8H_6	phenyl-acetylene			34 [33]	67 [50]	77 [70]	78 [82]

TABLE 3.8

Selected hydrocarbon species concentrations determined via chromatographic analysis of probe samples collected at 77°K from flame ETH2 at 6 mm height. Additive: 1/10 molar CsCl.

		Amount (arb units)		Amount Relative to Benzene	
		No addit.	Addit.	No addit.	Addit.
Chemical Symbol	Species				
CH_2CO	ketene	40.746	59.843	0.100	0.317
C_3H_6	propene	53.169	56.267	0.131	0.298
C_3H_4	methyl acetylene	2905.750	2339.610	7.137	12.410
C_4H_8	isobutene	34.067	24.015	0.0837	0.127
$1,3-C_4H_6$	1,3-butadiene	220.097	139.815	0.541	0.742
C_4H_2	diacetylene	2239.990	1206.67	5.502	6.400
C_4H_6	2-butyne	106.829	78.158	0.262	0.415
C_5H_6	trans 3-penten-l-yne	12.950	6.978	0.0318	0.0370
C_6H_6	benzene	407.116	118.533	1.000	1.000
C_6H_{10}	cyclohexene	93.739	47.357	0.230	0.251
C_7H_8	toluene	6.448	2.870	0.0158	0.0152
C_8H_6	phenylacetylene	70.722	32.772	0.174	0.174
C_9H_8	indene	10.126	4.533	0.0249	0.0240
$C_{10}H_8$	naphthalene	28.472	7.197	0.0699	0.0382

3.5 Flame Temperature

The temperatures of the three flames studied in this work have been estimated in two different ways. In one case, the temperatures were computed analytically for conditions appropriate to chemical equilibrium (Ref. 3.30), and these adiabatic temperatures are given in Table 3.1. Secondly, temperatures have been determined from the Wien equation using measured values of the flame's absorptivity and brightness temperature (Ref. 3.31 and 3.32). In Ref. 3.32 for example, the relation between true and brightness temperatures in given by $1/T_t - 1/T_{br} = (\lambda/c_2) \ln \epsilon_\lambda$, where T_t is the true flame temperature; T_{br}, the brightness temperature; λ, the emission wavelength ; $c_2 = 1.438$ cm°K, the second radiation constant; ϵ_λ, the emissivity at λ. If by Kirchhoff's law the emissivity and absorptivity, α_λ, are equal, then it follows that $1/T_t = 1/T_{br} + (\lambda/c_2) \ln \alpha_\lambda$. The quantities necessary to estimate T_t from the preceding equation were measured in this work. The brightness temperature was obtained using an optical pyrometer. Absorptivities ($= \sigma_o NL$) were measured in this work at both 5320 and 6328 Å. Values obtained at the latter wavelength, and given in Section 3.3, are close enough to values at the 6500 Å operating wavelength of the pyrometer not to introduce substantial error. In this way the true temperatures of ETH1, ETH2 and ETH3 at 15mm height were determined to be 1654, 1676 and 1681°K, respectively; the corresponding brightness temperatures were 1295, 1330 and 1365°K.

3.6 Metal Atom Concentrations

The concentrations of metal atoms (and cations) in the flame were not measured. Knowing such flame properties as the quantity of gas burned per second and the amount of aspirated salt exiting the face of the burner per second, it is possible to calculate the metal content per cm^3 of flame gas. Having a value for the nebulization efficiency of the aspirator is critical to this calculation. Fortunately, this efficiency has been determined carefully by others (Ref. 3.22) for the aspirator used in this work. It may be shown that the total number density, n_t, of metal present in the gaseous state (about equal to atomic number density for the alkalis) is given by (Ref. 3.33)

$$n_t = 10^{-3}\epsilon_n F_1 c N_A\ (298/T)/F_u\zeta\ (\text{in cm}^{-3}) \qquad (3.7)$$

where ϵ_n is the nebulization efficiency; F_1, the solution aspiration rate in cc/sec; c, the solution concentration in moles of salt per liter; N_A, Avogadro's number; T, the flame temperature; F_u, the volume flow of unburned gas in cm^3/sec; ζ (~1), the moles of burned gas per mole of the unburned initial mixture. Using the numerical values $\epsilon_n = 0.0159$, $F_1 = 1/30$, $c = 0.1$, $N_A = 6.022 \times 10^{23}$, $T = 1681°K$ (ETH3) and $F_u = 175$, it follows that $n_t = 3.23 \times 10^{13}$ cm^{-3}, or about 7 ppm of the total gas present.

In addition to the estimate of atom concentrations given above, the alkali cation concentrations may be estimated using the Saha equation (Ref. 3.31). This equation relates the relative concentrations of neutral, ions, and electrons by considering an equilibrium of the form, atom $\rightleftharpoons$ ion + electron. In this work, the flame is seeded with metal atoms having a relatively low ionization potential so that the number of metal cations and electrons may be assumed equal. Then, the cation number density, n_i, may be evaluated from

$$\log_{10}(n_i^2/n_t) = 20.94 - (5040W/T) - (3/2)\log_{10}(5040/T) \qquad (3.8)$$

where W is the ionization potential in eV. Using this approach, it may be shown for the cesium seeding of flames ETH1, ETH2 and ETH3 that n_i (in 10^{10} cm^{-3} units) = 8.55, 10.27 and 10.70, respectively. Another useful comparison is the relative number of different metal cations present for a given flame. Using Eq. (3.8), $n_t = 3.23 \times 10^{13}$ cm^{-3} from above, and appropriate numerical values for the ionization potentials of the alkali atoms, it is easy to show for flame ETH3 (T = 1681°K) that n_i (in 10^{10} cm^{-3} units) = 0.06, 0.15, 2.30, 4.03, and 10.70 for Li, Na, K, Rb and Cs, respectively.

3.7 Discussion

In this section, discussion is given of the results of this work, and where appropriate comparisons are made with earlier UTRC experiments as well as work done elsewhere by others.

The alkali chlorides were studied previously at UTRC as fuel additives in a sooting, $C_3H_8/O_2/N_2$ axisymmetric diffusion flame (Ref. 3.4). As in this work, the action of the metals on the particulates was, principally, to decrease size, increase number density, and either leave the volume fraction unchanged or decrease it. Given a sufficiently high additive molarity, the number density was also observed to decrease for the hotter of the two flames studied in Ref. 3.4; such a change in number density was not observed in this work. In Ref. 3.4, the additive effects on soot were most pronounced for the heavier metals, which, as pointed out above, differ from the lighter metals in that the former have relatively low atomic ionization potentials, leading to increased cation formation. Since the number of alkali atoms for a given molarity was approximately the same for all the alkali chlorides, the additive effectiveness for a given metal was in direct relation to the number of its alkali cations present. Our results for the alkali-seeded part of the premixed flame work reported here is fully supportive of the preceding conclusion. Indeed, the preceding logic may be used to explain the absence of any observed perturbation of soot by the alkaline-earth metals in this work. The ionization potentials of Ca, Sr and Ba are 6.11, 5.69 and 5.21 eV, respectively. Since these latter values are either nearly equal to or exceed the corresponding, high 5.39 eV value for Li, the alkaline-earth cation concentrations must in general be even lower than for lithium; hence, as for lithium there is no measurable soot perturbation. A difference between Ref. 3.4 and the present premixed flame work is that the former was done in T = 1973 and 2173°K flames, whereas here the flame temperature was of order 1700°K. This explains the roughly 10x larger Cs^+ concentration in Ref. 3.4 (see Table 1 therein) than estimated above in Section 3.6. For this reason as well, perturbations of soot equivalent in degree to those reported here were achieved at lower solution molarities in Ref. 3.4. Finally, there is one other difference between the two experiments discussed in this paragraph worthy of mention. In Eq. (3.7) above and the accompanying discussion, all of the alkali atom concentrations were taken to be the same and equal to 3.23×10^{13} cm^{-3}. This approach assumes that all of the metal is present in the flame as either M (atom) or M^+ (cation). This is a very good approximation for the alkalis, but in principle one other species may be present. In addition to the dissociation, $MCl \leftrightarrows M + Cl$, metal hydroxide formation may occur via, $M + H_2O \leftrightarrows MOH + H$ (Ref. 3.34). The MCl dissociation constants are very similar, but the probabilities for MOH formation differ a little for individual alkalis, leading to slightly different atom concentrations. Mindful of this issue, the M's were measured in Ref. 3.4, and not computed as was the case here. Except for the Na concentration, which was a little high, all of the atom concentrations were nearly equal and fell within the interval of $1\text{-}3 \times 10^{13}$ cm^{-3}. Accordingly, the assumption made here of equal numbers for all of the alkali atoms is a satisfactory approximation.

Experiments were also carried out earlier at UTRC in which alkali and alkaline-earth metals were added to a nearly two-dimensional laminar C_2H_4/air flame emanating from a symmetric Wolfhard-Parker burner (Ref. 3.6). Soot size, number density and volume fraction were determined from Mie scattering. Metal species concentrations were determined semiempirically by combining H-measurements with known equilibrium constants for the metal/radical reactions occurring in the flame. The flame temperature was measured via sodium line reversal. The alkaline-earth metals were observed to alter the three soot parameters above in accordance with a Ba > Sr > Ca order of effectiveness and, moreover, the effectiveness was a strong function of measurement position. The temperature and species measurements were used to relate this variation to a specific metal combustion product. Following this approach, a conclusion was reached which strongly implicated the charged MOH^+ (M = Ba, Sr, Ca) species as responsible for soot suppression. In addition, since significant suppression occurred with only a slight size change, the metal principally reduced the soot number density, which suggested that inhibitory intervention was most significant at an early soot formation stage. Alkaline-earth perturbations were clearly observed in this work, but was not the case here. This was probably true for two related reasons. First, the flame temperatures were considerably higher in Ref. 3.6 and, second, the solution molarities were also somewhat higher. For the alkaline-earths, cation formation occurs via the chemi-ionizing reaction, $M + OH \rightarrow MOH^+ + e^-$. In Ref. 3.6, the MOH^+ concentrations were of order 5×10^{10} cm^3 for Sr and Ba, or about the same as for Cs^+ in this work. Not surprisingly, then, the Sr and Ba were observed to perturb the soot in Ref. 3.6. In support of this, it may be estimated that the number of MOH^+ at 2000°K (Ref. 3.6) is more than 10x greater than at 1681°K (premixed flame ETH3). Finally, soot reduction is shown to be correlated with ionization potential for 10 different metals in Ref. 3.6 (see, in particular, Table 3.5 therein), in full agreement with results reported here.

Most of the results reported here support measurements of the effect of alkali and alkaline-earth metals on soot in premixed $C_2H_4/O_2/N_2$ flames carried out earlier by Haynes, et al. (Ref. 3.8). In this latter work, flame temperatures were somewhat higher than those here; hence, for the most part, additive effects were observed for both metal types. One flame (#6 in Ref. 3.8) was similar to flame ETH3 in temperature, being 1685°K. For it, Haynes, et al. observed essentially no change in any of the three soot parameters with barium seeding, which is consonant with our observations. On the other hand, for the same 1685°K a significant perturbation of soot by potassium was observed, which also agrees with our observations. Like Haynes et al., we found no evidence to support the enhancement of sooting by alkali metals which was reported earlier by Feugier (Ref. 3.7) for experiments in premixed $C_2H_4/O_2/N_2$ flames.

3.8 Conclusions

The principal conclusions of these premixed flame studies are as follows: 1) Alkali metals, provided they are present in sufficient quantity, are effective suppressants of soot formed in laminar hydrocarbon/air premixed flames. 2) The efficiency of a given metal is dependent almost exclusively on temperature and the metal atom's ionization potential. The higher the temperature and the lower the ionization potential, or equivalently the higher the number of metal cations, the greater the additive's influence on soot. 3) The perturbation of soot takes the form of decreased size and volume fraction and increased number density, the degree of perturbation increasing with residence time. 4) The conclusions in 1), 2) and 3) above are in essential agreement with the results of previous work done at UTRC and elsewhere. 5) The effect of the alkali metals on soot precursor hydrocarbon species has been done for the first time here. For the most part, the latter species are unaffected by the metals. There are one or two possibly intriguing exceptions to this such as the ketene and propene enhancement relative to benzene observed for cesium seeding. As discussed above in Section 2.7 for the ferrocene case, ketene increase is consistent with additive acceleration of acetylene oxidation via, $C_2H_2 + OH \rightarrow C_2H_2O + H$. In general, however, our view is that to firmly establish this or other similar phenomena for ketene, propene or other species, or to rule out such interventions altogether, additional and more precise data for the condensible hydrocarbons are required, especially with respect to absolute and not relative concentrations. 6) The alkali metals remove soot by creating more smaller particulates which then oxidize or burn out more rapidly at a late combustion stage. This work suggests intervention at an earlier stage, but this may not be stated with certainty at this time.

Section 3.0 References

3.1 Cotton, D. H., N. J. Friswell and D. R. Jenkins: *The Suppression of Soot Emission from Flames by Metal Additives*. Combust. Flame 17, 87-98 (1971).

3.2 Bulewicz, E. M., D. G. Evans and P. J. Padley: *Effect of Metallic Additives on Soot Formation Processes in Flames*. Fifteenth Symposium (Internat.) on Combustion, The Combustion Institute, Pittsburgh, PA, pp. 1461-1470 (1974).

3.3 Ndubizu, C. C., and B. T. Zinn: *Effects of Metallic Additives Upon Soot Formation in Polymer Diffusion Flames*. Combust. Flame 46, 301-314 (1982).

3.4 Bonczyk, P. A.: *In-Situ Optical Measurement of Additive Effects on Particulates in a Sooting Diffusion Flame*. Combust. Flame 51, 219-229 (1983).

3.5 Bonczyk, P. A.: *The Influence of Alkaline-Earth Additives on Soot and Hydroxyl Radicals in Diffusion Flames*. Combust. Flame 67, 179-184 (1987).

3.6 Bonczyk, P. A.: *Suppression of Soot in Flames by Alkaline-Earth and Other Metal Additives*. Combust. Sci. Tech. 59, 143-163 (1988).

3.7 Feugier, A.: *Effect of Metal Additives on the Amount of Soot Emitted by Premixed Hydrocarbon Flames*. Adv. Chem. Ser. 166 (Evaporation-Combust. Fuels), 178-189 (1978).

3.8 Haynes, B. S., H. Jander and H. Gg. Wagner: *The Effect of Metal Additives on the Formation of Soot in Premixed Flames*. Seventeenth Symposium (Internat.) on Combustion, The Combustion Institute, Pittsburgh, PA, pp. 1365-1374 (1979).

3.9 Shayeson, M. W.: Reduction of Jet Engine Exhaust Smoke with Fuel Additives. SAE Transactions 76, 2687-2694 (1968).

3.10 Friswell, N. J.: *Emission from Gas-Turbine-Type Combustors*, in Emissions from Continuous Combustion Systems (W. Cornelius and W. G. Angew, Eds.), Plenum, New York, pp. 161-182 (1972).

3.11 Bartholome, E., and H. Sachsse: *Catalytic Phenomena with Aerosols*. Z. Elektrochem. 53, 326-331 (1949).

3.12 Olson, D. B. and H. F. Calcote: *Ions in Fuel-Rich and Sooting Acetylene and Benzene Flames*. Eighteenth Symposium (Internat.) on Combustion, The Combustion Institute, Pittsburgh, PA, pp. 453-464 (1981).

3.13 Frenklach, M.: *Computer Modeling of Soot Formation Comparing Free Radical and Ionic Mechanisms*. Presented at AFOSR Contractors' Meeting on Combustion, Rocket Propulsion and Diagnostics of Reacting Flow, The University of Michigan, Ann Arbor, 19-23 June (1989).

3.14 D'Alessio, A., F. Beretta, and C. Venitozzi: *Optical Investigations on Soot Forming Methane-Oxygen Flames*. Combust. Sci. Tech. 5, 263-272 (1972).

3.15 Ritrievi, K. E., J. P. Longwell, and A. F. Sarofim: *The Effects of Ferrocene Addition on Soot Particle Inception and Growth in Premixed Ethylene Flames*. Combust. Flame 70, 17-31 (1987).

3.16 Haynes, B. S. and H. Gg. Wagner: *Soot Formation*. Prog. Energy Combust. Sci. 7, 229-273 (1981).

3.17 Browner, R. F., and A. W. Boorn: *Sample Introduction-The Achilles' Heel of Atomic Spectroscopy*. Anal. Chem. 56, 786A-798A (1984).

3.18 Willis, J. B.: *Atomization Problems in Atomic Absorption Spectroscopy - I. A Study of the Operation of a Typical Nebulizer, Spray Chamber and Burner System*. Spectrochimica Acta 23A, 811-830 (1967).

3.19 Stupar, J., and J. B. Dawson: *Theoretical and Experimental Aspects of the Production of Aerosols for Use in Atomic Absorption Spectroscopy*. Appl. Opt. 7, 1351-1358 (1968).

3.20 Novak, J. W., Jr., D. E. Lillie, A. W. Boorn, and R. F. Browner: *Fixed Crossflow Nebulizer for Use with Inductively Coupled Plasmas and Flames*. Anal. Chem. 52, 576-579 (1980).

3.21 Bonczyk, P. A. (Private Communication).

3.22 Maessen, F. J. M. J., P. Coevert, and J. Balke: *Comparison of Pneumatic Nebulizers in Current Use for Inductively Coupled Plasma Atomic Emission Spectrometry*. Anal. Chem. 56, 899-903 (1984).

3.23 Bonczyk, P. A.: *Measurement of Particulate Size by In-Situ Laser-Optical Methods - A Critical Evaluation Applied to Fuel-Pyrolyzed Carbon*. Combust. Flame 35, 191-206 (1979).

3.24 Cantor, A. J.: A Mie Scattering Computer Program. UTRC Report UTRC77-28, March (1977).

3.25 Senftleben, H., and E. Benedict: *Uber die Optischen Konstanten und die Strahlungsgesetze der Kohle*. Annalen der Physik 54, 65 (1918).

3.26 Kerker, M.: The Scattering of Light and Other Electromagnetic Radiation, Academic Press, New York pp. 356-357 (1969).

3.27 Prado, G., and J. Lahaye: *Physical Aspects of Nucleation and Growth of Soot Particles*, in Particulate Carbon Formation During Combustion (D. C. Siegla and G. W. Smith, Eds.), Plenum Press, New York, p. 143 (1981).

3.28 Wersborg, B. L., J. B. Howard, and G. C. Williams: *Physical Mechanisms in Carbon Formation in Flames*. Fourteenth Symposium (Internat.) on Combustion, The Combustion Institute, Pittsburgh, PA, pp. 929-940 (1973).

3.29 Friedlander, S. K.: Smoke, Dust and Haze - Fundamentals of Aerosol Behavior, Wiley, New York (1977).

3.30 Reynolds, W. C.: *STANJAN*, Interactive Computer Programs for Chemical Equilibrium Analysis, Stanford University (1981).

3.31 Gaydon, A. G., and H. G. Wolfhard: Flames - Their Structure, Radiation and Temperature, 4th Ed., Halsted Press (Wiley), New York, p. 296 (1979).

3.32 Penner, S. S.: *Optical Methods for the Determination of Flame Temperature - I.* Two-Color and Line-Reversal Techniques. Am. J. Phys. 17, 422-429 (1949).

3.33 Alkemade, C. Th. J., Tj. Hollander, W. Snelleman, and P. J. Th. Zeegers: Metal Vapours in Flames, Pergamon, New York (1982).

3.34 Pinta, M: Modern Methods for Trace Element Analysis, Ann Arbor Science Publishers, Ann Arbor, Mich. (1978).

APPENDIX I

Sooting Flame Thermometry
Using Emission/Absorption Tomography

by

Robert J. Hall and Paul A. Bonczyk
United Technologies Research Center

A sooting flame temperature measurement technique has been demonstrated that is based on emission/absorption tomography. The approach applies the algorithms of Fourier transform tomography to deconvolve local soot absorption coefficient and Planck function (temperature) from sets of parallel, line-of-sight measurements. The technique has the advantage that it is experimentally simple, and does not require involved theoretical analysis. There is also no sensitivity of the inferred temperature to possibly uncertain medium parameters. Its main limitation seems to be that it will not work well in optically thin environments, but this could be overcome in practice by seeding, and then performing all work at the wavelength of a seed resonance. When the spatial distribution of the absorber is reasonably uniform, the technique can accommodate very large optical thickness. A self-consistent comparison of measured, global radiation from a sooting ethylene flame with a radiative transfer calculation based on measured temperature and soot absorption parameters has been performed.

Introduction

Temperature is such an important indicator of the performance of combustion-driven systems that considerable effort has always been devoted to the development of temperature measurement techniques. Knowing it gives information about combustion efficiency, the rates of formation of unwanted particulates and pollutant species, and allows one to predict radiant heat transfer. Optical measurement approaches have been especially favored because of minimal disturbance of the medium being probed. Point techniques are coming to be regarded as inconvenient, however, because a measurement is made at only one location at a time, and the effort required to map out a large volume can be considerable. It is much faster to make a path-integrated measurement or a simultaneous set of them, along a line or lines over which the temperature is varying. There is a special advantage, therefore, to any algorithm which can reconstruct this varying temperature from path-integrated measurements, because with it a two-dimensional slice of the medium can be mapped out rapidly. A further requirement of any viable technique is certainly simplicity of data reduction; retrieval of temperature should not involve extensive and time-consuming computer code use, assumption of values for medium parameters that may not be well known, and should not rest on incompletely understood physics.

We have obtained good results in sooting laboratory flames using emission/absorption tomography. The technique is simple to implement experimentally, and data reduction is relatively uncomplicated. The deduced temperatures are not sensitive to assumptions about values of any medium parameters. Only relatively easily measured quantities, radiation intensity and absorption coefficient, are involved in the approach, which we now describe.

Theory

The reconstruction of internal flame or plasma temperatures from external, path-integrated intensity measurements has long been a problem of interest. For a gas in thermodynamic equilibrium, the line-of-sight emission intensity is given by the path integral (Ref. 1)

$$I_\lambda = \int \alpha_\lambda^{(a)}(s)\, B_\lambda\,(T(s))\, e^{-\int^{s} \alpha_\lambda^{(e)}(s')\,ds'}\, ds \tag{1}$$

where $\alpha_\lambda^{(a)}$ and $\alpha_\lambda^{(e)}$ are the local absorption and extinction coefficients and $B_\lambda\,(T)$ is the Planck function

$$B_\lambda\,(T) = \frac{2\,hc^2}{\lambda^5\,(\exp\,(\frac{hc}{\lambda kT}) - 1)} \tag{2}$$

If the absorption is due to molecules or small particles in the Rayleigh scattering range, scattering will be negligible, and $\alpha_\lambda^{(e)} = \alpha_\lambda^{(a)} = \alpha_\lambda$.

In the work of Porter (Ref. 1) and Kuhn and Tankin (Ref. 2), axisymmetric media were divided into concentric zones and the internal emission coefficients deduced by algebraic reconstruction. The internal absorption coefficients were calculated by making intensity measurements with and without an external source or mirror in the experiment. In Ref. 1 it is pointed out that one cannot use the familiar Abel integral equation formalism to deconvolve the internal emission coefficients because Eq.

(1) is not strictly of Abel equation form whenever there is finite absorption. It has been suggested more recently that Fourier transform tomography may be applicable to temperature measurement (Refs. 3-4) and an experimental demonstration in a laboratory flame has been reported (Ref. 5).

The application of tomography to temperature measurements is based on the fact that the expression for line-of-sight radiant intensity (Eq. 1) is the path integral of a property field, which is essentially the local emission rate. By making lateral intensity measurements at multiple angles of incidence, and applying Fourier transform-based reconstructive algorithms, it is possible to retrieve the internal values of this property field in a slice through the medium. To derive temperature, it is also necessary to perform an auxiliary measurement in which the local absorption coefficient is derived, using the same reconstructive technique.

We did not conduct a rigorous comparison of the tomographic reconstructive technique with other possible approaches, with the exception of "onion- peeling", which was found definitely to amplify experimental errors. As will be discussed, the Fourier transform method was found to give very good reconstruction of synthetic data. Unlike the Abel integral formalism, it appears to be applicable even for significant optical thickness. The reconstructive algorithm is also simple and fast. We use the convolution method of Ramachandran (Ref. 6); in particular the computer algorithm given by Shepp and Logan (Ref. 7). Our application follows that given in Refs. 3-4; the reader is referred there for further details.

Given a lateral intensity scan or projection P(r, θ) as given in Figure 1, the property field is reconstructed with the relationship

$$F(x, y) = \frac{a}{2N} \sum_{j=1}^{N} \sum_{k=1}^{M} P(r_k, \theta_j)\, \phi\, (x \cos \theta_j + y \sin \theta_j - r_k) \tag{3}$$

where a is the spacing between rays in a scan; M is the number of parallel ray paths in a scan; N is number of angular scans ($\theta_j = (j-1)\pi/N$); and ϕ is a filter function given by

$$\phi(r_k) = -\frac{4}{\pi a^2 \, (4k^2 - 1)} \quad k = 0, \pm 1, \pm 2, \ldots$$

(Shepp – Logan Filter)

(4)

$$\bar{\phi}(\mathrm{r_k}) = .4\ \phi\ (\mathrm{r_k}) + .3\ \phi\ (\mathrm{r_{k+1}}) + .3\ \phi\ (\mathrm{r_{k-1}})$$

(Modified Shepp – Logan Filter)

As our experimental projections were relatively free from noise, we saw no difference between the two filters. For the axisymmetric flames, all projections are the same, and only one experimental projection has to be made.

A number of computer experiments were performed to test the reconstructive capabilities of the algorithm. Axisymmetric temperature and absorption coefficient profiles were assumed, and synthetic projections were calculated numerically. The projections were then input to the deconvolution code, and the ability to reconstruct the temperature field tested. For spatially uniform absorption coefficient profiles, the algorithm could retrieve the input temperatures up to absorption coefficient-radius products of at least two, which represents fairly significant optical thickness. For thickness much beyond this, errors started to appear. The great sensitivity of Planck function to temperature (approximately T^4) had led to concern about dynamic range problems along paths with wide temperature variations, but this was not revealed by the computer experiments when the local absorption was uniform. When the local absorption is non-uniform, the accuracy of the temperature reconstructions can, in certain cases, be unsatisfactory. Regions of very weak absorption or those that combine weak absorption and low temperature will not always give satisfactory reconstructions; examples of this will be shown in the experimental sooting flame results. A very strongly absorbing annulus can obscure the centerline region of a medium, and lead to inaccurate predictions there. On the whole, however, the synthetic reconstructions gave encouragement to the use of tomographic procedures for temperature measurement in flames.

Experimental Arrangement

The experimental apparatus used in our investigations is shown in Figure 2. The source employed was a tungsten filament lamp which radiates as a grey body. The axisymmetric flame was positioned on a translatable mount; at a given vertical height above the burner surface, the required projections were generated by moving the flame transverse to the optical axis. Transverse resolution is defined by the 100 micron vertical slit, and the vertical resolution by the 1.5mm diameter optical fiber. As required for path-integrated measurements, the focal lengths of the lenses which bring the source radiation to a focus at the center of the flame, together with the vertical slit dimensions, are such as to create a large depth of field in the longitudinal or optical direction. This was verified by translating the flame in the longitudinal direction and observing no change in the intensity. (Conventional Kurlbaum can be performed by substituting a pin-hole for the vertical slit, giving fine longitudinal resolution.) Because we wanted to avoid having to make estimates of soot particle scattering, all work was performed at a wavelength of one micron where the size parameters are such that scattering should be small, and measured extinction can be equated to absorption. Other wavelengths could be selected by substituting for the one micron filter. The detection apparatus consisted of a photomultiplier and lock-in detector; the output signals were recorded on chart paper, and transferred manually to the computer for analysis.

The experimental procedure consists of making two projections at each vertical height; one with the source on, and the other with it off. Because the flames we investigated were axisymmetric, all projections at different angles of incidence are the same, and only one angle of incidence need be considered experimentally. The difference between the two projections defines the source transmission profile, which is readily deconvolved to yield the local absorption coefficient. Deconvolution of the flame emission profile yields the local value of the product of absorption coefficient, Planck function, and self-absorption factor. Knowledge of the previously derived absorption coefficient makes it possible to calculate the Planck function and thus the local temperature. It is highly desirable to derive temperature by measuring the Planck function because of the sensitive dependence of the latter on the former (approximately T^4) A 10% measurement error in the Planck function, for example, will be equivalent to roughly a 2% temperature error. It is also apparent that any error in absorption coefficient will generate an equivalent error in Planck function. The suggestion of Kuhn and Tankin (Ref. 2) that temperature error in this type of measurement is approximately the fourth root of the absorption coefficient error seems reasonable. Because the latter is a quantity that can in principle be measured very accurately, there is the promise of precise temperature measurements. Accurate absorption measurements are unlikely to be made in the limits of extreme optical thinness or thickness; it is expected that regions of moderate absorption will yield the best results. Temperature measurements cannot be reliably made in regions containing little soot.

The Planck function measurements need to be placed on an absolute basis for temperature determination, and this is done by performing an optical pyrometer measurement of the tungsten filament temperature. The filament current can be set at an arbitrary value, and the emission measurements are put on an absolute scale in this way. If the lens transmission losses on the filament side of the flame are significant, as they were in our experiments, this needs to be accounted for in the calibration. Losses at windows need to be accounted for in a similar fashion.

In these first experiments, we generated the projections by a tedious procedure of translating the flame relative to the optical axis, and then transferring by hand the intensities from the recorder paper to the computer for data reduction. The technique should lend itself rather easily to the use of detector arrays with computer interfacing for much more rapid and accurate data acquisition and reduction. Both the experiment and the analytical data reduction procedures are relatively simple, and do not require major investments in equipment or software. Real time temperature measurements should be possible.

Experimental Results

A. Ethylene Flame

We first investigated an ethylene-air diffusion flame. The burner consists of a 1 cm diameter fuel tube surrounded by a honeycomb mesh to straighten the air flow. It was extensively investigated with CARS (Ref. 8) and is not too dissimilar from the flame investigated by Santoro and co-workers, who used thermocouples and laser particle sizing (Refs. 9-10). The luminous tip height is 76 mm.

Figure 3 shows sample data from the ethylene flame at a height of about 4 cm above the burner surface. The filament current is set at an arbitrary value which keeps the source intensity on scale; the intensity scale has been calibrated using a pyrometer measurement as discussed in the experimental section. The actual recorded projections show slight asymmetries which have been removed by folding about the centerline and averaging. Subtracting the flame projection from the combined projection of the flame plus the source yields the source radiation transmission projection as shown. The path-integrated absorption is about 10%, which should be just adequate for accurate work. This is inverted by Equations 3-4 to yield the soot absorption coefficient profile shown in Figure 4. Typically 100 adjacent intensities were input to the data reduction programs, with 50-100 angles of incidence assumed. Even though the soot probably consists of chain-like aggregates which are not in the Rayleigh range, the Rayleigh relationship

$$\alpha_\lambda = C \frac{f_v}{\lambda} \tag{5}$$

between absorption coefficient and volume fraction f_v should still be valid. The first-order theory of scattering by mass fractal aggregates (Refs. 11-12) shows that the absorption coefficient of an aggregate of spheroids is simply the sum of the spheroid absorptions if the latter are in the Rayleigh range, and if multiple internal scattering effects are small.

The constant C is a function of the soot index of refraction; if one assumes the value used in Ref. 9, it has the value 4.9×10^4 for α_λ in cm^{-1} and λ in microns. Thus the peak absorption in Figure 4 corresponds to a soot volume fraction of about 10^{-6}. This is slightly higher than the peak values reported in Ref. 9. The temperatures deduced by deconvolving the flame projection in Figure 3 are shown in Figure 5. At the centerline, the temperature of ca. 1700°K agrees favorably with the 1650°K value reported for CARS (Ref. 8). It is perhaps 100°K higher than thermocouple measurements (Ref. 9), but the flames are not identical. There is a discontinuity in the temperature at a radius of about .27 cm because the soot concentration drops abruptly to zero.

The calculated soot absorption profiles as a function of height graphically depict the evolution of the soot as shown in Figure 6. The soot forms in an annulus low in the flame. Eventually, it fills the center of the flame as the wings contract. At a height of 6 cm, the wings are barely detectable, and low absorption precludes measurement beyond 6.5 cm.

The annular shape of the soot distribution low in the flame presents a problem for temperature measurement, as depicted in Figure 7. The inferred local emission rate, which is the product of absorption coefficient and Planck function, is plotted for a vertical height of 1.5 cm. As seen, the emission in the center region of the flame is extremely weak, and it is futile to attempt to deduce temperature in such regions. We employed a restriction that the local emission rate be greater than 10% of the peak value at a given height to qualify for temperature determination. With this restriction, the 1.5 cm temperature distribution is as shown in Figure 7. Higher in the flame, the soot occupies the center region, and the inferred soot temperatures tend to be relatively flat with values of about 1700°K, as shown in Figure 8 for a height of 5.5 cm. This qualitative behavior seems to be consistent with the thermocouple measurements of Ref. 9, if one restricts attention to the sooting regions. Because of insufficient absorption, we were not able to probe high enough in the flame to see any discernable fall-off of temperature.

Substitution of a 100μ pin-hole for the vertical slit in Figure 1 makes possible conventional Kurlbaum or soot reversal measurements with a longitudinal resolution of 1 mm. As discussed, one needs to make corrections for window and lens transmission losses on the source side of the flame. Further, one needs to account for absorption of the source radiation prior to the focal volume; the maps of absorption coefficient generated in these studies make this possible. Kurlbaum was performed at two heights, 32.5 mm and 40 mm, above the burner surface. At 32.5 mm, the line reversal measurement was 1848°, while the tomography prediction averaged over 1 mm around the centerline was about 1770°K. AT 40 mm, the line reversal gave 1794°K, and the tomography predictions averaged over 1 mm gave about 1720°K.

As part of the experiments on the ethylene flame, we performed a measurement of the global, wavelength-integrated radiation. The measurement was performed in the manner of Markstein (Ref. 13); a conventional, calibrated radiometer was placed sufficiently far from the flame that the latter could be approximated as a point source. The measured radiative power was then multiplied by 4π divided by the radiometer acceptance angle; the result was 36.3 Watts. For the ethylene flow rate of 3.85 cc/sec, this corresponds to 20% of the chemical enthalpy release, a result that is quite consistent with the results of Ref. 13. For an optically thin medium with an absorption coefficient having the Rayleigh form, the theoretical radiated power should be (Ref. 14).

$$\begin{aligned}\text{Radiated power} &= \int d\lambda \int_{4\pi} d\Omega \int dV\ \alpha_\lambda B_\lambda\ (T)\\ &= C' \int dV\ f_v\ T^5 \qquad (6)\end{aligned}$$

where C' has the value $2.97\text{x}10^{-10}$ (m.k.s) for the index of refraction of Ref. 14. Performing the above integration with our volume fractions and temperatures deduced from one micron measurements gave a value of 36.0 Watts. Of course, reasonable agreement is expected because our measurements are based on radiation, but the very precise agreement obtained suggests that the Rayleigh absorption law must be essentially valid, and that soot volume fraction is the concentration parameter needed for radiation prediction.

B. Iso-octane flame

We also employed the tomography technique in a highly sooting, iso-octane/air diffusion flame. Figures 9 and 10 show how the deconvolved soot concentration and temperature evolve with vertical height. Conventional Kurlbaum measurements were made at the centerline at heights of 20 and 30 mm. As seen in Figure 10, the soot absorption at 20 mm is weak and we could not measure a temperature tomographically there. However, the agreement at 30 mm was very good; Kurlbaum gave 1720°K and tomography 1705°K.

The deficiencies of the technique in the annular sooting zones low in the flames suggest that seeding to achieve a more uniform distribution of absorption might be a worthwhile idea. All work would be performed at the wavelength of a seed resonance (for example the sodium D line, if that were the seed), and the amount of seed introduced could be adjusted to achieve the desired moderate absorption.

Conclusions

We have obtained good diagnostic results in sooting flames using emission/absorption tomography. For the first time, a self-consistent examination of sooting flame radiation has been performed, with a comparison of measured radiative loss and theoretical predictions based on measured temperature and soot concentration. Although the optically thin flames investigated were not optimal for a demonstration of temperature tomography, results were obtained which agreed fairly well with CARS and Kurlbaum. The technique is experimentally simple, and only uncomplicated, fast data reduction procedures are required. It should lend itself to the use of detector arrays for very fast 2D and 3D data acquisition and reduction. The main drawback of the approach is that measurements cannot be made in regions of weak absorption; extreme optical thickness would also present a problem. The accuracy of the temperature measurements, probably now at the several percent level, might be improved by using a laser to make the crucial absorption coefficient measurement. Seeding to achieve a more uniform, moderate level of absorption should also improve the accuracy. In summary, there appears to be considerable promise to temperature measurement using tomographic deconvolution of line-of-sight radiation, and the technique is deserving of further attention and refinement.

Acknowledgements

The authors would to thank Joseph Sangiovanni and Robert Santoro for their help in clarifying certain ideas developed in this paper. They would also like to thank Kathi Wicks for her help in preparing this manuscript.

This research was sonsored in part by the Air Force Office of Scientific Research (AFOSR) and the Environics Division of the Air Force Engineering Services Center (AFESC, Tyndall AFB, FL) under AFOSR contract F49620-86 C-0054. The authors wish to thank Julian M. Tishkoff (AFOSR) and Paul Kerch (AFESC) for their interest in and support of this research.

References

1. R. W. Porter, "Numerical Solution for Local Emission Coefficients in Axisymmetric Self- Absorbed Sources", SIAM Review, 6, 228 (1964).

2. G. Kuhn and R.S. Tankin, "Spectroscopic Measurements to Determine Temperature and Carbon Particle Size in an Absorbing Propane Diffusion Flame", J.Q.S.R.T., 8, 1281 (1968).

3. H.G. Semerjian, S.R. Ray, and R.J. Santoro, "Laser Tomography for Diagnostics in Reacting Flows," AIAA-82-0584 (1982).

4. P.J. Emmerman, R. Goulard, R.J. Santoro, and H.G. Semerjian, "Multiangular Absorption Diagnostics of a Turbulent Argon-Methae Jet", J. Energy 4, 70 (1980).

5. H. Uchiyama, M. Nakajima, and S. Yuta, "Measurement of Flame Temperature Distribution by IR Emission Computed Tomography", Appl. Opt., 24, 4111 (1985).

6. G.N. Ramachandran and A.V. Lakshminarayanan, "Three-dimensional Reconstruction from Radiographs and Electron Micrographs: Application of Convolutions instead of Fourier Transforms", Proc. Nat. Acad. Sci. USA, 68, 2236 (1971).

7. L.A. Shepp and B.F. Logan, "The Fourier Reconstruction of a Head Section", IEEE Trans. on Nuc. Sci., NS – 21, 21 (1974).

8. L.R. Boedeker and G.M. Dobbs, "Temperature and Soot Correlations in Sooting, Laminar Diffusion Flames", UTRC85-51 (1985).

9. R.J. Santoro, H.G. Semerjian, and R.A. Dobbins, "Soot Particle Measurements in Diffusion Flames", Combust. Flame, 51, 203 (1983).

10. R.J. Santoro and H.G. Semerjian, "Soot Formation in Diffusion Flames: Flow Rate, Fuel Species, and Temperature Effects", Twentieth Symposium (International) on Combustion (The Combustion Institute, Pittsburgh, 1984) pp. 997-1006.

11. M.V. Berry and I.C. Percival, "Optics of Fractal Clusters Such as Smoke", Optica Acta, 33, 577 (1986).

12. R.D. Mountain and G.W. Mulholland, "Light Scattering from Simulated Smoke Aggregates", Langmuir, in press.

13. G.H. Markstein, "Relationship Between Smoke Point and Radiant Emission From Buoyant Turbulent and Laminar Diffusion Flames", in Twentieth Symposium (International) on Combustion (The Combustion Institute, Pittsburgh, 1984), pp. 1055-1061.

14. F.G. Roper, "Soot Escape from Diffusion Flames: A Comparison of Recent Work in this Field", Combust. Sci. Technol. 40, (1984).

LINE-OF-SIGHT PROJECTIONS

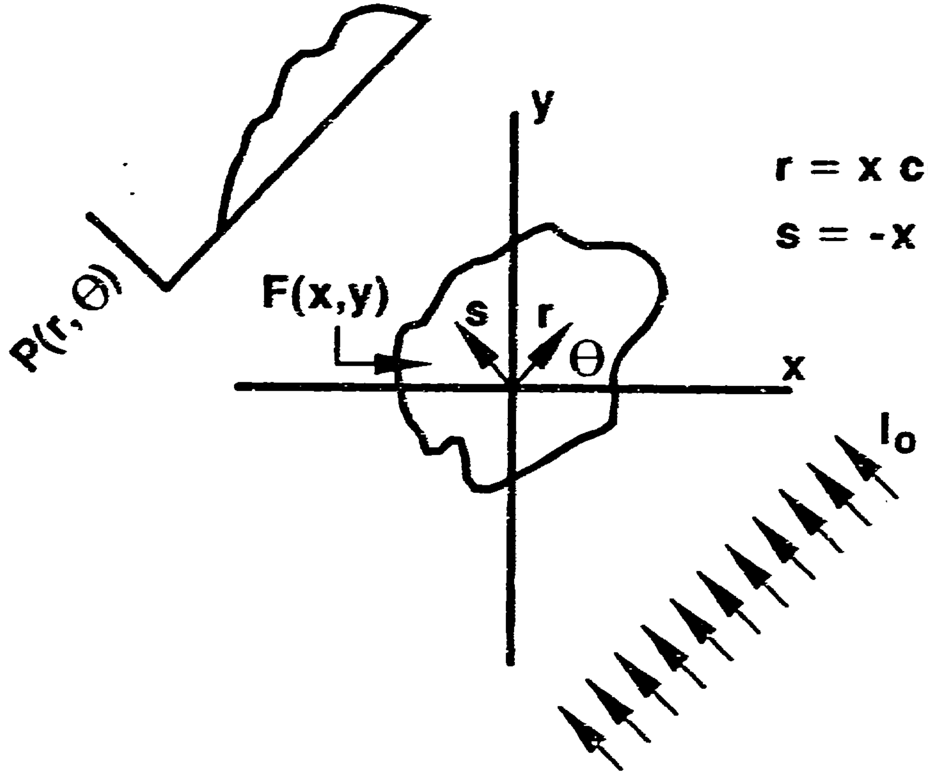

$r = x \cos\Theta + y \sin\Theta$

$s = -x \sin\Theta + y \cos\Theta$

(Absorption) $P(r,\Theta) = -\ln \left[I(r,\Theta)/I_o \right] = \int \alpha_\lambda(x, y) ds = \int F(x, y) ds$

(Emission) $P(r,\Theta) = \int \alpha_\lambda(s) B_\lambda(s) e^{-\int_s \alpha_\lambda(s') ds'} ds = \int F(x, y) ds$

Figure 1

RJ73TX.001

SOOT ABSORPTION / EMISSION SCHEMATIC

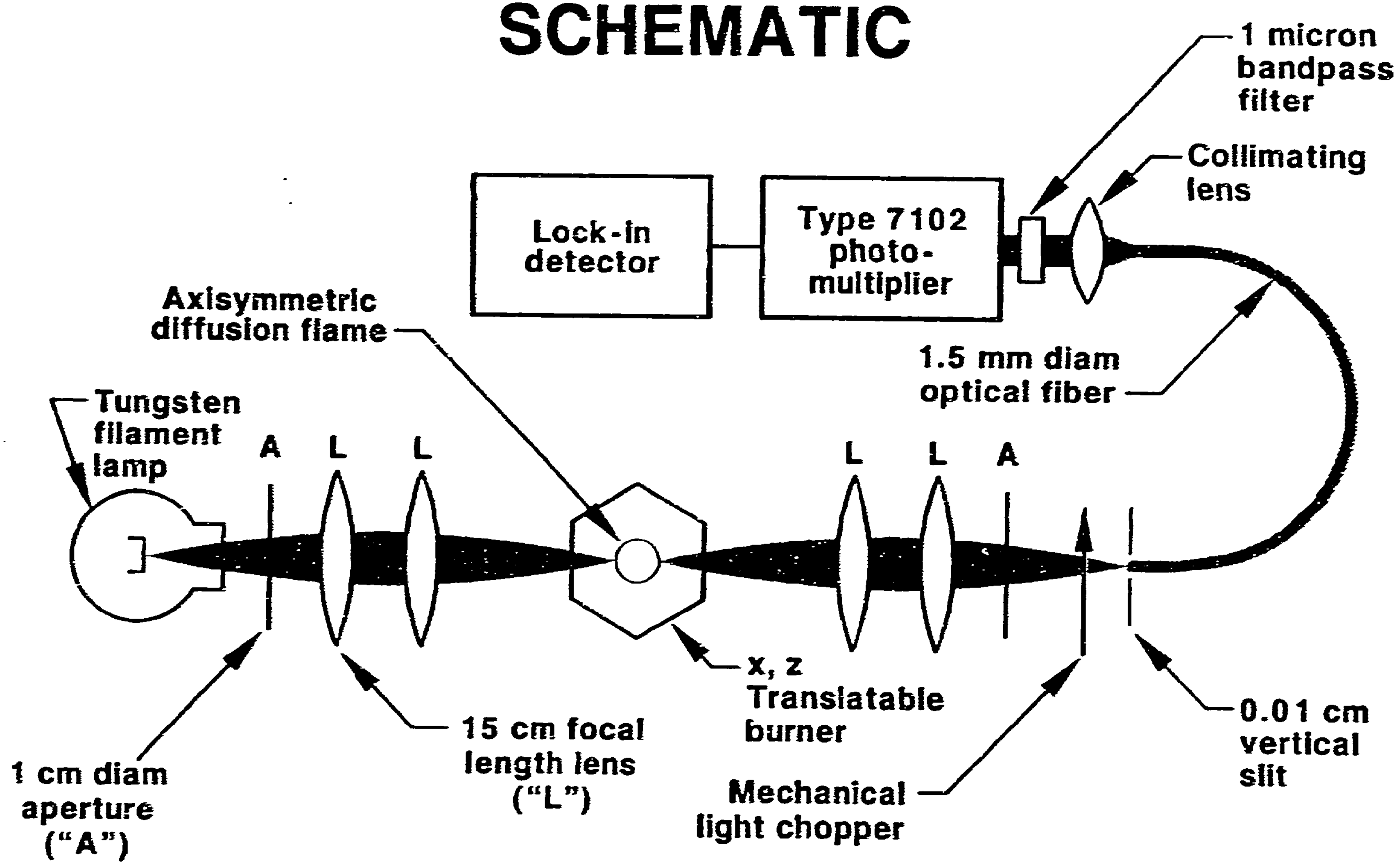

Figure 2

RK73TX.002

LINE-OF-SIGHT RADIATION AT 1 MICRON

Height = 4 cm

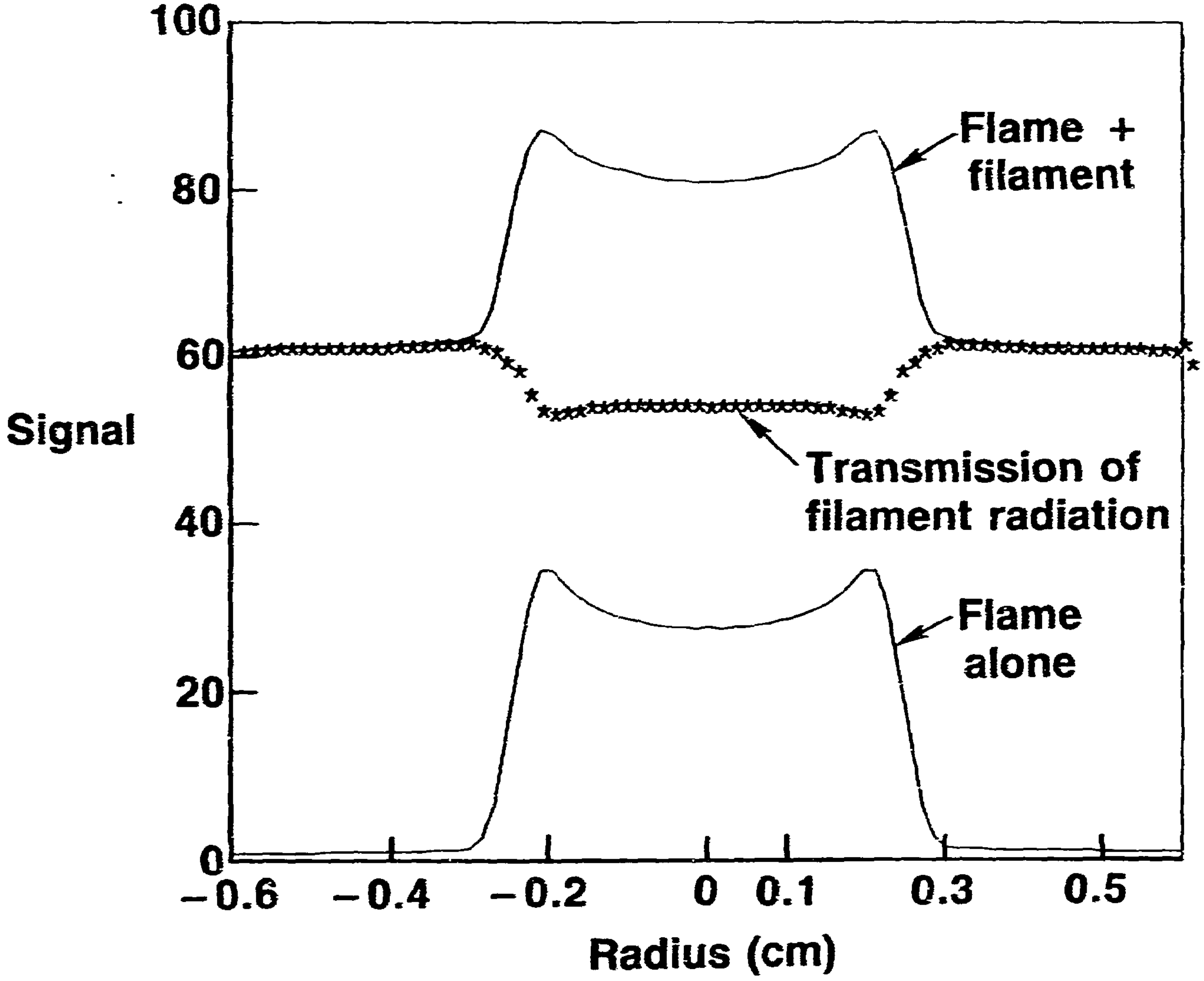

Figure 3

89—6—30—2

Figure 4

Soot Concentration in Ethylene—Air Diffusion Flame

Height = 4 Cm Above Burner

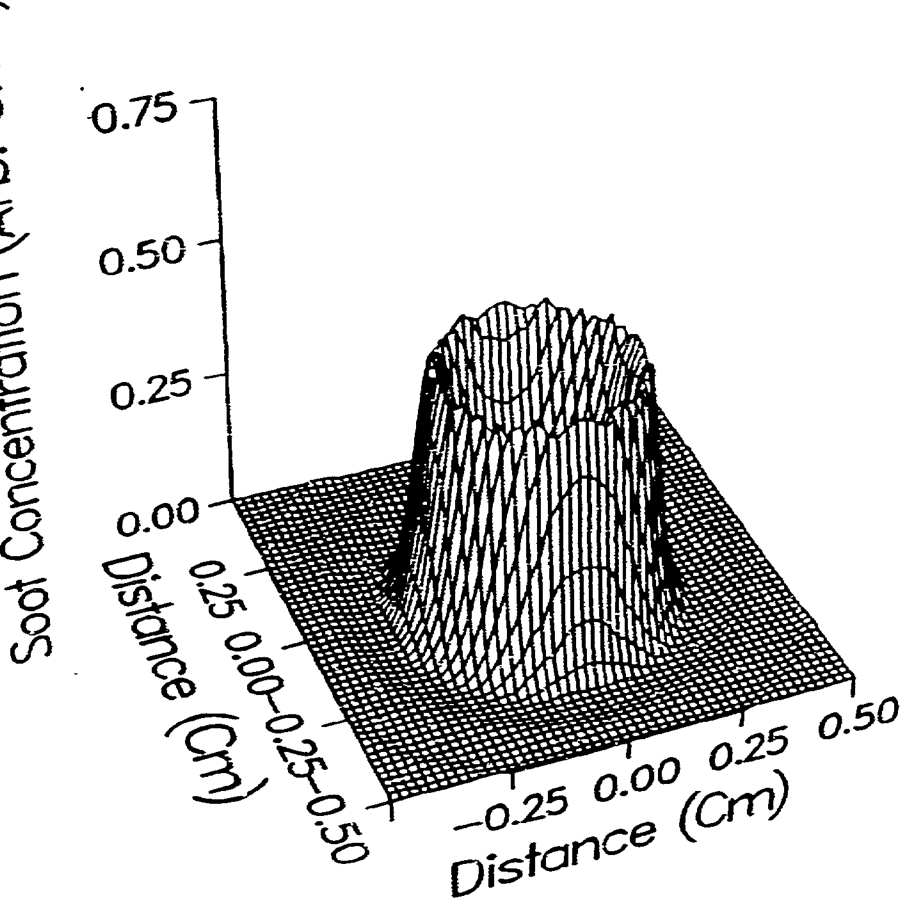

Figure 5

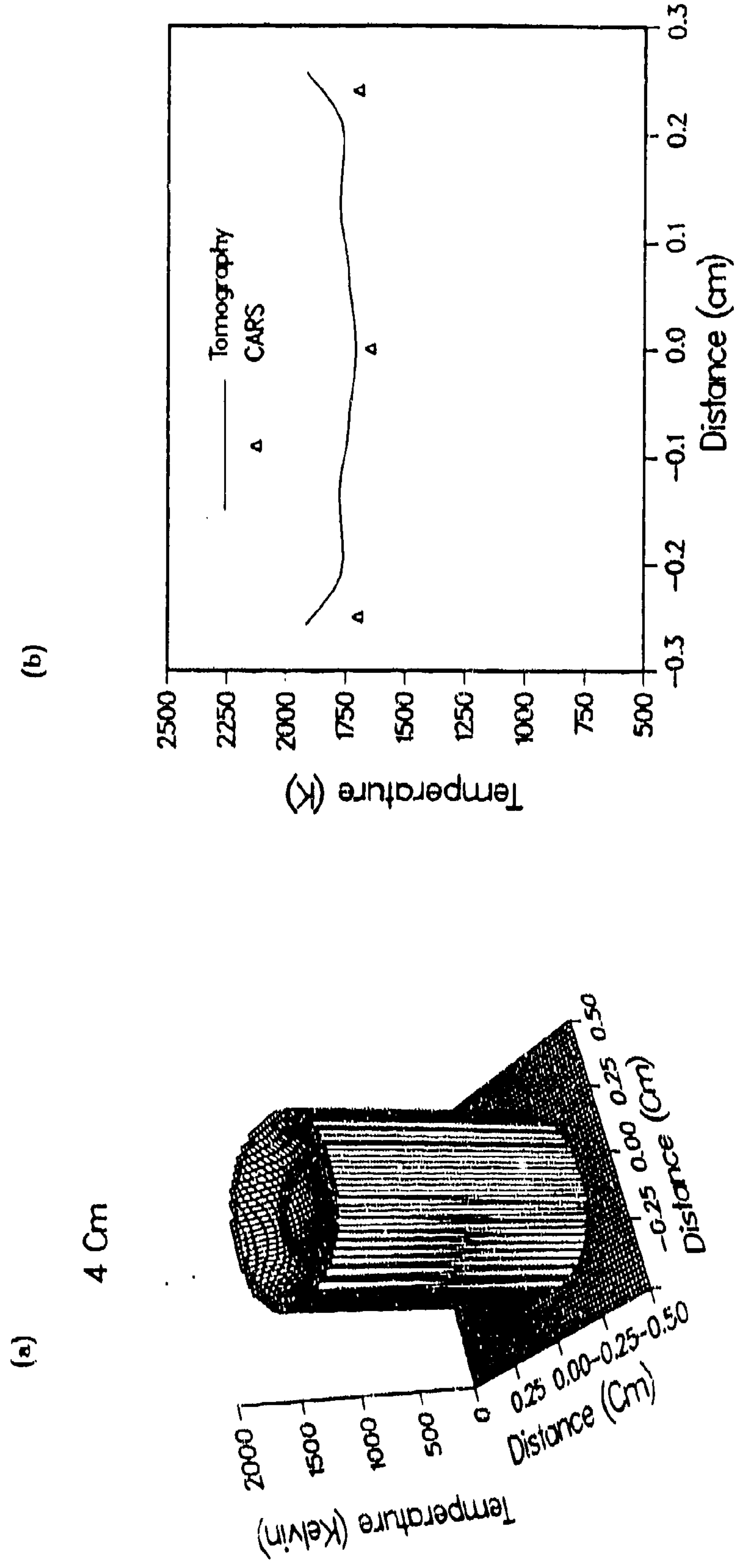
(a)
4 Cm
Temperature (Kelvin)
2000
1500
1000
500
0
0.25 0.00 −0.25 −0.50
Distance (Cm)
−0.25 0.00 0.25 0.50
Distance (Cm)
(b)
Temperature (K)
2500
2250
2000
1750
1500
1250
1000
750
500
Tomography
CARS
−0.3
−0.2
−0.1
0.0
0.1
0.2
0.3
Distance (cm)

Figure 6

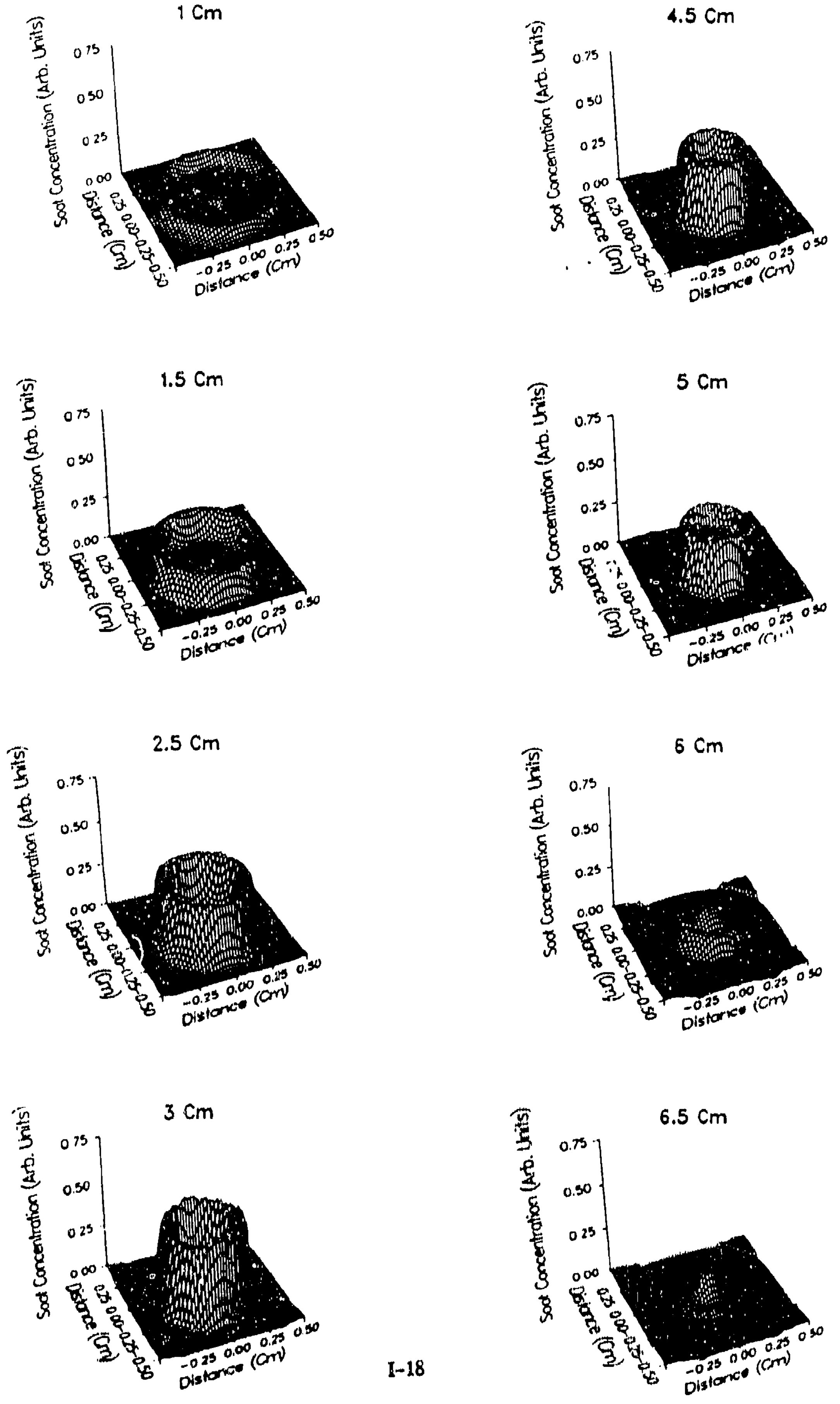
1 Cm
1.5 Cm
2.5 Cm
3 Cm
4.5 Cm
5 Cm
6 Cm
6.5 Cm
Soot Concentration (Arb. Units)
0.00
0.25
0.50
0.75
Distance (Cm)
0.25
0.00
-0.25
-0.50
Distance (Cm)
-0.25
0.00
0.25
0.50

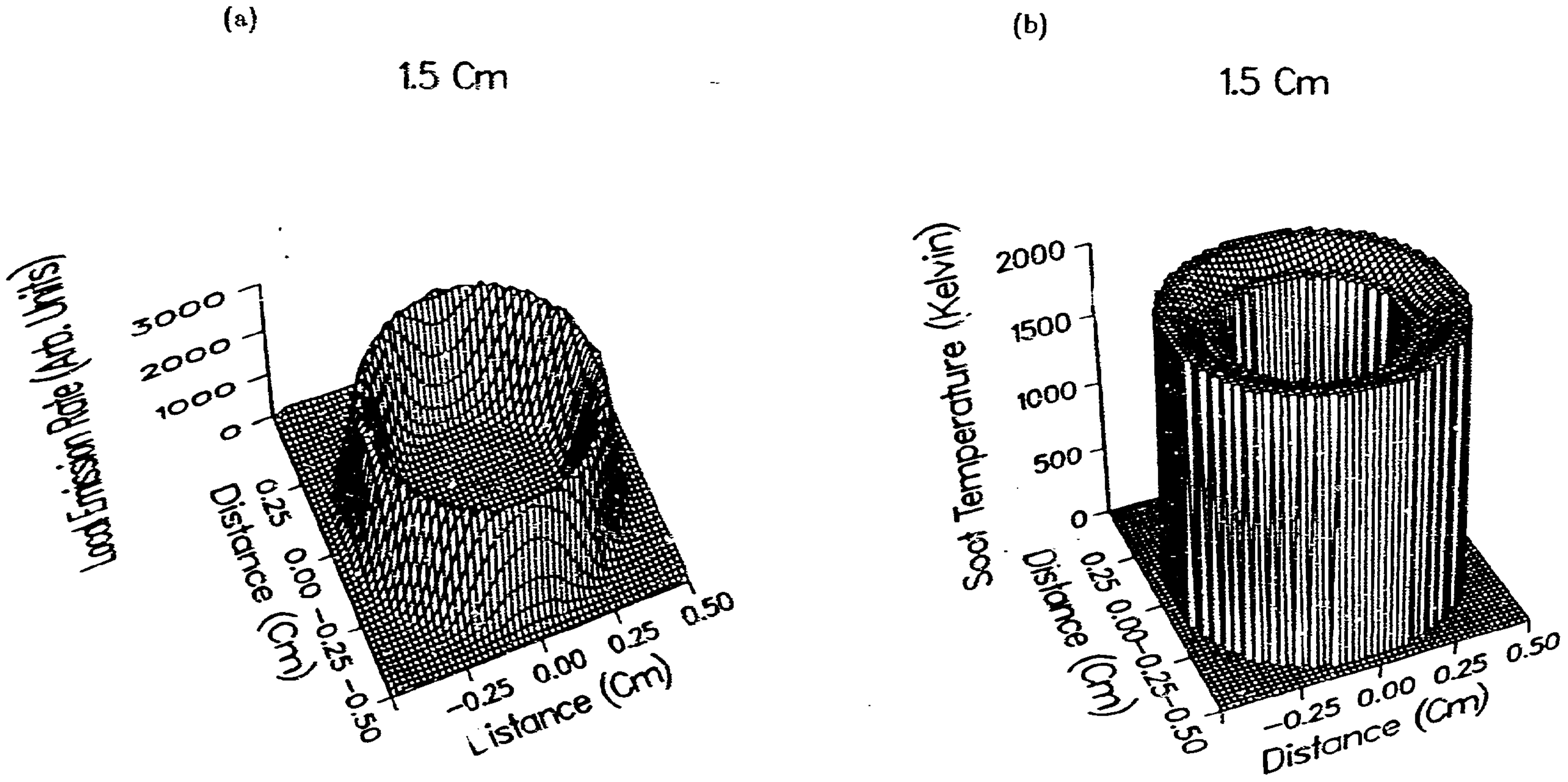
(a)
1.5 Cm
Local Emission Rate (Arb. Units)
3000
2000
1000
0
0.25 0.00 −0.25 −0.50
Distance (Cm)
−0.25 0.00 0.25 0.50
Listance (Cm)
(b)
1.5 Cm
Soot Temperature (Kelvin)
2000
1500
1000
500
0
0.25 0.00−0.25−0.50
Distance (Cm)
−0.25 0.00 0.25 0.50
Distance (Cm)

Figure 7

Figure 8

Soot Temperature in Ethylene–Air Diffusion Flame

Height = 5.5 Cm Above Burner

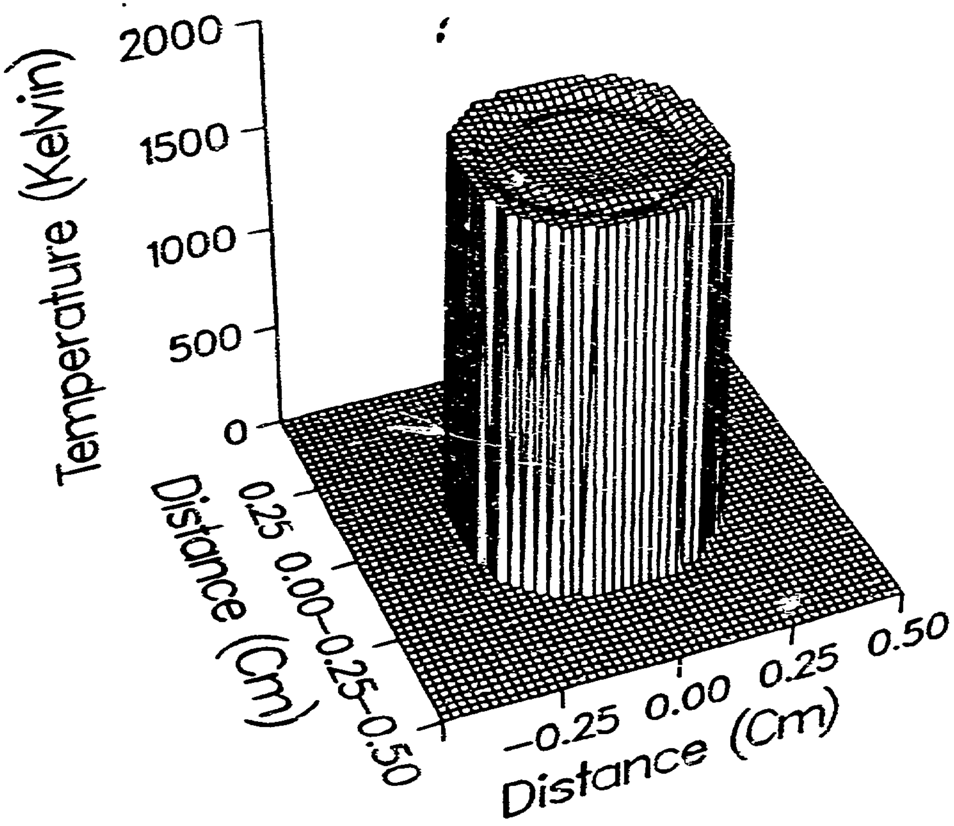

Figure 9

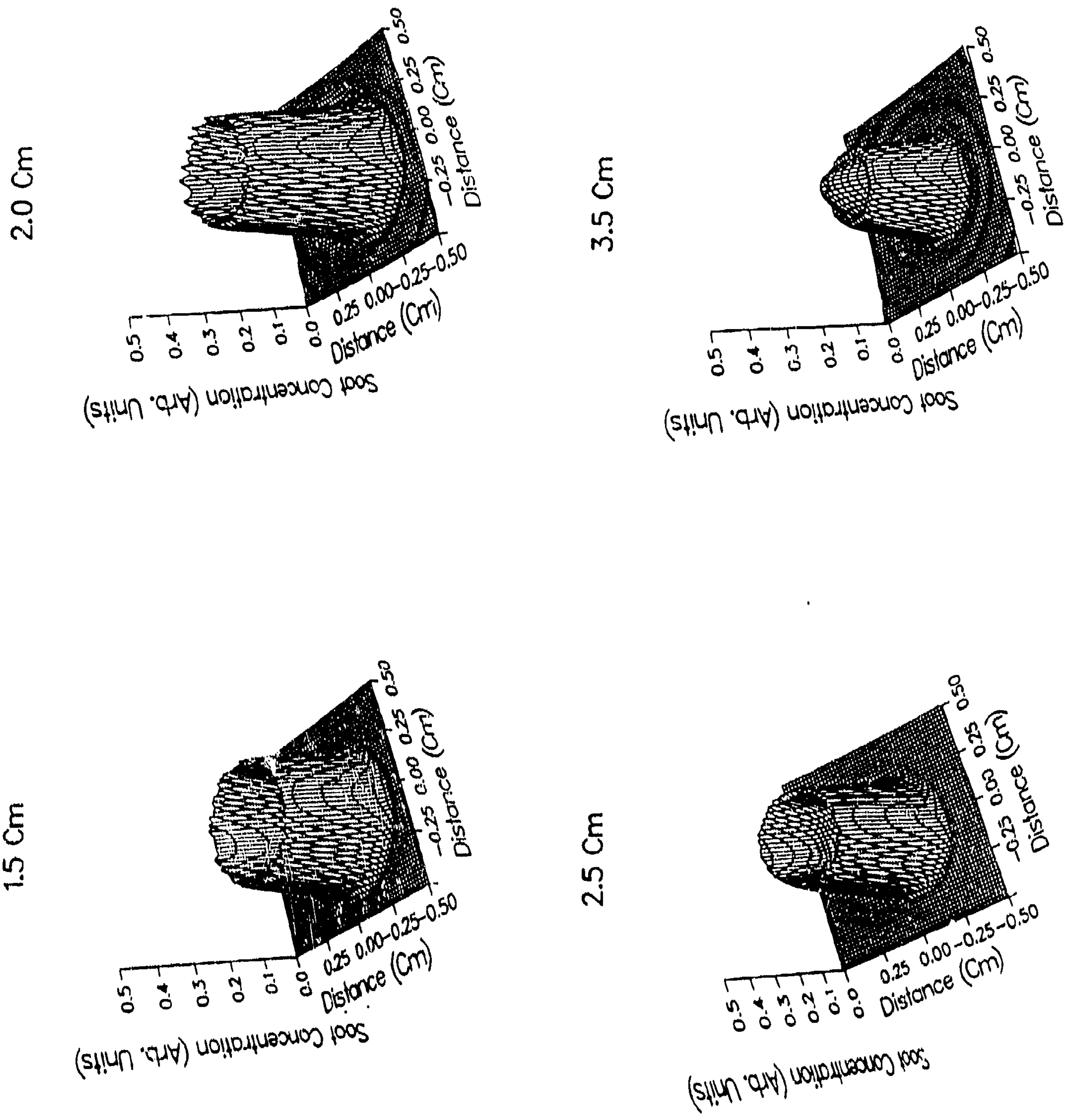

2.0 Cm

1.5 Cm

3.5 Cm

2.5 Cm

Figure 10

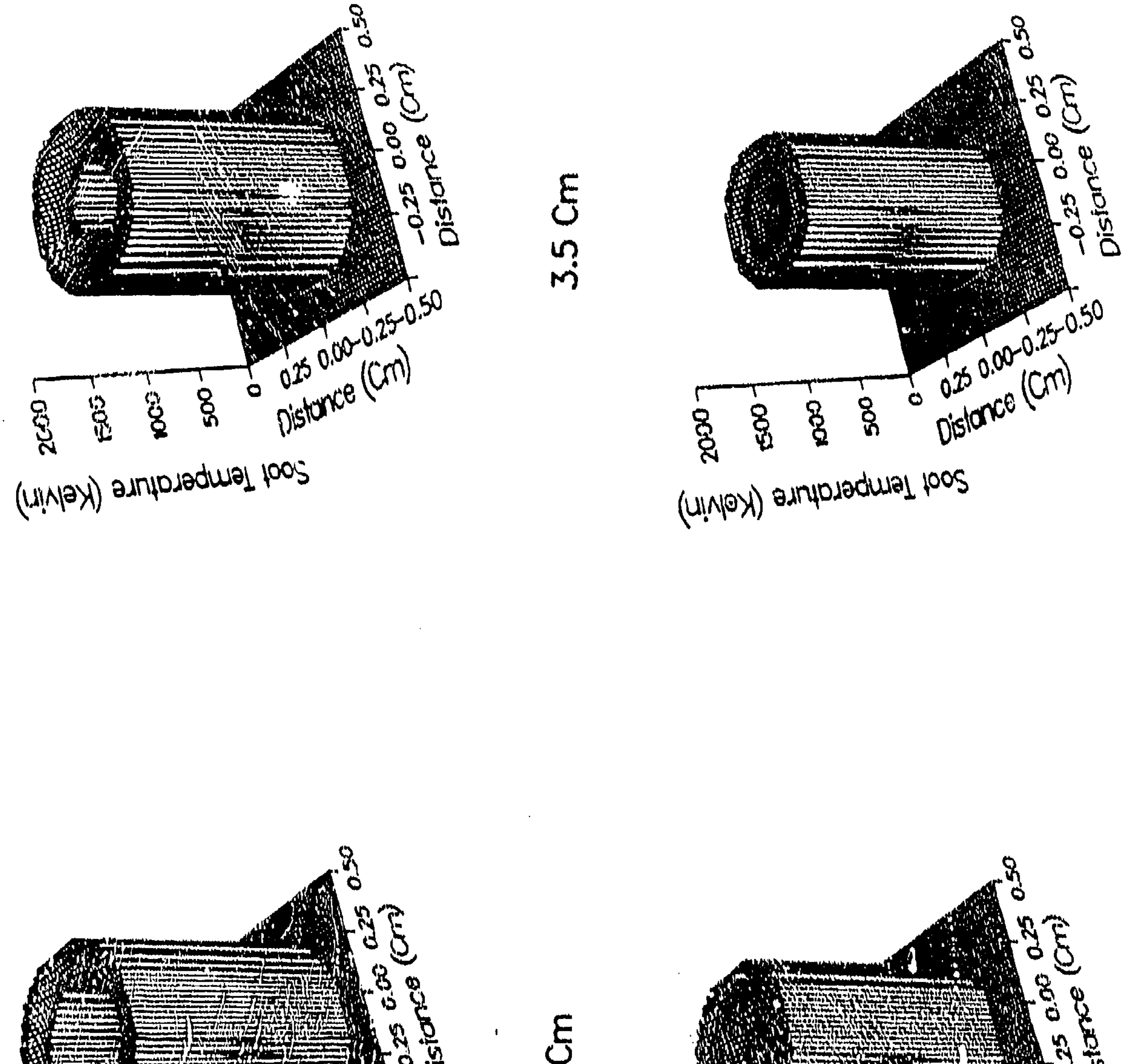
1.5 Cm
2.0 Cm
2.5 Cm
3.5 Cm
Soot Temperature (Kelvin)
2000
1500
1000
500
0
Distance (Cm)
0.25 0.00 -0.25 -0.50
-0.25 0.00 0.25 0.50

APPENDIX II

Presentations/Publications Under
AFOSR Contract F49620-86-C-0054

Presentations

1. *Fuel Additive Effects in Sooting Flames* was presented by P. A. Bonczyk at the 1988 AFOSR/ONR Contractor's Meeting on Combustion, Rocket Propulsion, and Diagnostics of Reacting Flow, Monrovia, Calif., June 13-17, 1988.

Publications

1. Hall, R. J., and P. A. Bonczyk: *Sooting Flame Thermometry Using Emission/Absorption Tomography* (submitted for publication in Applied Optics).

2. Bonczyk, P. A.: *Suppression of Soot by Ferrocene in a Prevaporized Iso-Octane/Air Diffusion Flame* (in preparation).

3. Bonczyk, P. A.: *Suppression of Soot by Alkali Metals in a Premixed $C_2H_4/O_2/N_2$ Flame* (in preparation).